Investigation of Conditional Source-term Estimation Approach to Modelling MILD Combustion

by

Jeffrey Labahn

A thesis
presented to the University of Waterloo
in fulfillment of the
thesis requirement for the degree of
Doctor of Philosophy
in
Mechanical Engineering

Waterloo, Ontario, Canada, 2016

I hereby declare that I am the sole author of this thesis. This is a true copy of the thesis, including any required final revisions, as accepted by my examiners.

I understand that my thesis may be made electronically available to the public.

Abstract

Conditional Source-term Estimation (CSE) is a turbulent combustion model which uses conditional averages to provide closure for the mean chemical source term and is based on the same ideas as the Conditional Moment Closure (CMC) approach. CSE applies first order closure for the conditional averages which are obtained by inverting an integral equation and has been used to simulate a range of premixed, non-premixed and partially premixed flames. In the present study, CSE is applied to investigate a high efficient, low emission combustion process called Moderate and Intense Low Oxygen Dilution (MILD) combustion. This work represents the first application of CSE for MILD combustion, the first application of a multi-stream CSE formulation and the first doubly-conditioned CSE formulation applied in the Large Eddy Simulation (LES) framework.

The objectives of the present study are to (i) investigate the CSE combustion model for turbulent non-premixed combustion, (ii) develop a CSE formulation for MILD combustion problems, (iii) implement CSE for MILD combustion problems in Reynolds-Averaged Navier-Stokes (RANS) and LES and (iv) compare the CSE predictions to experimental and previous numerical results for well documented MILD combustion flames.

Numerical simulations of a confined non-premixed methane flame are completed using the CSE non-premixed approach. This study investigates the sensitivity to various CSE model parameters and shows CSE is able to accurately predict non-premixed methane combustion. A detailed study of the inversion problem encountered in CSE is also investigated using the Bayesian framework. The origin of the perturbation seen in the unconditional mass fraction in CSE and the impact of a smoothing prior on the recovered solution and credible intervals are discussed. Different regularization methods are studied and it is shown that both zeroth and first order Tikhonov are promising regularization methods for CSE.

In the present work, the non-premixed CSE formulation is extended to include the impact of radiation of the conditional reaction rates and is applied to a semi-industrial furnace. This study demonstrates that a RANS-CSE simulation is able to accurately predict the temperature and species concentration, including NOx, for large scale realistic furnace configurations.

Finally, a multi-stream CSE formulation is developed and applied to the DJHC burners in the RANS and LES framework. This new CSE formulation is able to predict the temperature and velocity profiles in very good agreement with the experimental data. Further, the LES multi-stream CSE formulation is able to predict the time-dependent nature of the DHJC burners.

Acknowledgements

Over the past four years there have been a number of people who have made my accomplishments possible. I would like to take this opportunity to thank them for their support and help.

First, I would like to thank my supervisor, Professor Cecile Devaud who made this work possible. She introduced me to the challenges of turbulent combustion and has provided support, advice and encouragement throughout my PhD studies. Without her I would not have been able to complete this work or develop into the researcher I am today.

I would also like to thank Professor Clinton Groth, Professor Kyle Daun, Professor Francis Poulin, and Professor Fue-Sang Lien for consenting to be members of the thesis committee, and for reading and commenting on this thesis.

I would like to thank the Natural Sciences and Engineering Research Council of Canada (NSERC) and the Ontario government for their financial support. I would also like to acknowledge Compute Canada and SHARCNET, who provided the use of their supercomputers for the computations performed in this work.

I would like to thank all my colleagues and friends at the Energy Research Centre (ERC) for their support: Daniele Dovizio, Tim Sipkens, Dominic Ma, Kevin Lee, Duy Le, Mohammad Mortada, Amir Ashrafizadeh, Andrew Buckrell, Amine Debbagh, Guillaume Mancini and my other friends at the University of Waterloo for the great memories.

Finally, I would like to thank my family, my mother Laura for the countless hours she spent proofreading my papers and thesis, my father George, for providing motivation and advice, and my sister Claudia, and brother Phillip, for always being there and lending their support. This work would not have been possible without you.

Table of Contents

List of Tables **x**

List of Figures **xi**

Nomenclature **xvii**

1 Introduction **1**

1.1 Overview 1

1.2 Objectives 3

1.3 Overview of the study 4

1.4 Author's current contributions 5

2 Background **8**

2.1 Governing equations 8

2.2 Turbulent modelling approaches 10

2.2.1 Reynolds Averaged Navier-Stokes (RANS) 10

2.2.2 Large Eddy Simulation (LES) 14

2.2.3 Direct Numerical Simulation (DNS) 16

2.3 Non-premixed turbulent combustion models 17

2.3.1 Mixture fraction 17

2.3.2 Infinitely fast chemistry 19

2.3.3 Laminar Flamelet model 19
2.3.4 Conditional Moment Closure (CMC) 20
2.3.5 PDF methods 21
2.3.6 Conditional Source-term Estimation 21
2.4 Moderate and Intense Low Oxygen Dilution (MILD) combustion 22
2.5 Previous simulations of MILD combustion 23
2.6 Summary 24

3 CSE for turbulent non-premixed combustion 26
3.1 CSE 27
3.1.1 Model formulation 27
3.1.2 Inversion method 28
3.1.3 Chemistry tabulation 31
3.2 Computational details 33
3.2.1 Experimental conditions 33
3.2.2 CFD calculations 33
3.2.3 Turbulence models 36
3.2.4 CSE initialization 36
3.3 Results 37
3.3.1 Sensitivity to CSE ensemble number 37
3.3.2 Sensitivity to the mean mixture fraction range 41
3.3.3 Turbulent mixing field 44
3.3.4 Conditional averages 46
3.3.5 Temperature field 47
3.4 Summary 50

4 Inverse analysis and regularization in CSE **52**

4.1 Combustion problem 53

4.2 Computational details for the inverse problem 55

4.2.1 TSVD 59

4.2.2 Origin of perturbations 61

4.3 Bayesian analysis 63

4.3.1 Principle 63

4.3.2 Prior models 65

4.3.3 Bayesian credible intervals 66

4.3.4 Estimation of Γ_{noise} 67

4.3.5 Impact of prior on recovered solution 69

4.3.6 Impact of priors on credible intervals 72

4.3.7 Temporal smoothing vs spatial smoothing 74

4.4 Summary 79

5 CSE simulations of a semi-industrial furnace **81**

5.1 CSE formulation with radiation 81

5.1.1 Ensemble selection 82

5.1.2 Chemistry tabulation 82

5.2 Experimental conditions 83

5.3 Computational details 83

5.4 Results 85

5.4.1 Velocity 85

5.4.2 Temperature 86

5.4.3 Species concentration 88

5.4.4 Sensitivity to CSE ensemble selection 92

5.5 Summary 93

6 Two mixture fraction CSE for MILD combustion **94**
6.1 Mulitstream CSE formulation 94
6.1.1 Theory 94
6.1.2 Inversion method 96
6.1.3 Chemistry tabulation 96
6.1.4 Experimental conditions 97
6.2 Computational details 98
6.3 Results 101
6.3.1 Velocity and turbulent kinetic energy 101
6.3.2 Temperature 105
6.3.3 Lift-off height 109
6.3.4 Conditional mass fractions 109
6.3.5 Sensitivity to CSE ensemble selection 110
6.4 Summary 112

7 LES-CSE applied to MILD combustion **113**
7.1 LES formulation for mulitstream CSE 113
7.2 Computational details 115
7.3 Results 123
7.3.1 Turbulent flow field statistics 123
7.3.2 Temperature predictions 133
7.3.3 Lift-off height predictions 138
7.3.4 Flame characteristics 141
7.3.5 Conditional mass fractions 144
7.4 Summary 146

8 Conclusions and future work **147**
8.1 Summary of main findings 147
8.2 Summary of accomplishments 149
8.3 Future work 150

References **151**

List of Tables

4.1 Regularization parameters 75

5.1 Maximum absolute difference between the CSE predictions for 26 and 52 ensembles at three axial locations. Species concentration, X_{CH_4}, X_{CO_2}, X_{O_2}, X_{CO} and X_{H_2} are (%, dry). 15, 73 and 205 cm are axial locations 92

6.1 Experimental conditions selected for the present simulations (Re_d is the jet Reynolds number, T^c_{CO-max} the maximum coflow temperature and $Y^c_{O_2}$ the calculated mass flux weighted mean mass fraction in the coflow) 98

7.1 Numerical and experimental lift-off heights using P_{b1} and P_{b2} for the two DHJC flames under consideration. Lift-off heights are given in mm. DNG is Dutch natural gas. 140

List of Figures

2.1 Inlet temperature (Tin)-maximum temperature increase (ΔT) locus of different combustion modes for a methane/oxygen/nitrogen, well stirred reactor (WSR) mixture reproduced from [6]. T_{Si} is the self-ignition temperature . . . 23

3.1 Mixture fraction sampling locations . . . 31

3.2 TGLDM with Delaunay triangulation for $\eta_{st} = 0.055$ . . . 32

3.3 Computational grid (not to scale) . . . 34

3.4 CSE code structure. . . . 35

3.5 Centreline temperature profiles for different numbers of CSE ensembles . . 38

3.6 Radial temperature profiles for different numbers of CSE ensembles at different axial positions, same symbols as in Fig. 3.5 . . . 39

3.7 Conditional CO_2 mass fraction profiles for different numbers of CSE ensembles 40

3.8 Centreline temperature profiles for different CSE inversion ranges compared with experimental data [69] . . . 42

3.9 Radial temperature profiles at different axial positions for different CSE inversion ranges compared with experimental data [69], same symbols as in Fig. 3.8 . . . 43

3.10 Centreline mixture fraction profiles for different turbulence models compared with experimental data [69] . . . 44

3.11 Radial mixture fraction profiles at different axial positions for different turbulence models compared with experimental data [69], same symbols as in Fig. 3.10 . . . 45

3.12 Conditional CO_2 mass fraction profiles at different axial positions 47
3.13 Centreline temperature profiles for CSE, CMC [16] and flamelet [17] compared with experimental data [69] 48
3.14 Radial temperature profiles at different axial positions for CSE, CMC [16, 35] and flamelet [17] compared with experimental data [69], same symbols as in Fig. 3.13 49

4.1 Mean mixture fraction contours and location of CSE ensemble (shaded area) 54
4.2 Singular values for A matrix for 200 mixture fraction points 56
4.3 SVD solution to Eq. 4.3, with N=200 57
4.4 Perturbation analysis of Fourier coefficients, error term and singular values (same notation as in Eq. 4.8) 58
4.5 TSVD solution and error for perturbed $\vec{b}$ with 184 singular values truncated compared to exact solution (dashed line) 60
4.6 Perturbations in $\vec{b}_{exact}$ from the CSE simulations 61
4.7 Range of A_{jm} for CSE domain cells 63
4.8 Demonstration of 95% credible interval (shaded area) 67
4.9 Standard deviation of the unconditional mean mass fraction of CO_2 as a function of mean mixture fraction, unsmoothed (thin) and smoothed (bold) 68
4.10 MAP estimate with no smoothing prior (solid line) compared to exact solution (dashed line) 69
4.11 The effect of the smoothing prior on the maximum a posteriori estimate profile for two values of η, without a prior, $\alpha_2 = 0$ (dashed line) and with a prior, $\alpha_2 = 4000$ (solid line) 70
4.12 The effect of the smoothing prior on the MAP estimate, compared to exact solution (dashed line) 71
4.13 95% credible intervals (shaded area) with no smoothing prior compared to the exact solution (dashed line) 72
4.14 95% credible intervals (shaded area) for $\eta \leq 0.15$ with and without smoothing prior compared to the exact solution (dashed line). No smoothing prior corresponds to the non-negativity prior only, Eq. 4.14 and smoothing prior is spatial smoothing defined by Eq. 4.18 with $\alpha_2 = 4000$ 74

4.15 95% credible intervals (shaded area) for zeroth order temporal Tikhonov with different specified x_t profiles, the exact solution (left) and the least squares solution using a perturbed $\tilde{b}$ (right) compared to the exact solution (dashed line) 76

4.16 95% credible intervals shaded area) for first order Tikhonov compared to the exact solution (dashed line) with $\alpha_2 = \lambda^2/(2\sigma^2)$, as shown in Table 4.1 77

4.17 95% credible intervals (shaded area) for temporal and spatial smoothing for $\eta \geq 0.2$, compared to the exact solution (dashed line) 78

5.1 RANS computational domain showing one CSE ensemble and boundary conditions (not to scale) 84

5.2 CSE mean velocity profiles (solid lines) compared to the experimental data [57] (symbols) at various axial locations 86

5.3 CSE radial temperature profiles (solid lines) compared to the experimental data [57] (symbols) at various axial locations 87

5.4 CSE radial CO_2 and CO concentration (volume, dry) profiles (solid lines) compared to the experimental data [57] (symbols) at three axial locations . 89

5.5 CSE radial CH_4 and O_2 concentration (volume, dry) profiles (solid lines) compared to the experimental data [57] (symbols) at three axial locations . 90

5.6 CSE radial H_2 and NOx concentration (volume, dry) profiles (solid lines) compared to the experimental data [57] (symbols) at three axial locations . 91

6.1 Schematic of the computational domain 99

6.2 CSE mean axial velocity profiles in the radial direction (solid lines) compared to experimental data [54, 55] (symbols) at various axial locations for the DJHC-I 4100 flame 102

6.3 CSE mean axial velocity profiles in the radial direction (solid lines) compared to experimental data [54, 55] (symbols) at various axial locations for the DJHC-I 8800 flame 103

6.4 CSE mean turbulent kinetic profiles in the radial direction (solid lines) compared to experimental data [54, 55] (symbols) at various axial locations for the DJHC-I 4100 flame 104

6.5 CSE mean turbulent kinetic profiles in the radial direction (solid lines) compared to experimental data [54, 55] (symbols) at various axial locations for the DJHC-I 8800 flame 105

6.6 CSE radial temperature profiles (solid lines) compared to previous numerical results, standard EDC [29] (dot dashed line) and stochastic fields combustion model [9] (dashed line), and experimental data [54, 55] (symbols) at various axial locations for the DJHC-I 4100 flame 107

6.7 CSE radial temperature profiles (solid lines) compared to previous numerical results, stochastic fields combustion model [9] (dashed line), and experimental data [54, 55] (symbols) at various axial locations for the DJHC-I 8800 flame 108

6.8 Conditional mass fraction of CO_2 at two axial positions, 90 mm and 225 mm 110

6.9 Sensitivity to CSE ensemble selection: CSE predicted $\widetilde{Y}_{OH}$ profiles as a function of axial height using 8 (dashed line) and 12 (solid line) CSE ensembles for the DJHC-I 4100 flame 111

7.1 LES computational domain showing one CSE ensemble and boundary conditions 116

7.2 Resolution of the turbulent kinetic energy on the centreplane using Eq. 7.17 for the two flames under consideration. The isoline corresponding to R = 0.8 is also shown to distinguish between the well-resolved and under-resolved regions 122

7.3 LES-CSE time-averaged resolved axial velocity profiles in the radial direction (solid line) compared to RANS-CSE numerical predictions (blue line) and compared to experimental data [54, 55] (symbols) at various axial locations for the DJHC-I 4100 flame 123

7.4 LES-CSE time-averaged resolved axial velocity profiles in the radial direction (solid line) compared to RANS-CSE numerical predictions (blue line) and compared to experimental data [54, 55] (symbols) at various axial locations for the DJHC-I 8800 flame 124

7.5 LES-CSE time-averaged resolved radial velocity profiles in the radial direction (solid line) compared to RANS-CSE numerical predictions (blue line) and compared to experimental data [54, 55] (symbols) at various axial locations for the DJHC-I 4100 flame 126

7.6 LES-CSE time-averaged resolved radial velocity profiles in the radial direction (solid line) compared to RANS-CSE numerical predictions (blue line) and compared to experimental data [54, 55] (symbols) at various axial locations for the DJHC-I 8800 flame 127

7.7 LES-CSE time-averaged resolved axial velocity fluctuation profiles in the radial direction (solid line) compared to experimental data [54, 55] (symbols) at various axial locations for the DJHC-I 4100 flame 128

7.8 LES-CSE time-averaged resolved axial velocity fluctuation profiles in the radial direction (solid line) compared to experimental data [54, 55] (symbols) at various axial locations for the DJHC-I 8800 flame 129

7.9 LES-CSE time-averaged resolved $u'v'$ profiles in the radial direction (solid line) compared to experimental data [54, 55] (symbols) at various axial locations for the DJHC-I 4100 flame 130

7.10 LES-CSE time-averaged resolved $u'v'$ profiles in the radial direction (solid line) compared to experimental data [54, 55] (symbols) at various axial locations for the DJHC-I 8800 flame 131

7.11 LES-CSE time-averaged resolved turbulent kinetic energy profiles in the radial direction (solid line) compared to RANS-CSE numerical predictions (blue line) and compared to experimental data [54, 55] (symbols) at various axial locations for the DJHC-I 4100 flame (left) and DJHC-I 8800 flame (right) 132

7.12 LES-CSE time-averaged resolved temperature profiles in the radial direction (solid line) compared to RANS-CSE numerical predictions (blue line) and experimental data [54, 55] (symbols) at different axial locations for the DJHC-I 4100 flame 134

7.13 LES-CSE time-averaged resolved temperature profiles in the radial direction (solid line) compared to RANS-CSE numerical predictions (blue line) and experimental data [54, 55] (symbols) at various axial locations for the DJHC-I 8800 flame 135

7.14 LES-CSE temperature rms profiles in the radial direction (solid line) compared to experimental data [54, 55] (symbols) at various axial locations for the DJHC-I 4100 flame 136

7.15 LES-CSE temperature rms profiles in the radial direction (solid line) compared to experimental data [54, 55] (symbols) at various axial locations for the DJHC-I 8800 flame 137

7.16 CSE predicted P_{B1} and P_{B2} cumulative density functions for the DJHC-I 4100 (solid line) and DJHC-I 8800 (dashed line) flames 139

7.17 Flame front, defined as $\widetilde{Y}_{OH} \geq 10^{-3}$, and velocity vectors at six instantaneous time steps for the DJHC-I 8800 flame 142

7.18 Instantaneous methane reaction rate and temperature for the DJHC-I 8800 flame on the centreplane. The black lines at 90 mm and 225 mm correspond to the locations where the conditional averages are shown in Fig. 7.19 . . . 143

7.19 Instantaneous $\langle Y_{CO_2}|\eta, \upsilon\rangle$ profiles at various axial heights for each side of the CFD domain 145

Nomenclature

$Y_O^{O(0)}$	The minimum elemental oxygen (O) mass fraction in the coflow
$Y_O^{O(1)}$	The elemental oxygen mass fraction of the air stream
α	Molecular thermal diffusivity
α_t	Turbulent thermal diffusivity
χ_W	Scalar dissipation of oxidizer split
χ_Z	Scalar dissipation of mixture fraction
$\Delta h^0_{f,k}$	Enthalpy of formation of species k at the reference temperature
Δ	Filter size
δ	Delta function
$\delta_i j$	Kronecker symbol
$\dot{\omega}_k$	Species chemical reaction rate [kg/(m^{3}s)]
$\dot{Q}_r$	Radiation source term
η	Mixture fraction sample space variable
$\frac{D\overline{p}}{Dt}$	Total derivative of the filtered pressure
λ	Regularization parameter of Tikhonov regularization approach
λ	Thermal conductivity [W/(mK)]
$\langle u_i' u_i' \rangle$	Resolved time-averaged fluctuating quantities

μ	Molecular viscosity [Pas]
μ_t	Turbulent viscosity [Pas]
ν	Kinematic viscosity [m^2/s]
$\overline{f}$	Time average or filtered value of the quantity f
ρ	Density [kg/m^3]
τ_{ij}	Viscous stress tensor [Pa]
υ	Oxidizer split sample space variable
ε	Dissipation rate of the turbulent kinetic energy [m^2/s^3]
$\vec{\alpha}$	Solution of the Fredholm integral equation
$\vec{\alpha}_0$	*a priori* knowledge of the solution of the Fredholm integral equation
$\vec{b}$	Source vector representing the unconditional mass fraction in the CSE inversion problem
$\vec{x}_m$	Spatial coordinate of the m-th point in the ensemble J [m]
$\widetilde{f}$	Favre average or Favre-filtered value of the quantity f
A	Kernel of the Fredholm integral equation
$c_\chi, C_{\chi z}, C_{\chi w}$	Constant for the scalar dissipation rate estimation
$C_\mu, \sigma_k, \sigma_\varepsilon, C_{\varepsilon 1}, C_{\varepsilon 2}$	Standard $k-\varepsilon$ model constants
c_{pk}	Specific heat capacity of species k at constant pressure
D	Molecular diffusivity
D_t	Turbulent diffusivity
Da	Damköhler number
f''	Fluctuation of the quantity f
FDF	Filtered Density Function

h_t	Total specific enthalpy [kgm^2/s^2]
k	Turbulent kinetic energy [m^2/s^2]
Ka	Karlovitz number
L	Integral length scale [m]
Le	Lewis number
p	Pressure [Pa]
P_k	Production of turbulent kinetic energy [kg/(ms^2)]
PDF	Probability Density Function
q_i	The energy flux
Re_t	Turbulent Reynolds number
S	Strain rate [1/s]
Sc_{kt}	Turbulent Schmidt number for species k
T	Temperature [K]
T_0	Reference temperature
t_η	Kolmogorov time scale [s]
t_L	Integral time scale [s]
t_{chem}	Chemical time scale [s]
u'	Velocity root mean square [m/s]
u_i	i-th component of velocity [m/s]
W	Oxidizer split
x_i	i-th spatial coordinate [m]
Y_k	Mass fraction of the species k
$Y_{i,F}$	Mass fractions of element i in the fuel stream

$Y_{i,O}$	Mass fractions of element i in the oxidizer stream
Z	Mixture fraction
J	Ensemble of points used in CSE

Chapter 1

Introduction

1.1 Overview

Increased industrialization across the world has led to an increasing demand for energy. This energy is required for transportation, heating, electrical generation and industrial processes. Currently, turbulent combustion is primarily used to convert chemically bound energy into a usuable form. Indeed, turbulent combustion is the most common process in all practical systems as it allows enhanced mixing and heat release. The high energy density found in fossil fuels makes combustion attractive for transportation and propulsion processes and will likely remain the main method of power for these processes for the foreseeable future. Additionally, a significant portion of electric power generation is obtained from the turbulent combustion of fossil fuels. This burning of fossil fuels has led to an exponential growth in greenhouse gas emissions, which are expected to exceed 40 gigatonnes per year by 2035 [1]. As governments realize the negative impact of greenhouse gasses on the planet, a drive to reduce our dependence on fossil fuels and switch to renewable clean energy sources has begun. However, while reducing our dependence on fossil fuel is required, this cannot be accomplished instantaneously without a significant negative impact on the world economy. Furthermore, it will take time to scale up renewable clean energy sources to a level that can replace our dependency on fossil fuels. The United States Energy Information Administration (EIA) predicts that electrical energy obtained from renewable clean energy will increase from approximately 13% in 2013 to 22% in 2040 [2]. In comparison, the EIA predicts that coal could account for 34% of energy generation, with natural gas accounting a further 31% [2]. Thus, if we have any hope to reduce the amount of greenhouse gasses in the near future, then more efficient

combustion processes are required to reduce both greenhouse gas emissions and pollutants such as nitrogen oxides (NOx). In conjunction with experimental investigations, numerical simulations of turbulent combustion are required to further understand the physical phenomena involved and produce processes which are both cleaner and more efficient. The development of new combustion technologies is now being promoted to meet increasingly stringent atmospheric emission regulations with the goal of developing highly efficient and low pollutant combustion processes.

The requirement of highly efficient and low pollutant combustion is not limited to industrial electric generation, but is also required for the aerospace and transportation sectors. In 2014, 124.5 million people enplaned and deplaned at Canadian airports. This represents a growth of 45% since 2004 [3]. In addition, 1.1 million tonnes of freight worth $116.5 billion dollars was loaded or unloaded at Canadian airports. In 2012, the Canadian domestic aviation sector emitted 6.1 megatonnes of CO2 equivalent and accounted for 3.7 % of all transport greenhouse gas emissions. However, from 2000-2012 domestic aviation emissions decreased 20.7% despite increased traffic [3]. This decrease can be attributed to improved aircraft designs and aviation fuel efficiency, something significantly impacted by computer simulations of turbulent combustion processes. As a result, designing more efficient combustion processes has had a dramatic impact on emissions for the aerospace industry. The reductions are crucial when considering the size of the global aerospace industry. In 2014, 650 million people flew domestically in the USA [4], while approximately 3.3 billion flew worldwide according to the International Air Transport Association [5].

In the near term, renewable clean energy sources such as wind or solar do not appear to be feasible options for replacing turbulent combustion as the main source of energy. The implementation of renewable energy strategies requires overcoming technological issues including improving energy densities, increasing supply, storage capacities and large-scale market implementation, which limits its application in the foreseeable future. In order to further reduce the greenhouse gas footprint more efficient combustion processes are required. These new processes and designs can be optimized using computer simulations with detailed combustion models.

There are many different approaches which have been developed to increase combustion efficiencies in a range of industrial applications. In the present research, we have been focusing on Moderate and Intense Low Oxygen Dilution (MILD) combustion as it increases efficiencies, while at the same time reduces emissions. MILD combustion has two main characteristics: the inlet temperature of the reactants is above the stoichiometric auto-ignition temperature of the mixture; and the temperature increase of the system is less than the auto-ignition temperature [6]. High inlet temperatures can be obtained using exhaust gas recirculation where hot burnt products are mixed with fresh air. This reduces the oxygen concentration in the oxidizer steam, resulting in low peak temperatures and a

substantial reduction in NOx, which is responsible for smog and is a potential greenhouse gas, by up to 50% [6, 7]. The high oxidizer temperature can also increase the thermal efficiency of the system by up to 30% [7].

In turbulent combustion modelling, the turbulent flow field is modelled using one of three approaches: Direct Numerical Simulation (DNS), Large Eddy Simulation (LES) and Reynolds Averaged Navier-Stokes equations (RANS). DNS solves the Navier Stokes equations without any modelling. This is accomplished by temporally and spatially resolving the smallest eddies in the flow which requires a very small grid spacing and timestep. As a result, DNS is limited to simplified flows and geometry due to large computational costs. Thus, the use of DNS for industrial applications is not practical and is likely to remain so for the foreseeable future. LES requires less computational resources and has been shown to accurately describe the turbulent mixing between fuel and oxidizer. This is possible because the large turbulent eddies are computed without any modelling assumptions, whereas the subgrid scale turbulence is modelled. RANS simulations require even less computational resources but also result in a simplified description of the turbulent flow. Unlike LES, the RANS method contains modelling at all length scales. Consequently, the large scale transient motion of the flow is lost. The benefit of RANS is that it is commonly used in industry and has well-documented deficiencies. Further, the lower computational resources required make RANS an attractive method for model development. Within the current research framework, RANS and LES method are considered.

In turbulent combustion, difficulties arise when determining the averaged reaction-rate terms as the chemical kinetic rates are non-linear and the chemical reactions are strongly coupled with the micro-scale mixing [8]. Further difficulties are seen in modelling MILD combustion processes due to the complex interactions between turbulent fluid motion, combustion, radiation and multiphase flow. As the recirculated hot products do not necessarily have uniform properties this type of combustion is difficult to accurately model with traditional non-premixed combustion models. Since MILD combustion is a promising method for improved efficiency and reduced emissions, the development of theoretical models to predict this type of combustion is required.

1.2 Objectives

A typical MILD combustion burner consists of two parts, a main fuel nozzle and a flow of recirculated hot products or secondary coflow. In MILD combustion, due to heat lost to the walls and nonuniform combustion, the temperature and species concentrations may vary in the secondary coflow and recirculated hot produces. As a result, in MILD combustion,

models may need to include the variation in the properties of the coflow or recirculated hot products. One common strategy for extending non-premixed models to this type of MILD combustion is by including a second conditioning variable that is used to model the variation in the coflow or by including the effect of temperature on the chemical reaction rates. Conditional Source-term Estimation (CSE) is a combustion model based on using conditional averages. In contrast to most commonly used approaches, CSE can model any turbulent flame regime in any configuration in a relatively simple mathematical form. Thus, CSE is a good candidate for MILD combustion problems. The present study represents the first time that MILD combustion has been investigated using the CSE approach.

The proposed research focuses on the development of a combustion model based on the principles of the CSE method that can accurately model MILD combustion problems. The objectives of the proposed research can be summarized as follows:

1. Investigation of the CSE combustion model for turbulent non-premixed combustion
2. Development of CSE for MILD combustion problems
3. Implementation of CSE for MILD combustion problems in RANS and LES
4. Comparison of CSE predictions to experimental and previous numerical results for well documented MILD combustion flames

The purpose of the proposed research is to obtain predictions for temperature, species concentrations, velocity and flame characteristics such as flame length and lift-off height. The results will be compared to previous numerical work and experimental results to ensure the predictions are accurate. Further, the benefits and limitations of using the CSE to model these types of combustions problems will be determined. The proposed research is expected to make a significant contribution to the turbulent combustion field as CSE has never been applied to MILD combustion. This developed model can then be used in the design of high efficiency low emission furnaces and Homogenous Charge Compression-Ignition (HCCI) engines [9].

1.3 Overview of the study

In Chapter 2, background on turbulent combustion modelling and MILD combustion is provided. The governing equations that describe fluid behavior are described and the

different approaches of simulating turbulence are presented. Next, an overview of the commonly used turbulent combustion models and a description of MILD combustion are given.

Chapter 3 outlines the derivation of CSE for non-premixed combustion and inversion process used in CSE. Numerical simulations of a confined non-premixed methane flame are investigated using the RANS approach for turbulence modelling and CSE is applied to provide closure for the chemical source term. The effects of different CSE parameters are investigated and the CSE predictions are compared with available experimental results.

In Chapter 4, the CSE integral inversion for the combustion problem outlined in Chapter 3 is investigated using a Bayesian framework. Different regularization methods, are compared and credible intervals are calculated to determine the uncertainty in the recovered solution. The origins of the perturbations in the data is investigated and their magnitude quantified.

Chapter 5 describes the CSE simulations of a semi-industrial MILD furnace using a non-premixed CSE formulation. This CSE formulation accounts for the large radiative heat loss experienced in this furnace by including the conditional enthalpy in the tabulated chemistry. The CSE predictions are compared to detailed experimental temperature and species profiles, including NOx concentrations.

In Chapter 6, a multi-stream CSE formulation is developed to model the three-stream MILD Delft Jet-in-Hot-Coflow (DJHC) flames. A detailed description of this new CSE formulation is given and numerical simulations are performed in the RANS framework. The ability of this CSE formulation to model the DJHC flames is investigated by comparing the numerical predictions to available experimental data for velocity, turbulent kinetic energy and temperature.

In Chapter 7, the multi-stream CSE formulation outlined in Chapter 6 is extended to the LES framework for the DJHC flames, representing the first time a doubly conditioned CSE approach has been extended to the LES framework. The time dependent nature of the DJHC flames lift-off height and the ignition kernel formation mechanism are predicted using CSE. These predictions along with velocity, temperature and turbulent fluctuations of velocity and temperature are compared to available experimental data.

1.4 Author's current contributions

It is acknowledged that parts of the content presented in Chapter 3-7 are published in the following articles:

- J.W. Labahn, and C.B. Devaud. Large Eddy Simulations (LES) including Condi-

tional Source-term Estimation (CSE) applied to two Delft-Jet-in-Hot-Coflow (DJHC) flames. *Combustion and Flame,* 164:68-84, 2016.

- D. Dovizio, J.W. Labahn, and C.B. Devaud. Doubly Conditional Source-term Estimation (DCSE) applied to a series of lifted turbulent jet flames in cold air. *Combustion and Flame*, 162(5):1976–1986, 2015.

- J.W. Labahn, D. Dovizio, and C.B. Devaud. Numerical simulation of the Delft-Jet-in-Hot-Coflow (DJHC) flame using Conditional Source-term Estimation. *Proceedings of the Combustion Institute*, 35(3):3547–3555, 2015.

- J.W. Labahn, T.A. Sipkens, K.J. Daun and C.B. Devaud. Inverse Analysis and Regularization in Conditional Source-term Estimation Modelling. *Combustion Theory and Modelling,* 18(3): 474-499, 2014.

- J.W. Labahn, and C.B. Devaud. The application of the Conditional Source-term Estimation approach to modelling MILD combustion. *COMBURA,* 2014.

- J.W. Labahn, D. Dovizio, and C.B. Devaud. Simulation of MILD combustion using the CSE Approach. *Proceedings of the Combustion Institute/Canadian Section Spring Technical Meeting,* University of Windsor, May 12-15, 2014.

- D. Dovizio, J.W. Labahn, and C.B. Devaud. Doubly Conditional Source-term Estimation model for the simulation of turbulent lifted jet flames. *Proceedings of the Combustion Institute/Canadian Section Spring Technical Meeting,* University of Windsor, May 12-15, 2014.

- J.W. Labahn, and C.B. Devaud. Investigation of Conditional Source-term Estimation applied to a non-premixed turbulent flame. *Combustion Theory and Modelling,*17(5): 960-982, 2013.

- D. Dovizio, J.W. Labahn, and C.B. Devaud. Doubly Conditional Source-Term Estimation Applied to a Turbulent Lifted Jet Flame. *Eighth Mediterranean Combustion Symposium,* Çeşme, İzmir, Turkey, September 8-13, 2013.

- D. Dovizio, J.W. Labahn, and C.B. Devaud. RANS simulation of a turbulent lifted jet flame using Conditional Source Estimation. *Proceedings of the Combustion Institute/Canadian Section Spring Technical Meeting,* Université Laval, Québec, May 13-16, 2013.

- J.W. Labahn, and C.B. Devaud. RANS simulation of a confined turbulent non-premixed methane flame using CSE. *Proceedings of the Combustion Institute/Canadian Section Spring Technical Meeting,* Université Laval, Québec, May 13-16, 2013.

Chapter 2

Background

This chapter provides a brief review of background information required for turbulent combustion modeling. This chapter begins with a review of the governing equations that are used to describe a fluid. An overview of the RANS approach and the details on two RANS turbulent models, the standard $k-\epsilon$ and Re-Normalization Group (RNG) k-ϵ turbulent models are then presented. This is followed by a review of the principles of the LES approach and details on the Smagorinsky model. A description of the Direct Numerical Simulation (DNS) is then provided. A review of common non-premixed turbulent combustion modelling methods are also presented. This chapter finishes with details on previous simulations of MILD combustion.

2.1 Governing equations

The first governing equation that describes any fluid flow is conservation of mass. Conservation of mass, also known as the continuity equation, states that mass cannot be created or destroyed and is written as

$$\frac{\partial \rho}{\partial t} + \frac{\partial}{\partial x_i}(\rho u_i) = 0. \tag{2.1}$$

In Eq. 2.1, ρ is the density, u the velocity and i the index representing the three spatial coordinates, $i = 1, 2, 3$. The second governing equation is the conservation of linear momentum given by

$$\frac{\partial(\rho u_j)}{\partial t} + \frac{\partial}{\partial x_i}(\rho u_i u_j) = -\frac{\partial p}{\partial x_j} + \frac{\partial \tau_{ij}}{\partial x_i} + B_j, \tag{2.2}$$

where p is the pressure, the second term on the Right Hand Side (RHS) the viscous stress tensor and the last term on the RHS represents any body forces acting on the fluid, such as gravity. For a multi-species fluid this term can be expanded as

$$B_j = \rho \sum_{k=1}^{N} Y_k f_{k,j}, \tag{2.3}$$

where $f_{k,j}$ is the body force acting on species k in the j-th direction, N is the number of different species in the fluid and Y_k the mass fraction of species k. For a Newtonian fluid the viscous stress tensor is defined as

$$\tau_{ij} = -\frac{2}{3}\mu \frac{\partial u_k}{\partial x_k}\delta_{ij} + \mu\left(\frac{\partial u_i}{\partial x_j} + \frac{\partial u_j}{\partial x_i}\right), \tag{2.4}$$

where μ is the dynamic viscosity and δ_{ij} is the Kronecker delta. For a multi-species fluid the conservation of species for species k is given by

$$\frac{\partial(\rho Y_k)}{\partial t} + \frac{\partial}{\partial x_i}(\rho u_i Y_k) = -\frac{\partial(j_{k,i})}{\partial x_i} + \dot{\omega}_k \quad \text{for} \quad k = 1, N. \tag{2.5}$$

In Eq. 2.5, $j_{k,i}$ is the diffusive flux of species k, and $\dot{\omega}_k$ the reaction rate of species k. To satisfy conservation of mass the sum of all species mass fractions must always equal one.

The third and final governing equation of a fluid is the energy equation. Many different formulations of the energy equations have been defined based on the total enthalpy, sensible enthalpy, temperature and internal energy. In combustion modelling, the energy equation based on the total enthalpy is often selected. The total enthalpy of species k is defined as the sum of the sensible enthalpy and the enthalpy of formation and calculated as

$$h_k = \int_{T_0}^{T} c_{pk} dT + \Delta h^0_{f,k}, \tag{2.6}$$

where the first term on the RHS represents the sensible enthalpy, c_{pk} the heat capacity of species k and $\Delta h^0_{f,k}$ the heat of formation of species k at reference temperature T_0. The total enthalpy of the mixture is then calculated as the mass-weighted sum of the total enthalpy for each species:

$$h = \sum_{k=1}^{N} h_k Y_k = \int_{T_0}^{T} c_{pk} Y_k dT + \sum_{k=1}^{N} \Delta h^0_{f,k} Y_k. \tag{2.7}$$

The heat capacity of the fluid is calculated using the same principle, such that

$$c_p = \sum_{k=1}^{N} c_{pk} Y_k. \tag{2.8}$$

The energy equation, based on the total enthalpy, can then be obtained by solving

$$\frac{\partial(\rho h)}{\partial t} + \frac{\partial}{\partial x_i}(\rho u_i h) = \frac{\partial p}{\partial t} + u_i \frac{\partial p}{\partial x_i} + \frac{\partial}{\partial x_i}(u_i \tau_{ij}) - \frac{\partial q_i}{\partial x_i} + \dot{Q}_r + u_i B_i, \tag{2.9}$$

where the second term on the RHS is the work due by pressure, the third term represents a source term due to friction and the final term is the work done by volume forces. The energy flux, q_i is calculated as

$$q_i = -\lambda \frac{\partial T}{\partial x_i} + \rho \sum_{k=1}^{N} h_k j_k, \tag{2.10}$$

λ being the thermal conductivity of the mixture and j_k the diffusive heat flux. The diffusive heat flux can be calculated using Fick's first law,

$$j_k = -\rho D_k \frac{\partial Y_k}{\partial x_i}. \tag{2.11}$$

where D_k is the diffusivity of species k.

2.2 Turbulent modelling approaches

2.2.1 Reynolds Averaged Navier-Stokes (RANS)

In RANS, the Navier-Stokes equations are averaged to obtain the mean values of the turbulent flow. The averaging process results in unclosed terms which require closure. Due to the large density variations encountered in combustion it is convenient to use density-weighted averages or Favre-averaged quantities. The Favre-averaged quantities are defined as

$$\widetilde{\phi} = \frac{\overline{\rho\phi}}{\bar{\rho}}, \tag{2.12}$$

where ϕ is any quantity of interest and fluctuations of the Favre-averaged quantity is defined as

$$\phi'' = \phi - \widetilde{\phi}. \tag{2.13}$$

It is also important to note that when using Favre-averaged quantities the following relationship holds

$$\overline{\rho\phi''} = 0, \tag{2.14}$$

but unlike Reynolds averaging

$$\overline{\phi''} \neq 0. \tag{2.15}$$

The governing transport equations, neglecting body forces, for RANS are
Conservation of Mass (Continuity)

$$\frac{\partial\overline{\rho}}{\partial t} + \frac{\partial}{\partial x_i}(\overline{\rho}\widetilde{u_i}) = 0, \tag{2.16}$$

Conservation of Momentum

$$\frac{\partial\overline{\rho}\widetilde{u_i}}{\partial t} + \frac{\partial}{\partial x_i}(\overline{\rho}\widetilde{u_i}\widetilde{u_i}) + \frac{\partial p}{\partial x_j} = \frac{\partial}{\partial x_i}\Big(\overline{\tau}_{ij} - \widetilde{\overline{\rho}u_i''u_j''}\Big), \tag{2.17}$$

Conservation of Species

$$\frac{\partial\overline{\rho}\widetilde{Y_k}}{\partial t} + \frac{\partial}{\partial x_i}(\overline{\rho}\widetilde{u_i}\widetilde{Y_k}) = \overline{\dot{\omega}_k} - \frac{\partial}{\partial x_i}\Big(\overline{\rho u_i''Y_k''}\Big) + \overline{\frac{\partial}{\partial x_i}\rho D_k\frac{\partial Y_k}{\partial x_i}}, \tag{2.18}$$

Conservation of Energy

$$\frac{\partial\overline{\rho}\widetilde{h_t}}{\partial t} + \frac{\partial}{\partial x_i}(\overline{\rho}\widetilde{u_i}\widetilde{h_t}) + \frac{\partial p}{\partial x_i} = \frac{\partial}{\partial x_i}\Big(\overline{\lambda\frac{\partial T}{\partial X_i}} - \widetilde{\overline{\rho}u_i''h_t''}\Big) + \overline{\tau_{ij}\frac{\partial u_i}{\partial x_j}} + \dot{Q}_r. \tag{2.19}$$

The unclosed terms in the governing transport equations are modelled using different methods. For the species and energy transport equation the unclosed terms, $\widetilde{\overline{\rho}u_i''Y_k''}$ and $\widetilde{\overline{\rho}u_i''h_t''}$, are often closed using a gradient assumption. Using the gradient assumption these terms are modelled as

$$\widetilde{\overline{\rho}u_i''Y_k''} = -\frac{\mu_t}{Sc_{kt}}\frac{\partial\widetilde{Y_k}}{\partial x_k} \quad \text{and} \quad \widetilde{\overline{\rho}u_i''h_t''} = -\frac{\mu_t}{Pr_{kt}}\frac{\partial\widetilde{h_t}}{\partial x_k}, \tag{2.20}$$

where μ_t is the turbulent viscosity calculated by the turbulence model, Pr_{kt} the turbulent Prandtl number and Sc_{kt} the turbulent Schmidt number for species k. For turbulent combustion the laminar diffusion flux, $\overline{\lambda \frac{\partial T}{\partial X_i}}$, and the final term in Equation 2.18 are often omitted using the assumption that at high Reynolds numbers these terms are negligible. The purpose of turbulent combustion models is to calculate the mean chemical source term, $\overline{\dot{\omega}_k}$, in Equation 2.18.

Various turbulence models have been developed to close the Reynolds stresses, $\widetilde{u_i'' u_j''}$, which can broadly be classified into four categories: one equation models, two equation models, algebraic models and Reynolds Stress models (RSM) [10, 11]. In RANS modelling the most common approach to close the Reynolds stresses are two equation models such as the k-ϵ [12] and Re-Normalization Group (RNG) k-ϵ [10]. These two equation models are based on the eddy viscosity concept and the Reynolds stresses are calculated as

$$\overline{\rho}\widetilde{u_i'' u_j''} = -\mu_t \left(\frac{\partial \widetilde{u}_i}{\partial x_j} + \frac{\partial \widetilde{u}_j}{\partial x_i} - \frac{2}{3}\delta_{ij} \frac{\partial \widetilde{u}_k}{\partial x_k} \right) + \frac{2}{3}\overline{\rho}\delta_{ij}\widetilde{k}, \tag{2.21}$$

where $\widetilde{k}$ is turbulent kinetic energy defined as

$$\widetilde{k} = \frac{1}{2}\sum_{k=1}^{3} \widetilde{u_k'' u_k''}. \tag{2.22}$$

Turbulence models in RANS

Various turbulence models have been developed to close the Reynolds stresses. For the current research only the k-ϵ [12] and Re-Normalization Group (RNG) k-ϵ [10] turbulence models are considered and are chosen as they are commonly used in turbulent combustion. A brief review of these two models is presented. The $k-\epsilon$ model [12] is one of the most commonly used turbulence model. The transport equations used for the $k-\epsilon$ model are given by

$$\bar{\rho}\frac{\partial \widetilde{k}}{\partial t} + \bar{\rho}\widetilde{u}_i \frac{\partial \widetilde{k}}{\partial x_i} = \frac{\partial}{\partial x_i}\Big[\Big(\mu + \frac{\mu_t}{\sigma_k}\Big)\frac{\partial \widetilde{k}}{\partial x_i}\Big] + \bar{\rho}P_k - \bar{\rho}\widetilde{\epsilon}, \tag{2.23}$$

and

$$\bar{\rho}\frac{\partial \widetilde{\epsilon}}{\partial t} + \bar{\rho}\widetilde{u}_i \frac{\partial \widetilde{\epsilon}}{\partial x_i} = \frac{\partial}{\partial x_i}\Big[\Big(\mu + \frac{\mu_t}{\sigma_\epsilon}\Big)\frac{\partial \widetilde{\epsilon}}{\partial x_i}\Big] + C_{\epsilon 1}\frac{\widetilde{\epsilon}}{\widetilde{k}}P_k - C_{\epsilon 2}\bar{\rho}\frac{\widetilde{\epsilon}^2}{\widetilde{k}}, \tag{2.24}$$

where

$$\mu_t = \bar{\rho} C_\mu \frac{\widetilde{k}^2}{\widetilde{\epsilon}}, \tag{2.25}$$

with $C_{\epsilon 1} = 1.44, C_{\epsilon 2} = 1.92, C_\mu = 0.09, \sigma_k = 1.0, \sigma_\epsilon = 1.3$ [12]. The source term P_k is calculated as

$$P_k = -\bar{\rho}\widetilde{u_i'' u_j''}\frac{\partial \widetilde{u}_i}{\partial x_j}. \tag{2.26}$$

One reason for the $k-\epsilon$ model's popularity is that its deficiencies are well known as are the modifications to the standard $k-\epsilon$ model to correct these deficiencies. For example, it is well-known that the standard $k-\epsilon$ model over predicts the spreading rate in round jets [13, 14]. There are various methods for correcting this behavior. One common method is to modify the value of $C_{\epsilon 1}$. Dally et al.[15] have shown that a $C_{\epsilon 1}$ value of 1.6 better predicts spreading rates in non-reacting jets. It has also been shown that this correction can be applied to non-premixed jet flow combustion [16, 17].

In the RNG $k-\epsilon$ turbulence model, a random forcing function is introduced to the Navier-Stokes equations to simulate the effects of small-scale turbulence. This is accomplished by removing the effects of the small scales of motion from the Navier-Stokes equations and expressing them in terms of large scaled motion and modified viscosity [10]. The transport equations used for the RNG $k-\epsilon$ model [18] are given by

$$\bar{\rho}\frac{\partial \widetilde{\epsilon}}{\partial t} + \bar{\rho}\widetilde{u}_i\frac{\partial \widetilde{\epsilon}}{\partial x_i} = \frac{\partial}{\partial x_i}\Big[\Big(\mu + \frac{\mu_t}{\sigma_\epsilon}\Big)\frac{\partial \widetilde{\epsilon}}{\partial x_i}\Big] + C^*_{\epsilon 1}\frac{\widetilde{\epsilon}}{\widetilde{k}}P_k - C_{\epsilon 2}\bar{\rho}\frac{\widetilde{\epsilon}^2}{\widetilde{k}}, \tag{2.27}$$

where

$$C^*_{\epsilon 1} \;=\; C_{\epsilon 1} - \frac{\eta\Big(1-\frac{\eta}{\eta_0}\Big)}{1+\beta\eta^3}, \quad \eta = \frac{S\widetilde{k}}{\widetilde{\epsilon}}, \quad S = (2S_{ij}S_{ij})^{\frac{1}{2}}, \tag{2.28}$$

with S_{ij} being the mean strain rate component and the transport equation for k and turbulent viscosity determined using the same method as in the standard $k-\epsilon$ model.

The constants in the RNG $k-\epsilon$ model [18] are given by:

$$C_\mu = 0.0845, \quad \sigma_k = 0.7194, \quad \sigma_\epsilon = 0.7194, \tag{2.29}$$

$$C_{\epsilon 1} = 1.42, \quad C_{\epsilon 2} = 1.68, \quad \eta_0 = 4.38 \tag{2.30}$$

with $\beta = 0.012$ derived from experimental results.

2.2.2 Large Eddy Simulation (LES)

Large Eddy Simulation is more computationally expensive than RANS, but has several advantages. In LES, the large scale motion of the fluid is directly computed, while the smaller scale motion is modelled. Thus, LES simulations are able to accurately simulate both the large scale motion and mixing field better than RANS simulations. In addition, the computational cost of LES is significantly lower than for DNS simulations [11]. This combination makes LES very attractive to industrial simulations. Unlike the RANS approach, which uses time averaging to obtain the governing transport equations, LES uses a spatial filtering operation to separate the larger and smaller eddies.

The first step in the LES approach is the selection of a filtering function and a cut-off width. The purpose of the cut-off width is to determine which length scales are modelled and which are solved directly. Next, the filtering operation is used to decompose the velocity,

$$U(x,t) = \overline{U}(x,t) + u^{'}(x,t), \tag{2.31}$$

where $\overline{U}(x,t)$ is the filtered velocity component, which represents the fluid motion of the large eddies, and $u^{'}(x,t)$ is the residual velocity component. The filtered velocity is obtained using [19],

$$\overline{U}(\vec{x},t) = \int_V U(\vec{x},t)G(\vec{x}-\vec{x'})\ d\vec{x'}. \tag{2.32}$$

In Eq. 2.32 $G(\vec{x})$ is a spatial low-pass filter function at location $\vec{x}$. Various filtering functions can be used, such as the top hat filter or Gaussian filter defined as:

Top hat filter

$$G(\vec{x}-\vec{x'}) = \begin{cases} \frac{1}{\Delta} & \text{if } |\vec{x}-\vec{x'}| \leq \Delta/2 \\ 0 & \text{otherwise} \end{cases} \tag{2.33}$$

Gaussian filter

$$G(\vec{x}-\vec{x'}) = \left(\frac{6}{\pi\Delta^2}\right)^{1/2} exp\left(-\frac{6(\vec{x}-\vec{x'})^2}{\Delta^2}\right) \tag{2.34}$$

where Δ is the filter size. Following the decomposition of the velocity, the filtered Navier Stokes equations are derived by substituting Eq. 2.31 into the Navier-Stokes equations,

resulting in the following filtered governing equations:
Conservation of Mass (Continuity)

$$\frac{\partial \overline{\rho}}{\partial t} + \frac{\partial}{\partial x_i}(\overline{\rho}\widetilde{u}_i) = 0 \tag{2.35}$$

Conservation of Linear Momentum

$$\frac{\partial \overline{\rho}\widetilde{u}_i}{\partial t} + \frac{\partial}{\partial x_i}(\overline{\rho}\widetilde{u}_i\widetilde{u}_j) + \frac{\partial \overline{p}}{\partial x_j} = \frac{\partial}{\partial x_i}\left[\overline{\tau}_{ij} - \overline{\rho}\left(\widetilde{u_i u_j} - \widetilde{u}_i\widetilde{u}_j\right)\right] \tag{2.36}$$

Conservation of Species

$$\frac{\partial \bar{\rho}\widetilde{Y}_k}{\partial t} + \frac{\partial(\bar{\rho}\widetilde{u}_i\widetilde{Y}_k)}{\partial x_i} = \frac{\partial}{\partial x_i}\Big((D + D_t)\frac{\partial \widetilde{Y}_k}{\partial x_i}\Big) + \bar{\dot{\omega}}_k \tag{2.37}$$

Conservation of Energy

$$\frac{\partial(\overline{\rho}\widetilde{h})}{\partial t} + \frac{\partial(\overline{\rho}\widetilde{u}_i\widetilde{h})}{\partial x_i} = \frac{\partial}{\partial x_i}\left(\bar{\rho}(\alpha + \alpha_t)\frac{\partial \widetilde{h}}{\partial x_i}\right) + \frac{D\overline{p}}{Dt} + \dot{Q}_r \tag{2.38}$$

where D_t is the turbulent molecular diffusivity, α and α_t are the molecular and turbulent thermal diffusivity and $\frac{D\overline{p}}{Dt}$ the total derivative of the filtered pressure.

In the conservation of linear momentum, $\overline{\tau}_{ij}$ is the viscous stress tensor given by

$$\overline{\tau}_{ij} = -\overline{\mu\rho}\widetilde{u_i'' u_j''} = -\mu_t\left(\frac{\partial \widetilde{u}_i}{\partial x_j} + \frac{\partial \widetilde{u}_j}{\partial x_i} - \frac{2}{3}\delta_{ij}\frac{\partial \widetilde{u}_k}{\partial x_k}\right). \tag{2.39}$$

Similar to the RANS approach, the resulting filtered Navier Stokes equations contain an unclosed term, called the residual-stress tensor (or subgrid-scale (SGS) stress tensor) which is defined as $\sigma_{ij} = \overline{\rho}\left(\widetilde{u_i u_j} - \widetilde{u}_i\widetilde{u}_j\right)$. Closure for the residual-stress tensor is given by

$$\sigma_{ij} - \frac{1}{3}\delta_{ij}\sigma_{kk} = -2\overline{\rho}\nu_{t_{SGS}}\left(\widetilde{S}_{ij} - \frac{1}{3}\delta_{ij}\widetilde{S}_{kk}\right). \tag{2.40}$$

In Eq. 2.40, $\nu_{t_{SGS}}$ is the turbulent SGS viscosity, σ_{kk} the isotropic contribution of the Reynolds stresses and $\widetilde{S}_{ij}$ the filtered rate-of-strain tensor defined as

$$\widetilde{S}_{ij} = \frac{1}{2}\left(\frac{\partial \widetilde{u}_i}{\partial x_j} + \frac{\partial \widetilde{u}_j}{\partial x_i}\right). \tag{2.41}$$

Various modelling techniques have been developed to provide closure for the turbulent SGS viscosity. The Smagorinksy SGS model is the simplest of these models and is based the eddy-viscosity model [10, 11]. In the Smagorinksy SGS model the turbulent SGS viscosity is calculated as

$$\nu_{t_{SGS}} = (C_S\Delta)^2\sqrt{(2\overline{S}_{ij}\overline{S}_{ij})}, \tag{2.42}$$

where C_s is the Smagorinksy coefficient. This constant is either set as a fixed value or calculated dynamically [20].

2.2.3 Direct Numerical Simulation (DNS)

In the Direct Numerical Simulation (DNS) approach the governing equations are solved without modelling. Thus, in DNS the grid spacing must be smaller than the smallest length scale of the smallest eddy. The main advantage of DNS is that no assumptions are made, thus eliminating modelling error. However, the computational requirements for a DNS simulation are often prohibitive. For homogeneous turbulence, using pseudo-spectral methods, the maximum grid spacing in DNS [11] can be calculated using

$$\Delta x = \frac{\pi}{1.5}\eta, \tag{2.43}$$

where η is the Kolmogorov length scale defined as

$$\eta \equiv (\nu^3/\varepsilon)^{1/4}. \tag{2.44}$$

In Eq. 2.44, ε is the dissipation rate of the turbulent kinetic energy and ν the kinematic viscosity and the minimal size of the computational domain can be calculated using

$$\kappa_0 L_{11} = \frac{\pi}{4}, \tag{2.45}$$

where κ_0 is the lowest wave number and L_{11} is the integral length scale. Using this information the number of computational cells required is proportional to $Re_\lambda^{\frac{9}{2}}$ [11] with Re_λ being the Taylor-scale Reynolds number based on the transverse Taylor length scale (λ_g). Re_λ is calculated using the turbulent velocity fluctuations (u') such that

$$Re_\lambda = \frac{u'\lambda_g}{\nu}. \tag{2.46}$$

For a typical simulation, a Courant number of approximately 0.05 is imposed and the simulation time is approximately four times the turbulence time scale, $\tau = \frac{k}{\epsilon}$. Thus, the

total number of time steps required is

$$M = \frac{120}{\pi}\frac{L}{\eta} \approx 9.2 Re_{\lambda}^{\frac{3}{2}}. \tag{2.47}$$

Further, the total number of floating-point operations can be calculated for a typical simulation and is found to be proportional to Re_{λ}^{6} [11]. If a detailed chemical mechanism is included for a combustion problem the number of scalars and reactions that need to be solved can be on the order of tens to hundreds. As a result, DNS for turbulent combustion is limited to simplified geometry with homogeneous isotropic turbulence or mixing layers [21, 22] and these results are used to develop other combustion models.

2.3 Non-premixed turbulent combustion models

In turbulent combustion modeling the mean or filtered chemical source term is unclosed as a result of the averaging or filtering used in RANS or LES turbulence modeing. The purpose of turbulent combustion modelling is to provide closure to the mean or filtered chemical source term. Well-known combustion models fall into several catagories: infinitely fast chemistry models; Laminar Flamelet models [23]; Conditional Moment Closure (CMC) [24]; or Probability Density Function (PDF) models. In non-premixed combustion the mixing of the fuel and oxidizer and combustion occur simultaneously. Thus, in non-premixed combustion with fast chemistry, mixing is the rate limiting step and it is convenient to define a conserved scalar, mixture fraction, which models the mixing between fuel and oxidizer. This section presents a brief review of the mixture fraction and well-known combustion models.

2.3.1 Mixture fraction

In non-premixed combustion, the combustion process is controlled by the mixing of the fuel and the oxidizer. As a result, it is convenient to create a scalar, called mixture fraction, Z, which is a representative of this mixing. The mixture fraction is defined to have a value of 1 in the pure fuel stream and 0 in the pure oxidizer stream. Between these two limits the mixture fraction is defined following Bilger [25] as

$$Z = \frac{Y_i - Y_{i,O}}{Y_{i,F} - Y_{i,O}}, \tag{2.48}$$

where Y_i is the mass fraction of element i in the local mixture, and $Y_{i,O}$ and $Y_{i,F}$ is the mass fraction of element i in the oxidizer and fuel streams, respectively. The mixture fraction is a conserved scalar meaning there is no source term in its governing transport equation.

If the fast chemistry assumption is applied, all scalar values in turbulent non-premixed combustion are functions of the mixture fraction only [26]. The resulting Favre-averaged transport equation for mixture fraction is given by

$$\frac{\partial(\overline{\rho}\widetilde{Z})}{\partial t} + \frac{\partial}{\partial x_i}(\overline{\rho}\widetilde{u_i}\widetilde{Z}) = \frac{\partial}{\partial x_i}\left(\overline{\rho D \frac{\partial Z}{\partial x_i}} - \overline{\rho}\widetilde{u_i'' Z''}\right). \tag{2.49}$$

Similarly, the Favre-averaged transport equations for mixture fraction variance is

$$\frac{\partial(\overline{\rho}\widetilde{Z''^2})}{\partial t} + \frac{\partial}{\partial x_i}(\overline{\rho}\widetilde{u_i}\widetilde{Z''^2}) = \underbrace{-\frac{\partial}{\partial x_i}\left(\overline{\rho u_i'' Z''^2}\right)}_{\text{turbulent transport}} + \underbrace{\frac{\partial}{\partial x_i}\left(\overline{\rho D \frac{\partial Z''^2}{\partial x_i}}\right)}_{\text{molecular diffusion}} \tag{2.50}$$

$$- \underbrace{2\overline{\rho}\widetilde{u_i'' Z''}}_{\textit{production}} - \underbrace{\overline{\rho}\widetilde{\chi}}_{\text{dissipation}}. \tag{2.51}$$

Closure for the turbulent flux, $\widetilde{u_i'' Z''}$ is provided using the gradient assumption,

$$\widetilde{u_i'' Z''} = -D_t \frac{\partial \widetilde{Z}}{\partial x_i}, \tag{2.52}$$

and the mean scalar dissipation rate is defined as

$$\widetilde{\chi} = 2D\left(\frac{\partial \widetilde{Z}}{\partial x_i}\frac{\partial \widetilde{Z}}{\partial x_i}\right). \tag{2.53}$$

A model for the scalar dissipation rate can be determined by considering its dimension, inverse time. Thus, the scalar dissipation rate is the inverse of the diffusion time scale, or diffusivity in mixture fraction space. One model for the scalar dissipation rate derived using this method is

$$\widetilde{\chi} = c_\chi \frac{\widetilde{\epsilon}}{\widetilde{k}} \widetilde{Z''^2}, \tag{2.54}$$

where c_χ is a constant often taken as 2.0 [23].

2.3.2 Infinitely fast chemistry

In non-premixed turbulent combustion, the limiting time scale for the chemistry process is the time required for convection and diffusion. This occurs because the chemical time scale that characterizes the reactions is much smaller than the time scale of convection and diffusion. As a result, in many non-premixed combustion cases, it is reasonable to assume infinitely fast combustion for the study of global properties [27]. Using this assumption it is possible to create a combustion model that relates a conserved scalar to reactive scalars.

A common combustion model that utilizes the infinitely fast chemistry assumption is the Eddy Dissipation Concept (EDC) model developed by Magnussen [28]. The purpose of the EDC model is to provide closure for the mean chemical source term. For the EDC model, closure of the mean reaction rate is given by

$$\bar{\dot{\omega}}_1 = A\bar{\rho}\frac{\epsilon}{k} min\Big(\widetilde{Y}_1, \frac{\widetilde{Y}_2}{S}, B\frac{\widetilde{Y}_3}{1+S}\Big), \tag{2.55}$$

where A and B are adjustable parameters, subscripts 1, 2, and 3 denote the fuel, oxidizer and products respectively, and S represents the oxygen-fuel stoichiometric mass ratio [8]. A similar expression can be found for LES using the filtered quantities. The EDC model has the advantage of including finite rate kinetics at lower computational cost when compared to other combustion models. However, this computational saving comes at a price. First, the parameters A and B are not universal and require adjustments for each flame [8]. As a result, this model requires validation for each flow. Second, the model presents a less accurate description of turbulent temperature fluctuation [29].

Another limitation of the EDC model is that it cannot handle finite-rate chemistry in its base form. This limitation can be avoided by including information on the chemical reaction. This is accomplished by replacing the mixing timescale, k/ϵ, with $k/\epsilon + \tau_{chem}$, where τ_{chem} is some measure of the chemical time scale. This modification has allowed the EDC model to be considered for practical calculations for diesel combustion with detailed chemistry [8]. However, the modified equation still requires A and B to be determined for each flame.

2.3.3 Laminar Flamelet model

This method was independently derived by Peters [30] and Kuznetsov [31]. The Laminar Flamelet model assumes that turbulent diffusion flames consist of an ensemble of stretched laminar flamelets [32]. For non-premixed combustion the Favre-averaged mass fraction

species k is calculated using

$$\widetilde{Y}_k(x,t) = \int_0^1 \int_0^\infty Y_k(Z,\chi_{st},t)\tilde{P}(Z,\chi_{st},x,t)d\chi_{st}dZ, \tag{2.56}$$

where χ_{st} is the scalar dissipation at the flame surface, $\tilde{P}(Z,\chi_{st},x,t)$ is a presumed-PDF and $Y_k(Z,\chi_{st},t)$ is an ensemble of laminar flamelets at different strain rates and is tabulated prior to the CFD calculations. The limitation of the Laminar Flamelet model is that it is limited to the flamelet regime. In the flamelet regime the integrity of the flame structure is preserved and the turbulent eddies do not strongly distort the structure of the flame. Thus, in the flamelet regime the local structure of the flame sheet is the same as a laminar flame to a very good approximation [8].

2.3.4 Conditional Moment Closure (CMC)

CMC was first proposed independently by Bilger [33] and Kilmenko [34]. In non-premixed combustion, the conditioning variable is often chosen as the mixture fraction. Thus, in CMC, the value for the mean scalar is found using,

$$\widetilde{f} = \int_0^1 \langle f|\eta\rangle \widetilde{P}(\eta)d\eta, \tag{2.57}$$

where $\langle f|\eta\rangle$ is the conditional average of $\widetilde{f}$ determined by solving the CMC equations, η the sample space variable of Z, and $\widetilde{P}(\eta)$ a presumed PDF. For brevity, the CMC equations are not given, but can be found in [33, 34].

The main advantage of using conditional averages is that the fluctuations about the conditional average are much smaller than their unconditioned counterparts. In CMC, the transport equations are solved in mixture fraction space resulting in unclosed conditional quantities, such as conditional velocity, $\langle u_i|\eta\rangle$, conditional turbulent flux, $\langle u_i^{''}Y_k^{''}|\eta\rangle$ and conditional chemical source term $\langle\omega_k|\eta\rangle$. In first order CMC the fluctuations about the conditional mean are assumed to be negligible. Closure for the chemical source term is obtained using

$$\langle\dot{\omega}_k|\eta\rangle \simeq \dot{\omega}(\langle Y_k|\eta\rangle, \langle T|\eta\rangle, \langle\rho|\eta\rangle). \tag{2.58}$$

Thus, the conditional chemical source term is a function of conditional scalars which can be determined. The assumption that the conditional fluctuations can be neglected, can be avoided by using the second-order CMC approach [8]. Additionally, CMC has been

shown to perform well for various non-premixed flames [16, 35] and MILD burners [36]. However, since the CMC equations contain unclosed terms and an additional dimension for each conditioning variable introduced, the computational cost of the CMC approach is significantly higher than the laminar flamelet approach. The advantage of CMC over flamelet models is that it is not restricted to the flamelet regime.

2.3.5 PDF methods

The joint PDF transport equation model was first proposed by Pope [37]. In this method, a transport equation for the joint PDF of velocity, viscous dissipation and reaction scalars is solved. This transport equation does not contain any information on the mixing time resulting in an unclosed term that requires modelling [23]. Thus, closure of the mixing term is required. The main advantage of the joint PDF transport equation model is the chemical source term appears in closed form and no closure model is required. Further, this model does not make any fast chemistry assumptions, is valid for premixed and non-premixed combustion and currently is one of the most complete descriptions of turbulent reaction flows [8]. It is possible to provide closure to the mixing term by including scalar gradients in the transport equation at the cost of higher dimensionality and computational cost. Pope developed the Monte-Carlo simulation technique, using Lagrangian methods [38], to reduce the computational cost. In the Monte-Carlo method, the fluid is seeded with virtual particles. By using a random walk method the evolution of these particles are modelled and represent the macromixing. Using stochastic or deterministic models including micromixing the scalar concentration are then solved. Similar to other turbulent combustion models the predictions depend on the quality of the closure models. The disadvantages of PDF methods are that they are computationally expensive, mathematically complex and providing closure for the mixing term is not simple.

2.3.6 Conditional Source-term Estimation

Conditional Source-term Estimation (CSE) is initially proposed by Bushe and Steiner [39] and is based on the same ideas used to derive CMC. Similar to the CMC method presented in Section 2.3.4, in non-premixed CSE, first order closure is applied and the mixture fraction is selected to be the conditioning variable. The major difference between the CMC and CSE approaches lies in how the conditional averages are found. Unlike CMC, which determines the conditional averages by solving transport equations, CSE obtains conditional averages via an integral inversion. Further detail on the derivation and

implementation is given in Chapter 3. The concept has been evaluated using $a - priori$ tests including DNS results [39, 40, 41]. CSE has been used for a few cases related to autoignition [42, 43, 44], premixed combustion [45, 46, 47], non-premixed combustion [48, 49, 50, 51, 52] and partially premixed combustion [53]. The formulation has significantly evolved from using a collection of flamelet libraries [42] to including chemistry manifold tabulations [50] with different regularization techniques to invert the necessary integrals. Some numerical and modelling aspects still need to be clarified and investigated. For example, CSE assumes spatial homogeneity for the conditional averages within a given ensemble, corresponding to a CSE domain. The influence of the number and size of CSE domains on the numerical predictions has not been thoroughly examined in previously published CSE studies. Further, CSE offers high potential to be extended more easily to partially-premixed combustion and multi fuel problems.

2.4 Moderate and Intense Low Oxygen Dilution (MILD) combustion

MILD Combustion belongs to high-temperature combustion technologies (HiCOT), which encompasses any technologies that use high temperature reactants. MILD combustion has been investigated world-wide as a method for increasing efficiency and reducing emissions. In this type of combustion a high temperature oxidizer stream is present and large quantities of flue gases are mixed with the fuel stream before ignition. This can be accomplished using a secondary burner to produce a high temperature, low oxygen, oxidizer stream [54, 55, 56] or using recirculation within the furnace to dilute the oxygen concentration in the reaction zone while having a high temperature and concentration of flue gases in the reaction zone [57]. In Japan, MILD combustion was called excess enthalpy combustion [58], whereas in Germany and the United States it has been called flameless oxidation [59, 60] and low-NOx injection, respectively. A schematic for MILD combustion is presented in Figure 2.1.

As can be seen in Fig. 2.1, in both High Temperature Combustion and MILD combustion the temperature of the reactant is above the self-ignition temperature, T_{Si}. For the process to be considered MILD combustion an additional constraint, the temperature increase within the combustion process, ΔT, is lower than T_{Si} must also be met. In comparison, feedback combustion has low reactant temperatures and large temperature increases. It is important to note that unlike feedback and high temperature combustion, MILD combustion is not able to be sustained without the preheating of the reactants [6]. In both

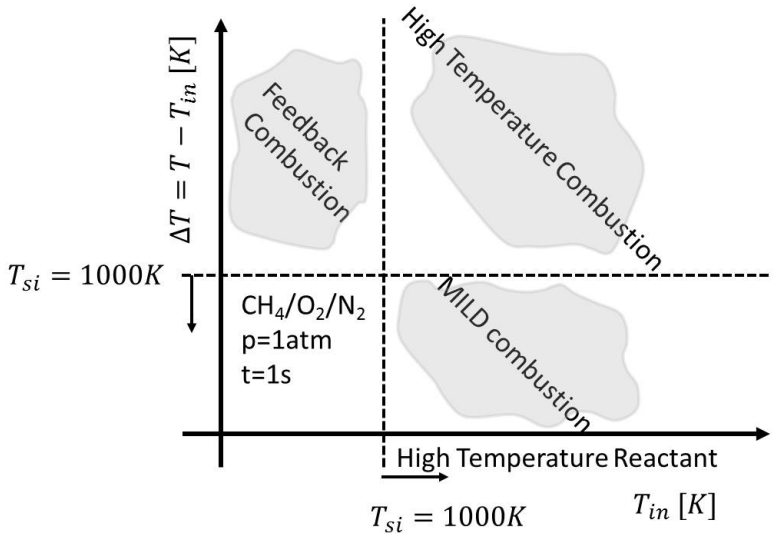

Figure 2.1: Inlet temperature (Tin)-maximum temperature increase (ΔT) locus of different combustion modes for a methane/oxygen/nitrogen, well stirred reactor (WSR) mixture reproduced from [6]. T_{Si} is the self-ignition temperature

feedback and high temperature combustion, the heat released by the combustion process is sufficient to maintain the process even if the preheating of the reactants is removed.

Oberlack et al [61] and Peters [62] provide a second definition of MILD combustion for a well stirred reactor based on the behavior of the ignition and extinction points. They define MILD combustion as the conditions where a monotonic shift from unburnt to burnt is observed and both the ignition and extinction points no longer exist.

2.5 Previous simulations of MILD combustion

The development of models for MILD combustion has mainly focused on the extension of existing non-premixed models. Various combustion models such as the EDC, flamelet, CMC and transported probability density function have been used with varying degrees of success.

MILD combustion has been experimentally studied on laboratory and industrial scales. For laboratory-scale burners, two different experimental data sets, the Delft-Jet-in-Hot-Coflow (DJHC) [54, 55] and the Adelaide burner [56], have been used to evaluate the performance of different combustion models simulating MILD combustion. De et al. [29]

performed RANS simulations using an Eddy Dissipation Concept (EDC) model to simulate the DJHC flames. In this work the lift-off heights were underpredicted using the EDC model and the temperatures were found to be significantly overestimated compared to the experimental data. De et al. [29] found that improved prediction could be obtained by tuning either the volume fraction constant or the time scale constant. In the LES framework, Kulkarni and Polifke [9] modelled the DJHC burner using a transported Probability Density Function (PDF) approach including stochastic fields with two mixture fractions. Significant improvement in the predicted lift-off heights were obtained compared to the RANS simulations, but the temperatures were overpredicted downstream of the burner. Recently, Bhaya et al. [63] using different transported PDF models simulated the DJHC flames. The ignition kernel formation mechanism and trend of decreasing lift-off height with increasing jet Reynolds number were correctly reproduced. However, the lift-off heights were underpredicted and the temperature was higher than the experimental data. Similar to the DJHC flames, the Adelaide burner has been studied extensively using RANS and LES simulations. Conditional Moment Closure (CMC) has been used to model to the Adelaide burner [36] using a single mixture fraction and modified PDF. Good agreement with the experimental data was obtained, but NO concentrations were underestimated. Christo and Dally [64] showed that single conserved scalar-based models are unable to accurately model the Adelaide burner. In the LES framework, Ihme and See [65] extended the flamelet/progress variable approach to model the Adelaide burner, by including two mixture fractions. The inclusion of a second mixture fraction was found to significantly improve the predictions and a second mixture fraction was required to accurately model the variations present in the coflow. In addition, laboratory-scale furnaces have been experimentally and numerically studied. Coelho and Peters [66] simulated the furnace experimentally studied by Plessing et al. [67] using a Eulerian particle flamelet model and obtained NO predictions in good agreement with the experimental data. For larger scale furnaces, Kim et al. [68] compared different global reaction mechanisms for a 2 m x 2 m x 6.25 m furnace using an EDC model. Mancini et al. [60] modelled the same furnace using an Eddy-break-up model, an EDC model and a PDF/mixture fraction model and found all predictions were of good quality

2.6 Summary

This section presents relevant background required for the proposed research. Information on turbulence modelling and combustion modelling is presented. MILD combustion modelling is an extension of traditional non-premixed combustion modelling. Various com-

bustion models such as CMC, Flamelet and EDC have been used to model mild combustion problems. The Flamelet model has been extended to include a second conserved conditioning scalar with promising results. However, the Flamelet model is limited to the flamelet regime. The CMC method has also been extended to MILD combustion problems by modifying the presumed PDF. However, determining the modified PDF is not necessarily straightforward or simple. Further, extending CMC to include a second conserved conditioning scalar results in more complicated transport equations for the conditional averages, with additional unclosed terms which require closure.

CSE can be extended to include a second conserved conditioning scalar, but is simpler than CMC as no transport equations are required for the conditional averages. Further, CSE is not limited to the flamelet regime giving it an advantage over flamelet models. CSE also been successful in modelling non-premixed flames [48, 49, 50, 51] which suggest that this method could be promising for modelling MILD combustion problems. The first step of developing a CSE combustion model is to test the CSE non-premixed combustion model and determine the sensitivity to the inversion parameters. The following chapter describes the investigation of the CSE method for non-premixed combustion and a sensitivity analysis of the inversion parameters.

Chapter 3

CSE for turbulent non-premixed combustion

The flame under consideration is the confined turbulent methane-air flame investigated by Brookes and Moss [69] in atmospheric conditions. Although the experimental study is focused on soot measurements at atmospheric and high pressures, it provides some experimental conditions and data useful for model comparison without considering soot modelling. Methane is the hydrocarbon fuel producing the lowest soot amounts compared to other hydrocarbons. For the atmospheric turbulent flame, Brookes and Moss [69] report soot levels comparable to those found in laminar diffusion methane flames: the peak values of soot volume fraction approximately range between 0.07 ppm and 0.16 ppm for heights of 300 mm to 425 mm (425 mm, being the axial position where the peak temperature reaches the centreline). Further, soot is only observed in the downstream region of the flame after 300 mm. Thus, a lot of soot-free experimental measurements are available for axial positions between the nozzle exit until 300 mm downstream of the fuel exit. Another advantage related to the choice of methane for the fuel resides in the chemical kinetics being better known as compared to other hydrocarbon fuels. The inflow conditions are well specified in the experiments, the selected confined flame does not impinge on the enclosure and the experimental set-up is axisymmetric resulting in a straightforward computational domain and simple boundary conditions. Experimental data is available for mean mixture fraction, temperature, soot volume fraction and spectral radiation intensity. Comparisons with the mixture fraction can give a good indication of how well the turbulent mixing field is predicted. The temperature is mostly affected by concentrations of the major product species, carbon dioxide (CO_2) and water (H_2O). Thus, temperature comparisons indirectly provide information on the accuracy of the CO_2 and H_2O predictions. Further,

the same flame is also used for comparison in previous numerical studies including the eddy dissipation model [70], the flamelet model [17] and CMC [16, 35]. The availability of experimental data and previous modelling results will serve as a good foundation for further comparison and analysis using the current CSE results. In the present work, soot formation is not included and soot modelling is beyond the scope of the present study. However, the radiative loss due to the main combustion product species H_2O and CO_2 is included in the calculations.

To summarize, the objectives of the present chapter are

1. Assessment of the impact of the main numerical parameters in CSE such as the number of CSE ensembles and the ensemble size used for inversion
2. Comparison of the CSE numerical predictions with available experimental data and results from previous simulations for the selected flame.

3.1 CSE

3.1.1 Model formulation

Similar to the CMC approach, CSE uses conditional averages to determine the Favre-averaged quantities in a turbulent reacting flow. In non-premixed combustion the conditioning variable is commonly selected to be mixture fraction, Z. As a result, the conditional average of any quantity, such as species concentration, enthalpy or temperature, at a particular value of η, in mixture fraction space, is considered. In the present work, the conditional fluctuations are assumed to be negligible leading to first order closure for the conditional chemical source terms. This simplification is commonly used in CMC and has been proven to be a reasonable assumption for attached jet flames far from extinction and without ignition [24, 71, 72], corresponding to the selected experimental conditions [69]. Thus, the conditional chemical source term of any species k, $\langle \dot{\omega}_k | \eta \rangle$, may be expressed as

$$\langle \dot{\omega}_k | \eta \rangle \simeq \dot{\omega}(\langle Y_i | \eta \rangle, \langle T | \eta \rangle, \langle \rho | \eta \rangle), \tag{3.1}$$

where $\langle Y_i | \eta \rangle$ is the conditional mass fraction for species i, $\langle T | \eta \rangle$ the conditional temperature and $\langle \rho | \eta \rangle$ the conditional density. However, in contrast to CMC, $\langle Y_i | \eta \rangle$ and $\langle T | \eta \rangle$ needed in Eq. 3.1, are not obtained by solving transport equations. Instead, only transport equations for Favre-averaged species concentrations are included in the calculations (see

Section 3.2.2). Thus, in CSE, the determination of the mean unconditional reaction rate for each species, $\overline{\dot{\omega}_k}$, is the key step using

$$\overline{\dot{\omega}_k}(x_j,t) = \bar{\rho}\int_0^1 \frac{\langle\dot{\omega}_k|\eta\rangle}{\langle\rho|\eta\rangle}\widetilde{P}(\eta,x_j,t)d\eta, \tag{3.2}$$

where x_j is the spatial coordinate, t the time and $\widetilde{P}(\eta)$ the Favre-averaged PDF of mixture fraction. In the present study, a presumed β-PDF distribution is used to model $\widetilde{P}(\eta)$ [73]. The β-PDF is calculated using

$$\beta_{pdf}(x,a,b) = \frac{1}{B(a,b)}x^{a-1}(1-x)^{b-1}, \tag{3.3}$$

with a and b the parameters that define the shape of the PDF. B(a,b) is the β-function calculated using

$$B(a,b) = \frac{\Gamma(a)\Gamma(b)}{\Gamma(a+b)}, \tag{3.4}$$

where $\Gamma(x)$ is the gamma function. In Eq. 3.3, a and b are calculated as

$$a = \overline{x}\left(\frac{\overline{x}(1-\overline{x})}{\sigma^2}-1\right) \quad \text{and} \quad b = (1-\overline{x})\left(\frac{\overline{x}(1-\overline{x})}{\sigma^2}-1\right), \tag{3.5}$$

where $\overline{x}$ is the mean value of x, and σ^2 its variance. In order to calculate $\langle\dot{\omega}_k|\eta\rangle$, the conditional species mass fractions, $\langle Y_k|\eta\rangle$, are determined from the unconditional Favre-averaged values, $\widetilde{Y_k}$ by inverting the following integral,

$$\widetilde{Y_k}(x_j,t) = \int_0^1 \langle Y_k|\eta\rangle(\eta,x_j,t)\widetilde{P}(\eta,x_j,t)d\eta, \tag{3.6}$$

where $\widetilde{Y_k}$ and $\widetilde{P}(\eta)$ are known quantities determined by a transport equation and the β-function, respectively. Thus, in Eq. 3.6, the only unknown is $\langle Y_k|\eta\rangle$. In the following section, further detail is given for the inversion technique required in CSE.

3.1.2 Inversion method

Before inverting Eq. 3.6, some properties related to the conditional averages are considered. The conditional averages are assumed to be homogeneous within a known ensemble of

points. This assumption is based on the observation that conditional averages vary much less in space than unconditional averages [24, 74], which is commonly used in CMC [75, 76]. Thus, for a given ensemble of points, Eq. 3.6 can be rewritten as

$$\widetilde{Y_k}(x_j,t) = \int_0^1 \langle Y_k|\eta\rangle(\eta,t)\widetilde{P}(\eta,x_j,t)d\eta. \tag{3.7}$$

In practice, the ensemble of points corresponds to a subset of the computational grid. For example, Salehi et al. [45] select one ensemble covering the entire computational domain to simulate a premixed flame. In non-premixed turbulent combustion, the ensembles are typically a set of planes defined in the axial direction [42, 50] making use of the weak radial dependence of the conditional averages [24]. However, no rigorous sensitivity analysis has been reported showing how the number of the ensembles could affect the simulation predictions. This aspect will be investigated in Section 3.3.1.

Equation 3.7 is a Fredholm integral equation of the first kind. Using a numerical quadrature for the left-hand side of Eq. 3.7, it can simply be written in general form as

$$A \cdot \vec{\alpha} = \vec{b}, \tag{3.8}$$

where $\vec{\alpha}$ is the vector including $\langle Y_k|\eta\rangle$ at each η_m, m being the mixture fraction bin index, $\vec{b}$ is the vector containing $\tilde{Y}_k$ at each spatial position x_j and A is the matrix of integrated PDF over a mixture fraction interval, also called bin. It should be noted that A is a $N \times M$ matrix, where N is the number of points (grid nodes) in a given ensemble and M is the number of bins in mixture fraction space. In matrix notation, the values in A are given by

$$A_{jm} = \int_{\eta_1}^{\eta_2} \widetilde{P}(\eta_m, x_j, t)\ d\eta, \tag{3.9}$$

using j for the spatial coordinate index and η_1 and η_2 are the lower and upper bounds of the mixture fraction bin, respectively. The solution of Eq. 3.8 is ill-posed, which means the solution of Eq. 3.8 is sensitive to any small perturbations of the system [77]. Thus, in order to reach a smooth, stable and unique solution for $\vec{\alpha}$, a regularization method must be implemented. A general review on regularization methods for Fredholm equation of the first kind can be found in [77]. In the present work, Tikhonov regularization is adopted [78]. Other regularization methods exist and could also be applied, for example the Truncated Singular Value Decomposition (TSVD) [79]. The Tikhonov technique has been shown to provide a stable and unique solution in previous CSE studies [44, 45, 51]. Thus, this appears to be a suitable regularization tool for the present investigation. The solution of Eq. 3.8 is obtained using the following implementation based on the least-square technique

$$\vec{\alpha} = \arg\min\Big\{ \Big\| \mathbf{A}\vec{\alpha} - \vec{b} \Big\|_2^2 + \lambda^2 \Big\| I(\vec{\alpha} - \vec{\alpha}_0) \Big\|_2^2 \Big\}, \tag{3.10}$$

where $||.||_2$ denotes the L2-norm of a vector, I is the identity matrix , $\vec{\alpha}^0$ the solution from the previous time step [42], and λ the regularization parameter. Various initial values of $\vec{\alpha}^0$ have been tested [53] and the final solution does not depend on the initial value of $\vec{\alpha}^0$. The regularization parameter λ is calculated as

$$\lambda^2 = \frac{Tr(A^T A)}{Tr(I)}, \tag{3.11}$$

where Tr is the trace of the matrix [80].

Finally the values for $\vec{\alpha}$ are obtained using LU decomposition to solve Eq. 3.8. For the solutions to be realistic, $\vec{\alpha}$, the vector including the conditional species mass fractions, must contain only positive values since negative terms have no physical meaning. However, the present regularization method does not impose the positivity condition. In the current calculations, very small negative values are observed for very rich and lean conditions. In these regions, no significant chemical activity is expected and the erroneous values would have a negligible effect on the overall turbulent combustion modelling. In order to circumvent this nonphysical behaviour, any negative values for $\vec{\alpha}$ are set to zero. Bushe and Steiner also note the same issue of negative values for $\vec{\alpha}$ after regularization in their work and as a more general strategy, suggest removing any negative value and then apply a re-scaling to $\vec{\alpha}$ [40]. Thus, a rescaling is also implemented following the method described in [40] to find the scaling factor. The final values of $\vec{\alpha}$ noted by $\vec{\alpha}_{final}$, are obtained by

$$\vec{\alpha}_{final} = \vec{\alpha} \frac{\sum_j \widetilde{Y}_k \int_0^1 \langle Y_k|\eta\rangle \tilde{P}(\eta) d\eta}{\sum_j \left(\int_0^1 \langle Y_k|\eta\rangle \tilde{P}(\eta) d\eta \right)^2}. \tag{3.12}$$

The scaling factor, s, is monitored during the simulations and is shown to be between $0.90 \leq s \leq 1.10$, confirming the little impact of the scaling process.

To circumvent the problem related to the negative physical values, a different regularization method could be implemented. For example, Salehi et al. [45] use the same Tikhonov method but with a different expression for λ and TSVD [79] and obtain negligible differences in the results between the two methods.

It would still remain extremely computationally expensive to invert Eq. 3.7 for each species present in a detailed chemical mechanism such as GRI 2.11 including 49 species [81]. Instead, the chemistry is tabulated as a function of two variables, $\langle Y_{CO_2}|\eta\rangle$ and $\langle Y_{H_2O}|\eta\rangle$. Further detail is presented in Section 3.1.3. Thus, the inversion process is only required for two species mass fractions, $\langle Y_{CO_2}|\eta\rangle$ and $\langle Y_{H_2O}|\eta\rangle$. Once $\langle Y_{CO_2}|\eta\rangle$ and $\langle Y_{H_2O}|\eta\rangle$ are determined, the conditional reaction rates for each species $\langle \dot{\omega}_k|\eta\rangle$ is found from the chemistry tables. Finally, the unconditional reaction rates for each species k is determined by integrating the conditional reaction rates with the PDF using Eq. 3.2.

3.1.3 Chemistry tabulation

The chemical reaction rates are tabulated prior to the simulation using the Trajectory Generated Low Dimension Manifold (TGLDM) approach [82]. In the present study, the TGLDM method is based on the technique developed by Huang and Bushe [43] and Pope and Maas [82]. The principle is to start from a detailed chemistry mechanism that is reduced to low-dimensional manifolds in composition space. The resulting TGLDM manifold for each mixture fraction, η, is stored in tables using two variables, Y_{CO_2} and Y_{H_2O} selected due to their long formation times [43, 50]. The boundary of the manifold is calculated using conservation of elements, by determining the maximum and minimum values of Y_{H_2O} for given values of Y_{CO_2} based on a constant amount of initial fuel. The trajectories are solved using the governing Ordinary Differential Equation (ODE) equations starting at each boundary point using a stiff ODE system solver [83],

$$\rho \frac{\partial Y_k}{\partial t} = \dot{w}_k. \tag{3.13}$$

The calculations stop when chemical equilibrium is reached. Once the trajectories for TGLDM are calculated, redundant points are removed in order to reduce the size of the tables. Finally, in order to allow for easier location on the manifold, Delaunay triangulation is applied [84].

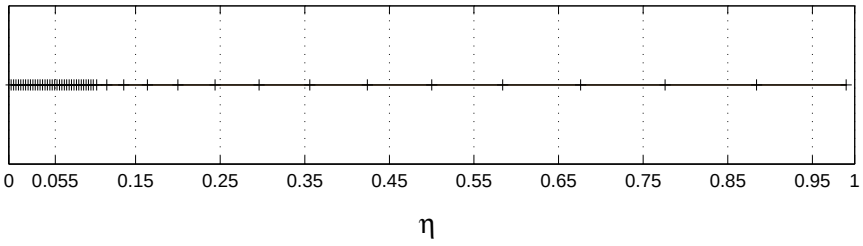

Figure 3.1: Mixture fraction sampling locations

In the present work, 50 TGLDM manifolds are tabulated for 50 different values of η ranging from 0.00286 to 0.99, with a greater concentration of values around the stoichiometric mixture fraction ($\eta_{st} = 0.055$) as shown in Fig. 3.1. One TGDLM manifold is

presented in Fig. 3.2 for the stoichiometric mixture fraction value. The detailed mechanism used is the GRI-MECH 2.11 [81] for methane-air combustion including 49 species with 277 reactions. To determine the conditional chemical source terms, two variables are required, $\langle Y_{CO_2}|\eta\rangle$ and $\langle Y_{H_2O}|\eta\rangle$, resulting in the inversion of two integral equations. Once the $\langle Y_{CO_2}|\eta\rangle$ and $\langle Y_{H_2O}|\eta\rangle$ variables are calculated the conditional reaction rates are determined for each value of η using Barycentric coordinates for interpolation [85].

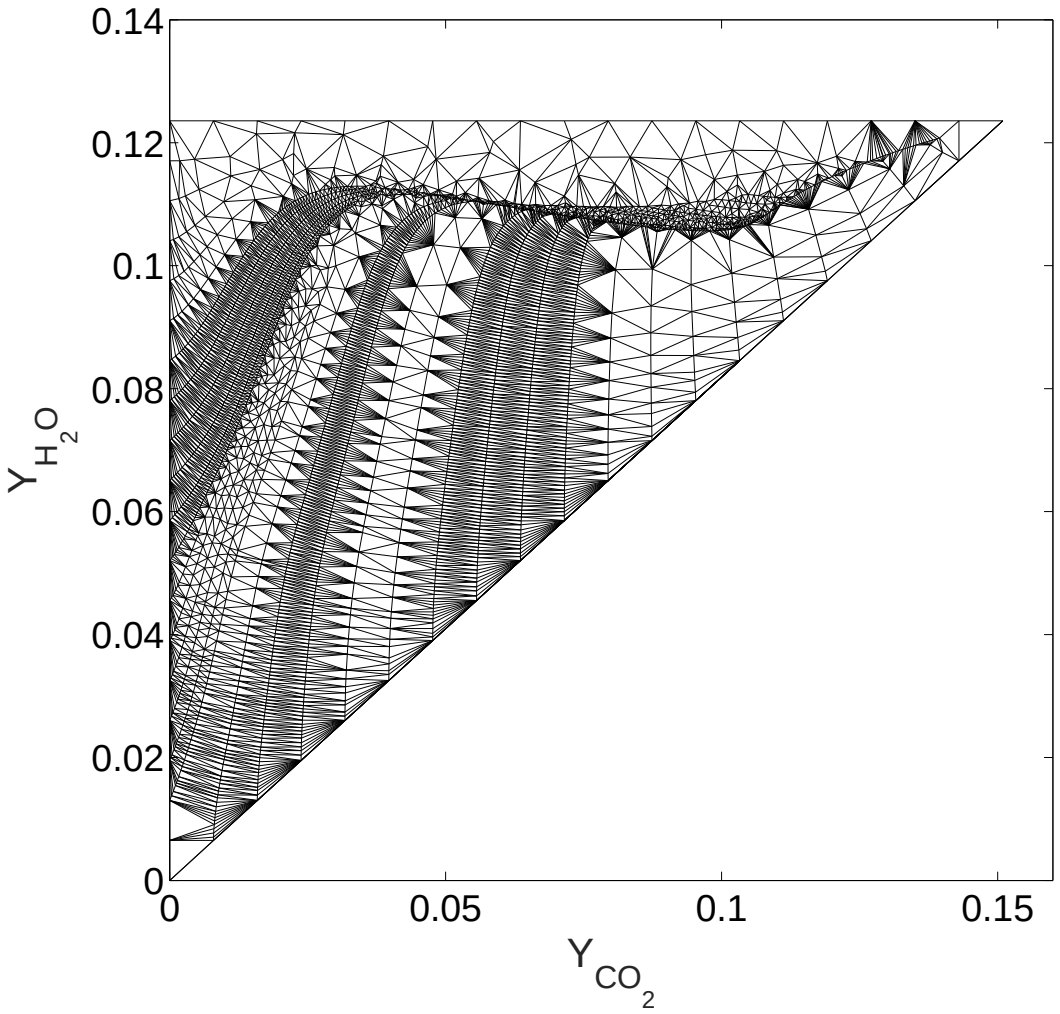

Figure 3.2: TGLDM with Delaunay triangulation for $\eta_{st} = 0.055$

3.2 Computational details

3.2.1 Experimental conditions

The confined methane-air flame at atmospheric conditions experimentally characterized by Brookes and Moss [69] is selected. The experimental setup consists of a cylindrical 4.07 mm diameter nozzle for the main fuel flow and an annular pilot nozzle with a width of 160 μ m surrounding the main nozzle. To prevent recirculation around the base of the flame a flow-straightening diffuser, consisting of two circular perforated metal plates are used. This provides a flat velocity for the coflowing air. A coflow of air is also present with a mass flow rate of 708 g/min [69]. The flame is confined by a 155 mm Pyrex tube and atmospheric air. The bulk velocity of the main fuel is 20.3 m/s, with a mass flow rate of 10.3 g/min and an exit Reynolds number of 5000. The main fuel and coflow air enter the combustion chamber at 290 K. The main fuel flow consists of pure methane. The experimental error on the mean mixture fraction measurements is reported to be equal to 6%.

3.2.2 CFD calculations

Following the experimental setup, the computational domain is cylindrical with a radius of 77.5 mm and a total length of 1000 mm. The geometry is created as a wedge of a small angle (θ =10°) with one cell in the θ direction, creating a two dimensional simulation. The grid is nonuniform with a high density of grid points located close to the nozzle and between 0 and 60 mm in the radial direction where the flame develops. Grid refinement is used at the wall to properly model the effects of the boundary layer at the wall. The current grid consists of 58,800 cells. The computational domain with the boundary conditions are shown in Fig. 3.3. Further refinements were made to the mesh and the present results are found to be grid independent. The inlet boundary conditions consist of non-premixed fuel supplied at 20.3 m/s at the main nozzle and a coflow of air with a velocity of 0.514 m/s. Adiabatic and no-slip wall conditions are applied to the walls and the outlet pressure is set to atmospheric. The RANS flow and continuity equations are solved using a finite volume low-Mach number pressure based approach using OpenFOAM [86]. Transport equations are solved for mass (continuity), momentum, enthalpy, and the Favre-averaged mass fraction of the major species (methane (CH_4), oxygen (O_2), H_2O, CO_2, carbon monoxide (CO), and hydrogen (H_2)).

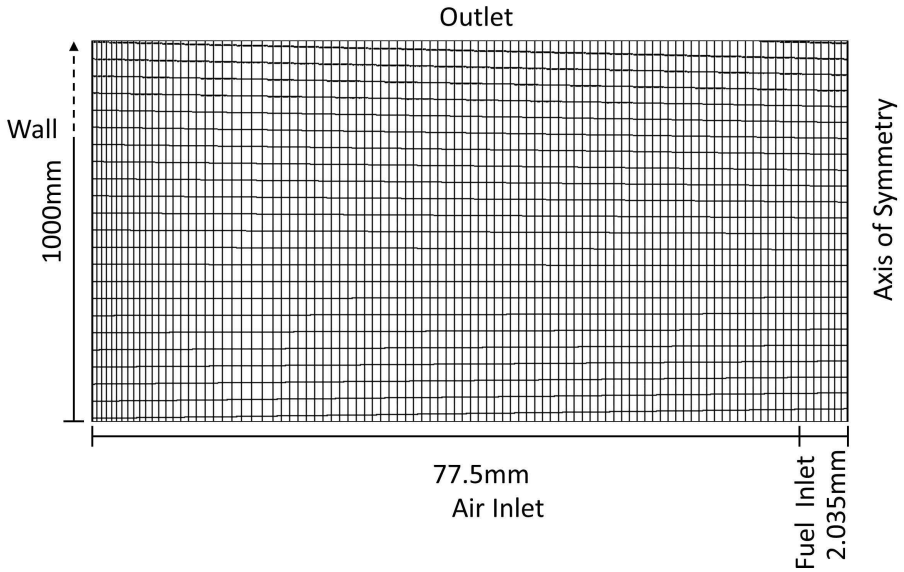

Figure 3.3: Computational grid (not to scale)

The transport equation for the Favre-averaged species mass fraction is given by,

$$\frac{\partial \bar{\rho}\widetilde{Y}_k}{\partial t} + \frac{\partial(\bar{\rho}\widetilde{u}_i\widetilde{Y}_k)}{\partial x_i} = \frac{\partial}{\partial x_i}\Big(\frac{\mu_t}{Sc_t}\frac{\partial \widetilde{Y}_k}{\partial x_i}\Big) + \bar{\dot{\omega}}_k, \tag{3.14}$$

where μ_t is the turbulent viscosity, Sc_t the turbulent Schmidt number and $\bar{\dot{\omega}}_k$ is the output from the CSE routines using

$$\bar{\dot{\omega}}_k = \int_0^1 \dot{\omega}_k^{TGLDM}\bar{P}(\eta)d\eta, \tag{3.15}$$

with $\dot{\omega}^{TGLDM}$ the conditional chemical source terms for species k, a function of $\langle Y_{CO_2}|\eta\rangle$ and $\langle Y_{H_2O}|\eta\rangle$ extracted from the TGLDM tables.

Transport equations for the mean mixture fraction $\tilde{Z}$ and variance $\widetilde{Z''^2}$ are also solved which are required to determine the presumed β PDF. A gradient assumption is used to close the turbulent transport terms. A schematic of how the CSE code and CFD solver are coupled is given in Fig. 3.4.

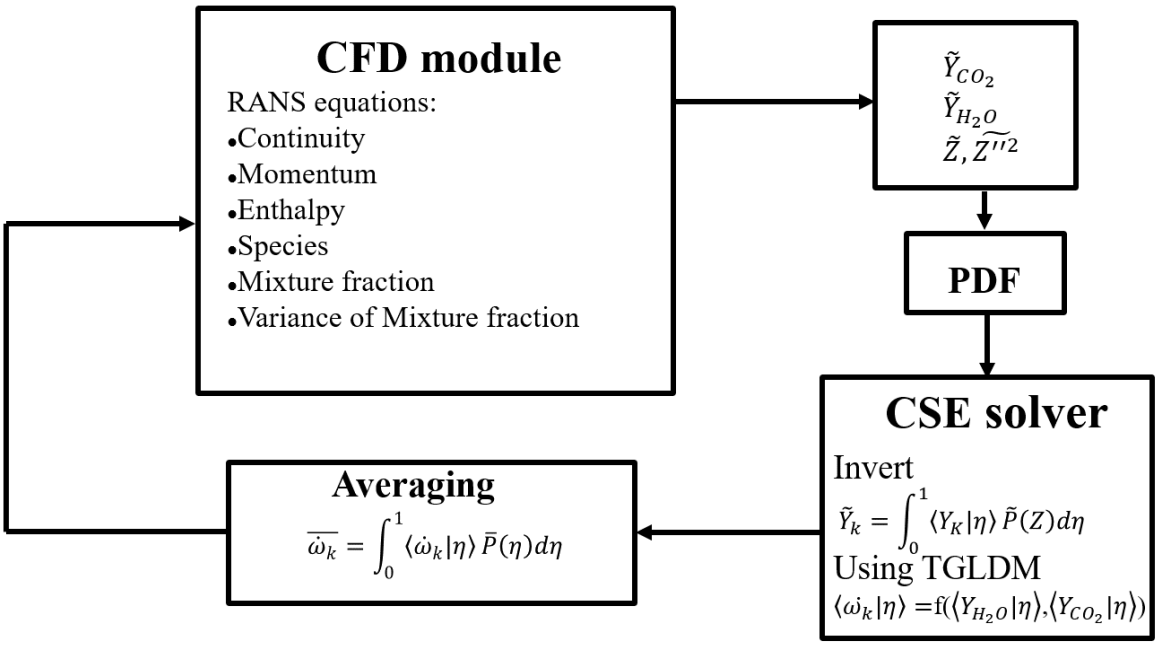

Figure 3.4: CSE code structure.

In order to determine the sensitivity of the simulation to changes in the turbulent intensity at the inlet, three simulations with different turbulent intensities ranging from 5 to 20% are tested. The mixture fraction profiles obtained from the simulation with 5% turbulent intensity are in best agreement with experimental measurements near the nozzle. Farther downstream the effect of the inlet turbulent intensity is negligible. As a result, the inlet turbulent intensity is set to 5% for the remaining simulations.

In addition, two turbulent Schmidt numbers, 0.7 and 0.9 are tested. The value of 0.7 was found to produce results in better agreement with the experimental data. Thus, a turbulent Schmidt number of 0.7 is used for the remaining simulations.

The radiation effects are included in the present simulations using an optically thin radiation model. The radiative heat loss due to H_2O and CO_2 is only considered and curve fitting to used determine the Planck absorption coefficients, $a_{p,i}$, as a function of H_2O and CO_2. The parameters for the curve fitting are found on the Sandia website (http://www.sandia.gov/TNF/radiation.html). Once the Planck absorption coefficients

are determined, the radiative heat loss, Q is calculated as

$$Q = Q(T, Y_k) = 4\sigma\Big(\sum_{1}^{n_r} p_k * a_{p,k}\Big)(T^4 - T_\infty^4), \tag{3.16}$$

where σ is the Stefan-Boltzmann constant, p_k is the partial pressure of species k in atmospheres, T is the local flame temperature (K) and T_∞ is the background temperature [87]. Soot concentrations are very small in the selected flame under atmospheric conditions [69]. Thus, no soot model is incorporated and radiation due to soot is also neglected.

3.2.3 Turbulence models

Two turbulence models are used in the simulations. The first of these is the $k-\epsilon$ model [12]. The standard $k-\epsilon$ model is well-known to overpredict the spreading rate in round jets [13, 14]. To correct this problem, several strategies can be applied. Modifying the value of $C_{\epsilon 1}$ is one possibility. For non-reacting jets, Dally et al. [15] have shown that a $C_{\epsilon 1}$ value of 1.6 better predicts the characteristics of these flows. This correction is also commonly applied to non-premixed jet flames [16, 17]. The sensitivity analysis applied to the flame under investigation results in a optimal value of 1.47 for best agreement with experimental data for mixture fraction and temperature. Thus, $C_{\epsilon 1}$ equal to 1.47 is kept for the remaining simulations.

In addition to the $k-\epsilon$ approach, the Re-Normalization Group (RNG) $k-\epsilon$ model [88] is also included for further comparison. The RNG $k-\epsilon$ turbulence scheme models the effects of small-scale turbulence by including a random forcing function to the Navier-Stokes equations.

The experimental study does not report any buoyancy effects [69]. Thus, no buoyancy correction is added to the turbulence model equations, also following what is done in previous numerical simulations for the same flame [17, 35, 70].

3.2.4 CSE initialization

CSE uses $\langle Y_{CO_2}|\eta\rangle$ and $\langle Y_{H_2O}|\eta\rangle$ as variables to determine the chemical source terms. However, at the start of the simulation there is no CO_2 or H_2O in the CFD domain. Consequently, some initial values for the mass fractions of CO_2 or H_2O must be set. The chemical source terms are determined using an assumed form for $\langle Y_{CO_2}|\eta\rangle$ and $\langle Y_{H_2O}|\eta\rangle$. For the initial time steps, conditional values are not determined by inversion, instead the initial profiles for $\langle Y_{CO_2}|\eta\rangle$ and $\langle Y_{H_2O}|\eta\rangle$ are selected such that they lie within the

fully burning portion of the TGLDM manifold. This ensures that the conditional and unconditional chemical source terms calculated from the TGLDM table are large. Once the mass fractions of CO_2 and H_2O in the CSE domains have reached a level where the reaction is self-sustaining, the initialization process is turned off and the conditional profiles for CO_2 and H_2O are calculated using the inversion process.

3.3 Results

3.3.1 Sensitivity to CSE ensemble number

As described in Section 3.1.2, the conditional averages are assumed to be homogeneous for a given assemble of points. That means that the computational grid may be divided into subdomains (CSE ensemble) to represent these ensembles. This approach is similar to the idea of defining a separate grid for conditional averages superimposed on the CFD mesh in CMC calculations [24]. The number of CSE ensembles may have an impact on the final species and temperature predictions.

In this section, a sensitivity analysis is performed by progressively increasing the number of CSE ensembles in the simulations until no significant change in the Favre-averaged temperature and species concentrations is observed. To this end, five sets of simulations are completed including 3, 6, 12, 24 and 32 CSE ensembles. The CSE ensembles are created over the same CFD grid domain, between 0 and 725 mm in the axial direction, keeping the entire radial distance and with a slight overlap between the ensembles. All other computational and modelling parameters are kept the same. The CSE ensemble overlap is included to prevent any sharp changes in the conditional averages and the resulting chemical source terms in the species transport equations. It should be noted that the present results are only used to evaluate the relative change induced by the number of CSE ensembles and are not compared with experimental results. Thus, radiative heat loss is not included for these simulations for computational efficiency. Further, the CSE ensembles are always defined following the axial direction, being cut in the direction normal to the centreline of the jet. This is explained by the fact that the conditional averages are known to vary more strongly in the axial direction and much less in the radial direction [24].

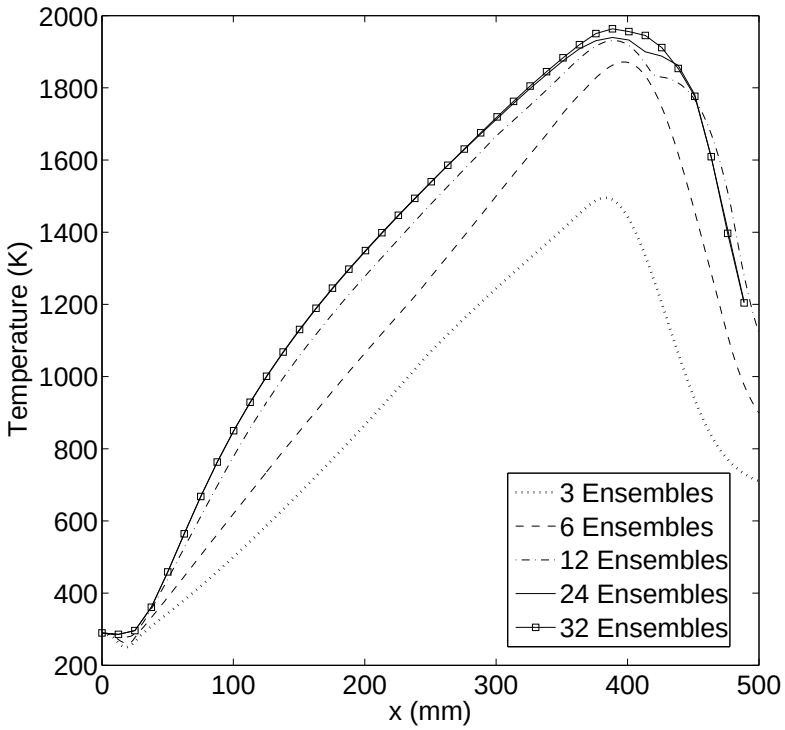

Figure 3.5: Centreline temperature profiles for different numbers of CSE ensembles

The predicted axial centreline temperatures are shown in Fig. 3.5 and the radial profiles are included in Fig. 3.6. As can be seen in Figs. 3.5 and 3.6, the predictions converge to a single temperature profile with increasing number of CSE ensembles. It is clear that a significant variation can be observed between 3 and 32 CSE ensembles. For example, at 150 mm the difference is approximately 500K corresponding to a 50 % relative change. Farther downstream, at 425 mm the temperature change is approximately equal to 700 K, i.e. $\simeq$35 % difference between these two sets of calculations. However, the temperature variation using 24 and 32 ensembles is small: less than 3K at 150 mm and approximately 26K at 450 mm. At all positions the relative change is less than 1%, expected to be well within any experimental uncertainty. In Fig. 3.6 the temperatures profiles for 24 and 32 ensembles coincide for most points and cannot be easily distinguished. Thus, it can be concluded that the solution obtained with 24 CSE ensembles has converged to a single set of temperature profiles.

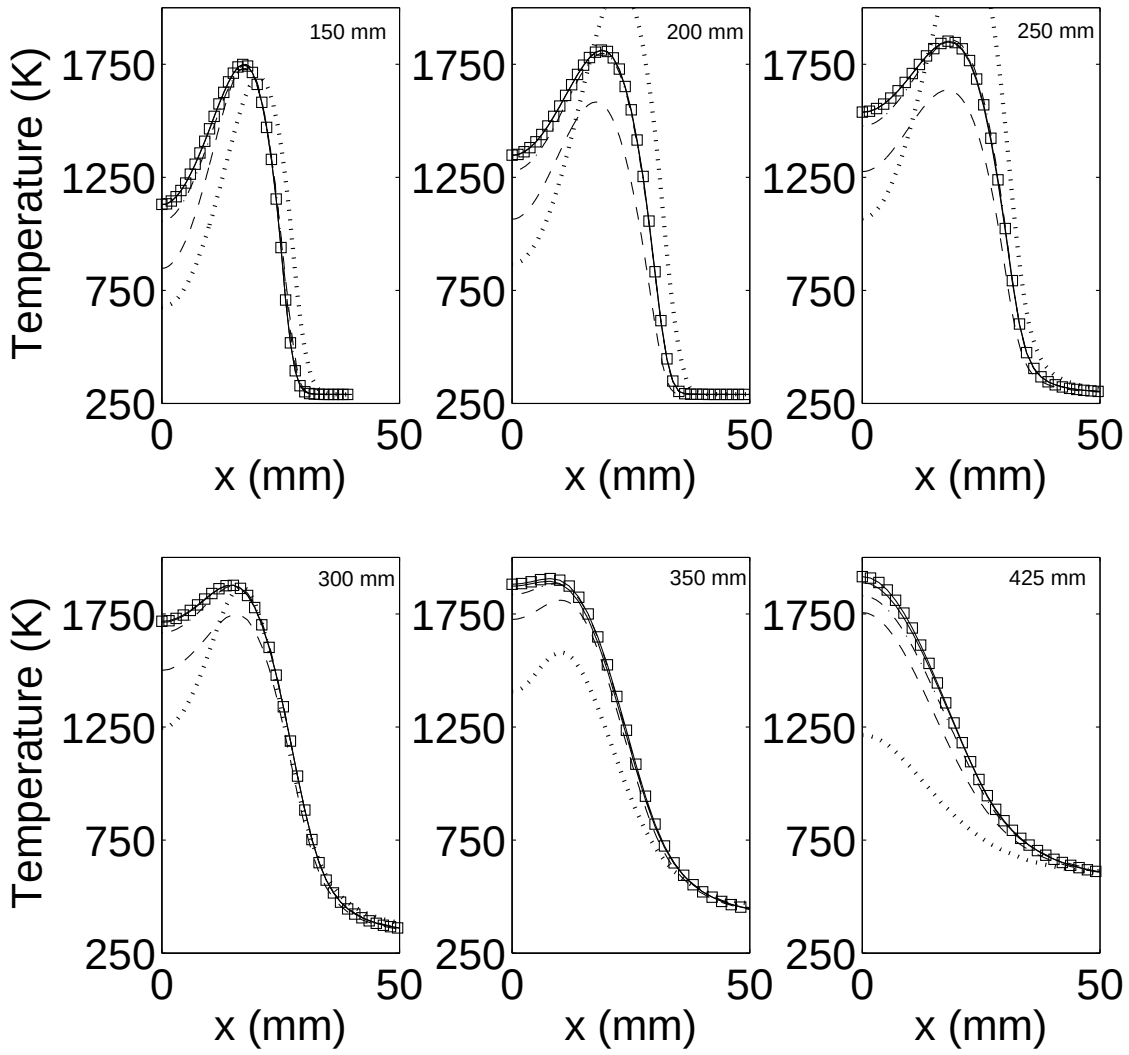

Figure 3.6: Radial temperature profiles for different numbers of CSE ensembles at different axial positions, same symbols as in Fig. 3.5

In addition to comparing the Favre-averaged temperature profiles for different CSE ensembles, the conditional species mass fractions are also examined. Figure 3.7 shows $\langle Y_{CO_2}|\eta\rangle$ extracted at the same axial position (280 mm) for the different CSE ensembles.

As for the Favre-averaged temperature profiles, as the number of CSE ensembles increases, the conditional CO_2 mass fraction profiles converge to one profile. This trend further demonstrates that the number of CSE ensembles used for the simulation is important. If too few ensembles are included, the conditional averages in those ensembles are far from the converged solution and provide poor simulation results. Similarly, if too many ensembles are used the computational cost increases unnecessarily. Consequently, it is important to find the minimum number of CSE ensembles that produces an independent solution.

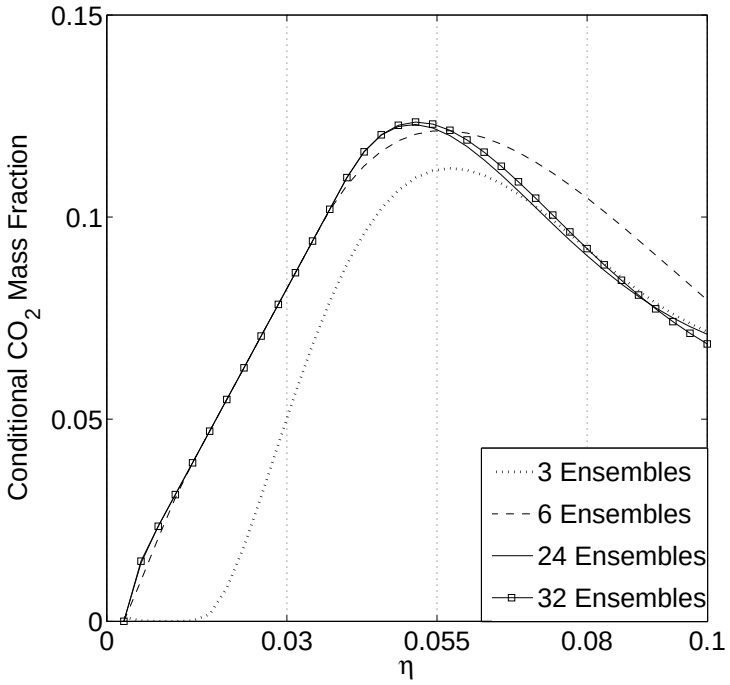

Figure 3.7: Conditional CO_2 mass fraction profiles for different numbers of CSE ensembles

For the present simulation the temperature profiles predicted by the 24 and 32 CSE ensemble simulations are almost identical. The computational time for 32 CSE ensembles is approximately 30 % larger than that needed for 24 ensembles to obtain a converged solution. Thus, 24 CSE ensembles are selected for the remaining simulations in order to save computational time. It should be noted that the simulations are carried out in parallel via domain decomposition, however each inversion process is computed using a single processor. In the current work, parallel implementation of the inversion process is not

considered. Further study is required to determine the benefits of a parallel implementation of the inversion process.

3.3.2 Sensitivity to the mean mixture fraction range

In this section and the remaining analysis, radiation losses due to H_2O and CO_2 are included in the simulations. As presented in Section 3.1.2, CSE obtains $\langle Y_{CO_2}|\eta\rangle$ and $\langle Y_{H_2O}|\eta\rangle$ by performing two integral inversions. Beyond the selection for the number of CSE ensembles, it is also possible to define a criterion to determine which cells are selected for the inversion process. For example, the mean mixture fraction may be used, i.e. a computational cell is included in the inversion process if its mean mixture fraction falls within a predetermined range. The main advantage of restricting the ensemble size is the potential saving in computational time. To determine if the CSE results are sensitive to the mixture fraction range used in the inversion process, two test cases are run. For Test Case 1 the range is set to $0.015 < \tilde{Z} < 1$. The lower limit is determined such that mixtures very close to pure air are excluded in the inversion. Initially, the calculations are run with all the cells in the ensemble only excluding pure air and pure fuel, i.e. $0 < \tilde{Z} < 1$. The lower bound is progressively increased to 0.015. For this lower bound value, no significant difference can be noticed when the final predictions are compared with those using $0 < \tilde{Z} < 1$. The upper bound is not modified as there are fewer cells with fuel-rich mixtures compared to those with fuel-lean mixtures. A different strategy is applied to Test Case 2. The mean mixture fraction range is determined using upper and lower flammability limits of methane in air at atmospheric pressure and a temperature equal to 293K, which are approximately 4.5% and 16% on a volume percentage [89], corresponding to mixture fraction values of approximately 0.026 and 0.096. In the current calculations, the range is slightly extended to $0.022 < \tilde{Z} < 0.11$ to ensure that all flammable mixtures are included within possible uncertainties in the calculation of the flammability limits.

To examine the effects of changing the mixture fraction range used for the inversion process, the centreline and radial temperature profiles are compared for the two test cases with the experimental data [69] and are shown in Fig. 3.8 and 3.9, respectively. As can be seen in Fig. 3.8, close to the nozzle, for axial positions between 0 and 50 mm, the centreline temperature profile shape and magnitude for the two test cases are very similar. However, farther downstream the two sets of predicted temperature are clearly different. At an axial position of 250 mm the temperature predicted in Test Case 2 underpredicts the experimental value by approximately 300 K at 250 mm, whereas that from Test Case 1 overpredicts the experimental data by 125 K. Best agreement with the experimental values is obtained with the temperatures retrieved from Test Case 1. As shown in Fig.

3.9, the radial temperatures profiles predicted by Test Case 2 are consistently lower than the experimental data. In contrast, Test Case 1 tends to overpredict the temperatures compared to the experiments, except for axial positions between 300 and 425 mm where the temperatures are underpredicted for radial locations larger than 40 mm. However, Test Case 1 still provides temperatures much closer to the experimental values.

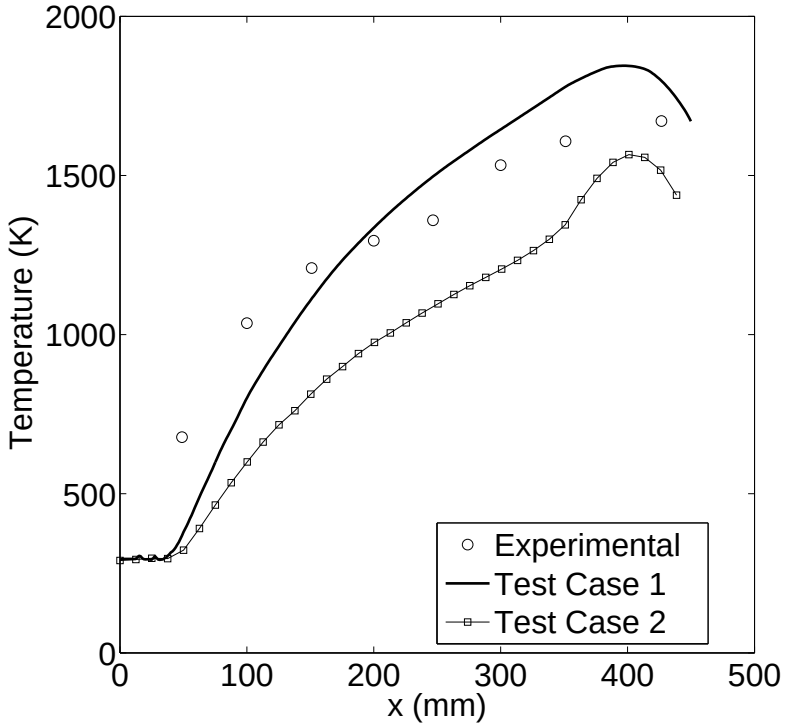

Figure 3.8: Centreline temperature profiles for different CSE inversion ranges compared with experimental data [69]

According to the observations made from Figs. 3.8 and 3.9, the bounds of the mixture fraction range has an impact on the temperature predictions. If the ensemble size is too small, the inversion yields erroneous values for the conditional averages leading to inaccuracies in the mean chemical source terms and Favre averages. The lower and upper bounds of the mean mixture fraction range needs to be selected with care. For the present conditions, the flammability limits cannot be used to define the ensemble size. The major assumption is that the conditional averages are homogeneous for a given ensemble. If too many cells are excluded, the validity of spatial homogeneity breaks down, i.e the

conditional averages are homogeneous within the ensemble however, they will be equal to different values outside the ensemble. Thus, the mean mixture fraction range included in Test Case 1 is kept for the remaining calculations: negligible differences in the predicted temperatures compared to those with $0 < \tilde{Z} < 1$ and significant computational saving is achieved: approximately 20% additional computational time is required for the full range of mixture fraction compared to using $0.022 < \tilde{Z} < 0.11$.

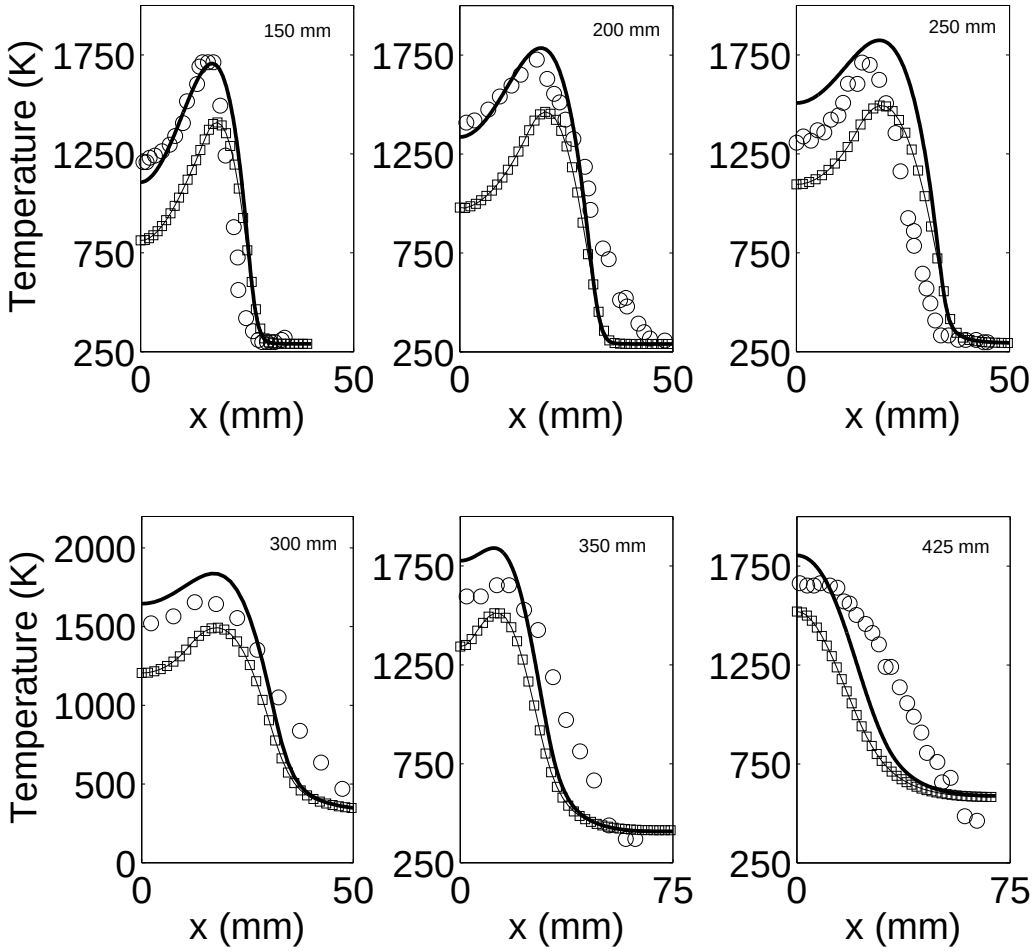

Figure 3.9: Radial temperature profiles at different axial positions for different CSE inversion ranges compared with experimental data [69], same symbols as in Fig. 3.8

3.3.3 Turbulent mixing field

Figure 3.10 shows the predicted centreline mixture fraction profiles using both turbulence models, the modified k-ϵ model with $C_{\epsilon_1} = 1.47$ and RNG k-ϵ described in Section 3.2.3, compared with the experimental values [69]. As can be seen in Fig. 3.10, the RNG k-ϵ model overpredicts the centreline mixture fraction values close to the nozzle between 0 and 100 mm, whereas the $k-\epsilon$ model underpredicts the centreline mixture fraction at the same locations. Farther downstream from 200 to 300 mm, best agreement with the experimental data is obtained using the corrected $k-\epsilon$ model, whereas the RNG k-ϵ model is in better agreement with the experimental data at the 350 and 425 mm locations.

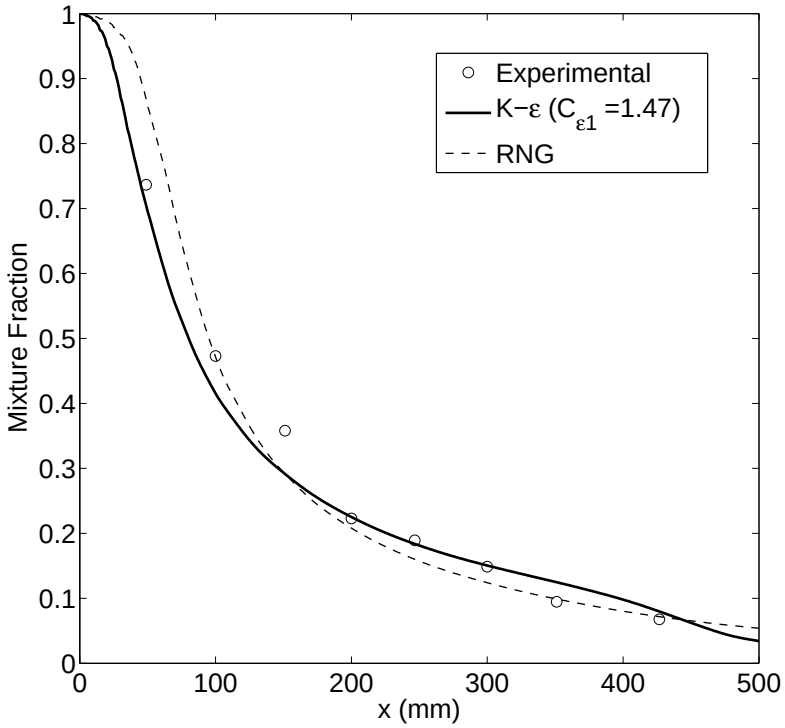

Figure 3.10: Centreline mixture fraction profiles for different turbulence models compared with experimental data [69]

Further information can be retrieved from the radial profiles. Figure 3.11 shows the radial mixture fraction profiles for several axial locations using the same turbulence models compared with the experimental data.

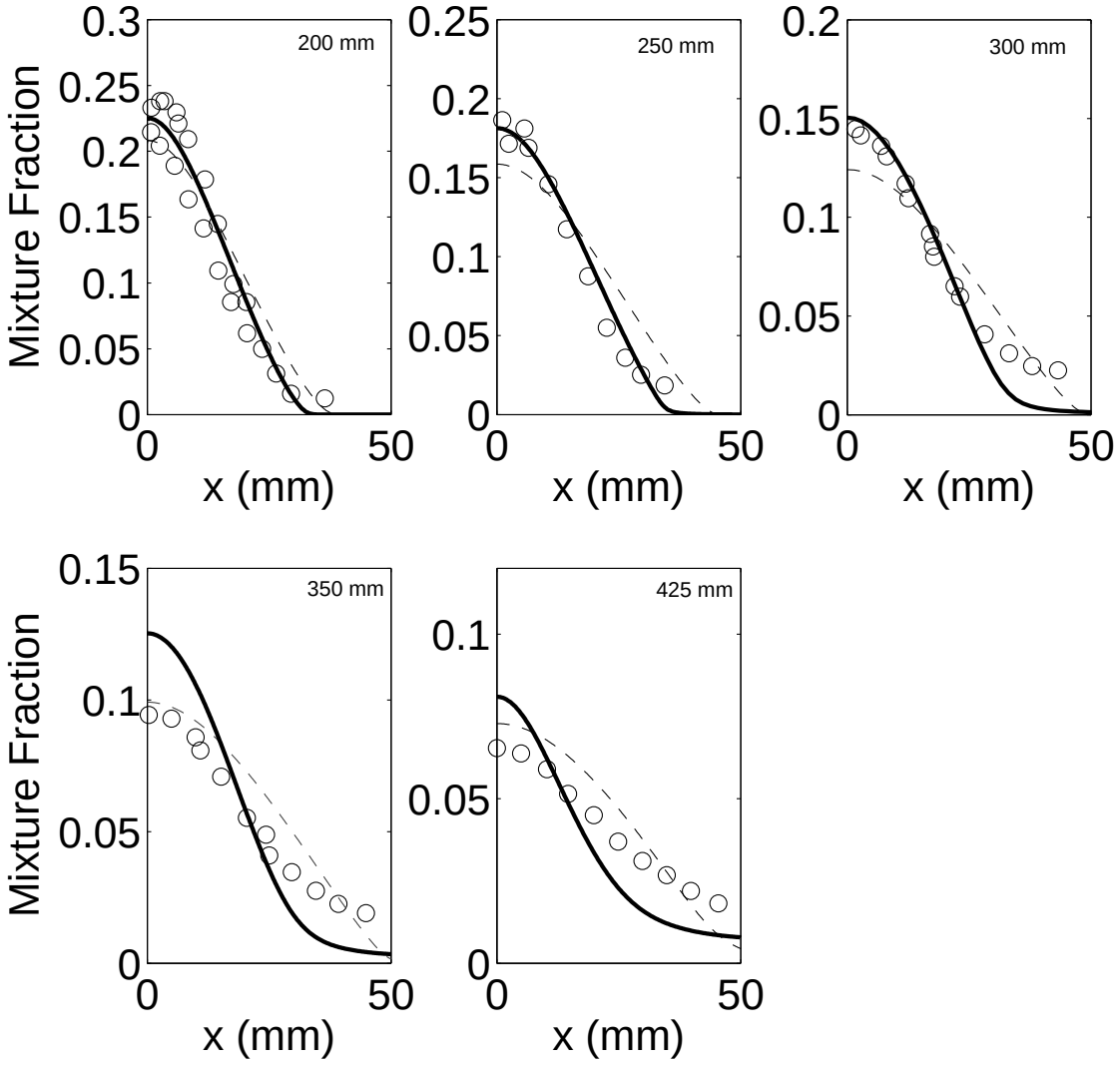

Figure 3.11: Radial mixture fraction profiles at different axial positions for different turbulence models compared with experimental data [69], same symbols as in Fig. 3.10

Similar to what is observed in Fig. 3.10, the radial profiles predicted by the corrected $k-\epsilon$ model match the experimental mixture fraction profiles closely near the nozzle. For axial positions less or equal to 300 mm, both the RNG and corrected $k-\epsilon$ models predict the

mixture fraction profile well, with a slight advantage for the corrected $k-\epsilon$ model as the RNG k-ϵ model underpredicts the mixture fraction by approximately 10-15% at 250 mm and 300 mm. Farther from the nozzle at 350 mm, the RNG k-ϵ model gives values very close to the experimental data close to the centreline and overpredicts the mixture fraction past 15 mm in the radial direction. In contrast, for the same position, the centreline mixture fraction from the corrected $k-\epsilon$ model is approximately 30% higher than that in the experiments, but remains in good agreement with the experimental data away from the centreline. At 425 mm the RNG k-ϵ model predicts the centreline mixture fraction well but overpredicts the mixture fraction away from the centreline. At this location, the overprediction is on the order of 30 % for the corrected $k-\epsilon$ model on the centreline. However, away from the centreline, the predicted values become lower than the experimental data. In conclusion, both turbulence models reasonably predict the turbulent mixing field compared to the experimental values. The corrected $k-\epsilon$ model appears to perform better in the first half of the flame, whereas RNG $k-\epsilon$ model is shown to produce better agreement for mixture fractions in the downstream regions of the jet flame. It is decided to select the corrected $k-\epsilon$ model in the remaining comparisons for the temperature mainly for consistency with previous numerical simulations [16, 17, 35, 70] using different turbulent combustion models applied to the same flame.

3.3.4 Conditional averages

Profiles for the conditional CO_2 mass fraction are considered at four different axial locations and are presented in Fig. 3.12. As seen in Fig. 3.12, the magnitude of the conditional profiles increases with increasing axial distance from the nozzle, between 50 mm and 275 mm. This is expected since there is little CO_2 very close to the nozzle, resulting in lower conditional profiles for this location. Farther downstream a greater portion of the jet is burning which produces higher levels of CO_2. Further, the shape of the conditional profiles can be seen to change significantly between 50 mm and 125 mm, a more pronounced peak is observed at larger axial positions. No experimental data is available for the conditional averages. However, the present results are qualitatively in agreement with previous CMC jet flame simulations [71, 90].

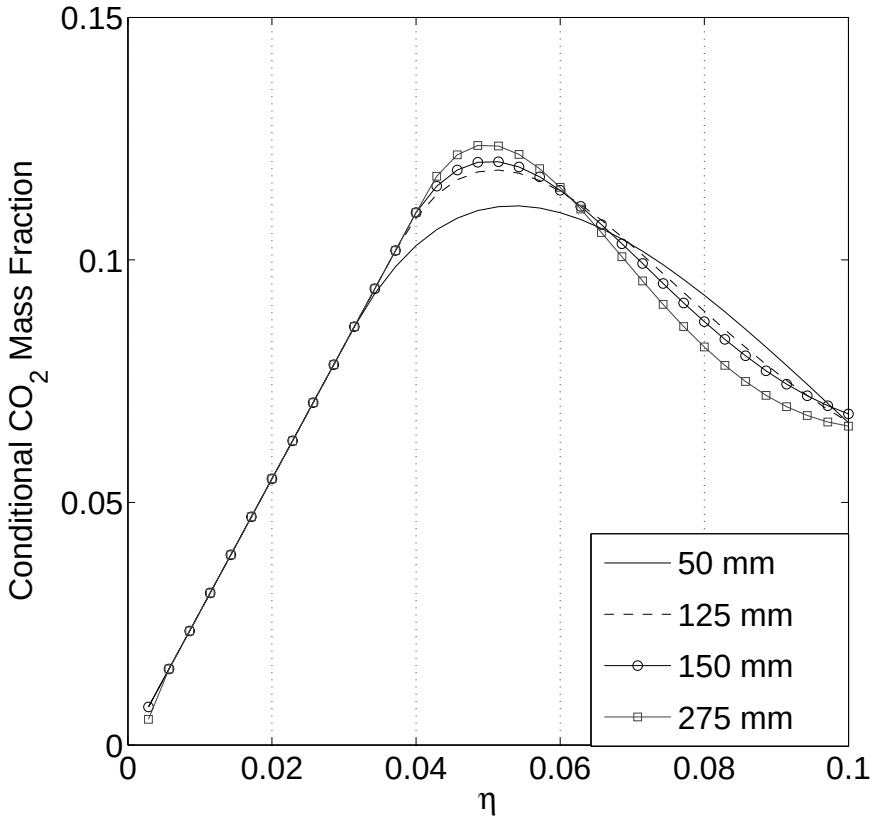

Figure 3.12: Conditional CO_2 mass fraction profiles at different axial positions

3.3.5 Temperature field

In this section, the CSE temperature predictions are first compared with the experimental data [69] and then with previous numerical simulation results [16, 17]. The centreline temperature profiles are shown in Fig. 3.13. The current predictions are in very good agreement with the experimental values qualitatively and quantitatively. A small underprediction can be seen very close to the nozzle and farther downstream a slight overprediction is displayed near the tip of the flame (defined as the centreline location where the peak temperature is reached), i.e. at 425 mm. For example, the peak temperature is slightly overpredicted by approximately 200K, on the order of 12%.

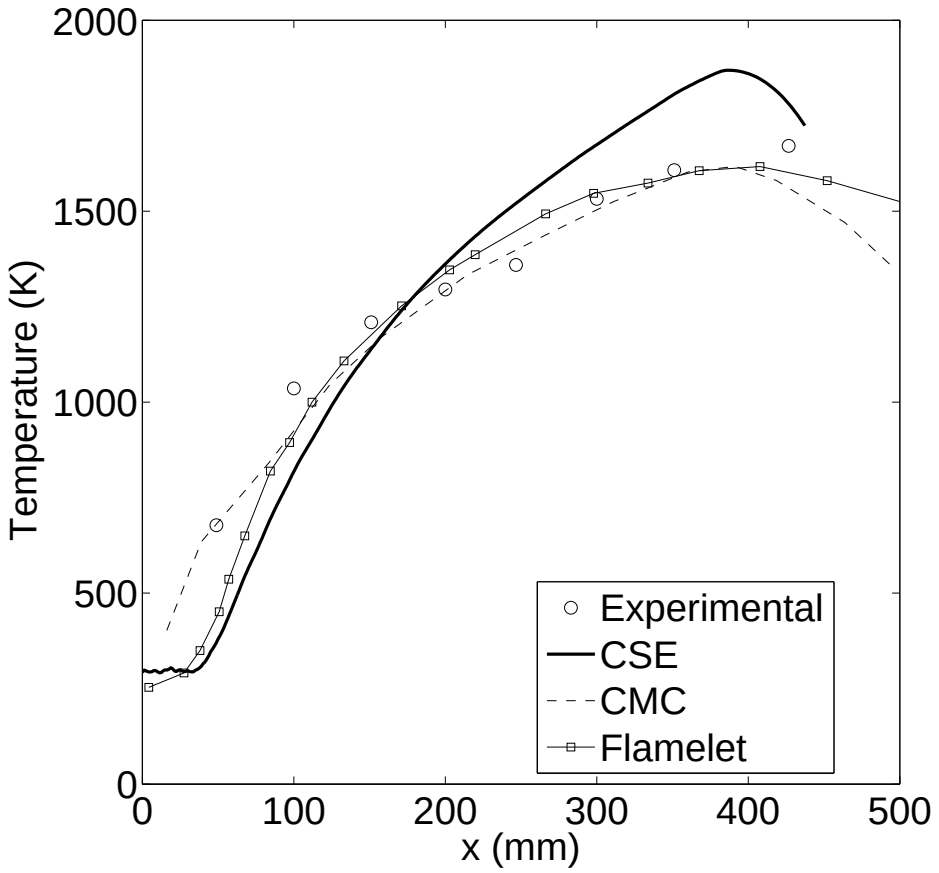

Figure 3.13: Centreline temperature profiles for CSE, CMC [16] and flamelet [17] compared with experimental data [69]

Similar agreement between the CSE and experimental temperatures can be seen for the radial profiles shown in Fig. 3.14. The width of the flame is captured very well for axial positions of 150 mm and 250 mm. At 200 mm the CSE results show a slightly narrower flame than what is seen in the experimental results. Farther downstream the CSE temperature predictions follow the same trends as the experimental results with the peak temperature being slightly overpredicted by approximately 13% at the axial locations of 300 mm and 350 mm. At 425 mm the CSE predicted flame remains narrower compared to the experimental profile and and the temperature is underpredicted for radial locations between 15 to 50 mm.

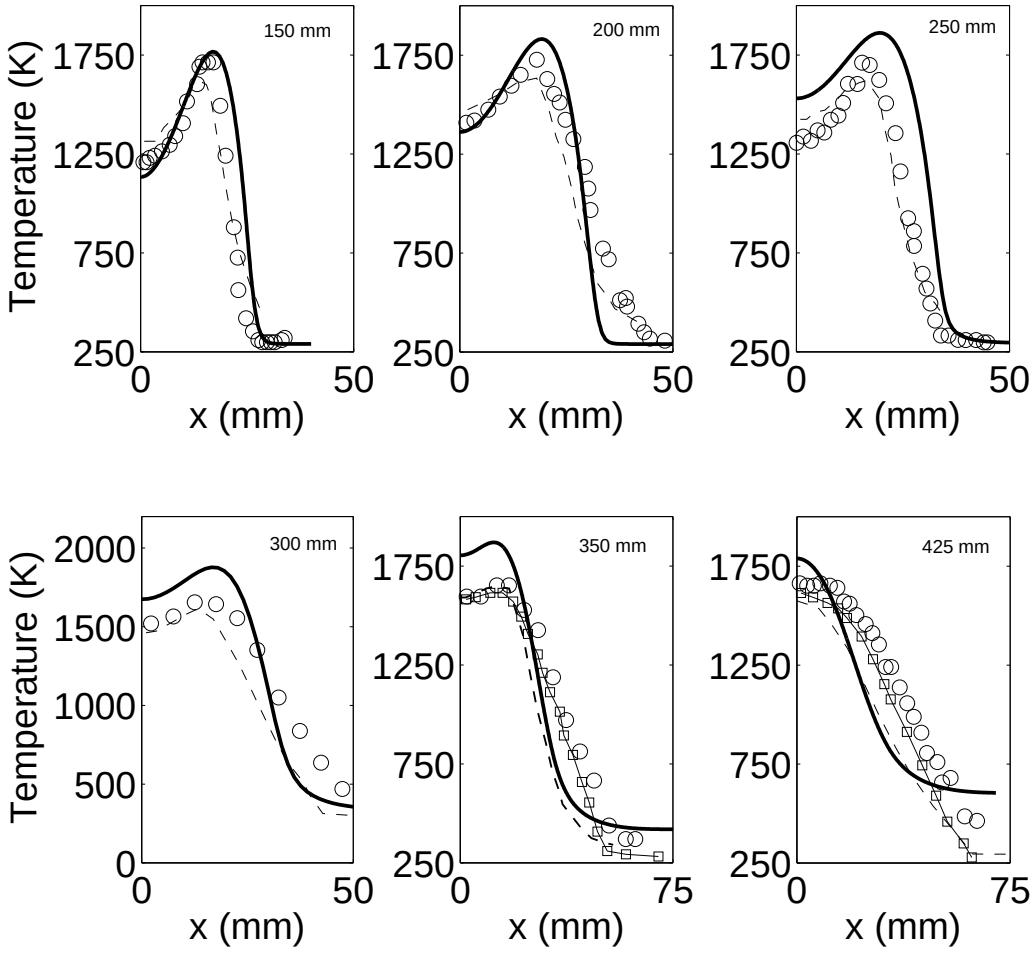

Figure 3.14: Radial temperature profiles at different axial positions for CSE, CMC [16, 35] and flamelet [17] compared with experimental data [69], same symbols as in Fig. 3.13

For comparison, previously published results using the flamelet model [17] and CMC [16, 35] are included. The simulations performed by Kassem et al. [70] focus on implementing the Eddy dissipation model in OpenFOAM. However, in their work, radiation effects are not taken into account. As a result, the predicted temperatures are noticeably higher than those reported experimentally and the numerical results are not as good as those shown in [16, 17, 35]. Thus, the predictions presented in [70] are not included in Figs. 3.13 and 3.14. Outside the turbulent combustion model, the major difference between the current

CSE work and previous simulations [16, 17, 35] is related to soot modelling. The studies presented in [16, 17, 35] include the same optically thin radiation model as that used in the present work, but soot formation is considered. Similar to the current investigation, the GRI mechanism is also included in the simulations reported in [16, 35] for methane combustion. Detailed kinetics are used by Brookes and Moss [17], however no specific reference is given for the chemistry. In Fig. 3.14, it should be noted that the results from Brookes and Moss [17] are only available for the axial positions in the downstream region of the flame, 350 and 425 mm. The CSE predictions are comparable to those obtained in previous calculations. As expected, the present CSE tends to predict peak temperatures slightly larger and narrower radial profiles compared to those shown in [16, 17, 35]. This is likely due to the fact that soot is neglected in the present CSE formulation. Brookes and Moss state that the selected flame is a mildly nonadiabatic flame, with a radiative heat loss of less than 20% [69]. To determine the radiative heat loss in the present CSE simulations a comparison with an adiabatic simulation of the flame is conducted. From this comparison it is seen that the peak centreline temperature is approximately 15% higher in the adiabatic case. This suggests that the radiative heat loss due to soot (in the present case estimated to be on the order of 5%) is less significant than the radiative heat loss due to gas radiation from the CO_2 and H_2O.

3.4 Summary

CSE combined with TGLDM for the chemistry tabulation was implemented in order to simulate a confined non-premixed turbulent methane flame. A sensitivity analysis related to the number of CSE ensembles and ensemble size was performed. The number of CSE ensembles was shown to have a significant impact on the results if not selected appropriately. For a given simulation case, it may be difficult to know the suitable number of CSE ensembles required in advance. Thus, a sensitivity analysis is recommended to be completed for each new CSE application. The number of points in each ensemble was also shown to have an impact on the predictions. For the present simulation, the ensemble size was defined based on a mean mixture fraction range, $0.015 < \tilde{Z} < 1$, yielding Favre-averaged temperature predictions equivalent to those using, $0 < \tilde{Z} < 1$ but, requiring less computational resources.

As part of the inversion process, regularization is needed in CSE. The Tikhonov method was implemented [78]. The regularization was implemented following the procedure used in previous CSE studies [39, 42]. The present CSE calculations provided stable and converged predictions. Recent CSE studies [45, 46] present a different expression to calculate

the regularization parameter. Further investigation would be useful in determining the best expression for the regularization parameter. Future work may also be include testing different regularization techniques and finding the most appropriate regularization method depending on accuracy, numerical stability and computational cost, for a given combustion problem.

Two different turbulence models were used, the $k-\epsilon$ model with a corrected value for $C_{\epsilon 1}$ and the RNG $k-\epsilon$ model. The corrected $k-\epsilon$ model predicted mixture fractions accurately for axial locations in the first half of the flame. Farther downstream, the RNG $k-\epsilon$ model performed better. Overall, the current predictions for the mixture fraction are in good agreement with the experimental data.

The predicted temperatures using CSE and the $k-\epsilon$ turbulence model with a modified value of $C_{\epsilon 1} = 1.47$ were shown to be in very good agreement with the experimental data. CSE tended to slightly overpredict the peak temperature which is likely to be due to the lack of a soot model that includes radiation from soot. Further, the current CSE results were of comparable quality with previous simulations using the flamelet model [17] and CMC [16, 35].

Chapter 4

Inverse analysis and regularization in CSE

Inverse problems involve finding a solution which violates one of Hadamard's three criteria for a well-posed problem: a solution exists, is unique, and is not sensitive to small changes in the initial conditions [91]. Inverse problems can be categorized as rank deficient inverse problems, where a unique solution does not exist and discrete ill-posed problems, where the solution is sensitive to small perturbations [77, 91]. For both of these categories, additional information based on some prior expectation of the solution attributes must be introduced through regularization to obtain a solution.

The inverse problem found in CSE is discrete ill-posed and is sensitive to small perturbations in the data. Thus, a regularization method is needed to stabilize the solution. Although some aspects of the inversion process have been studied, such as the size of the ensembles and mixture fraction range used for the inversion process additional analysis is required. In the present study, the turbulent flow and mixing fields obtained from the RANS-CSE calculations of a turbulent non-premixed methane jet flame presented in Chapter 3 are extracted to serve as a baseline for the inverse problem. The current regularization method, zero-order temporal Tikhonov, used in most CSE studies has been shown to work well in previous simulations. However, a detailed uncertainty analysis has never been completed.

The first objective of this chapter is to determine the ill-posedness of the CSE inverse problem to assess how sensitive the solution is to small perturbations in the data. Next, the origin of these perturbations is investigated. This information is used to determine credibility intervals so that the uncertainty in the recovered solution can be estimated. Bayesian analysis has previously been used to investigate syngas chemistry models to determine un-

certainty [92], but has never been applied to CSE. The study of the CSE inversion problem in the Bayesian framework will allow a systematic method for studying this problem in a probabilistic manner and obtain statistical information on the inversion problem. Among the statistical information collected are credibility intervals with and without a smoothing prior, which shows the impact of including a prior on the level of uncertainty in the solution. Once the credibility intervals are calculated, several regularization methods are tested using the Bayesian framework to determine the regularization method best suited to the current problem. Thus, the current study is focused on the amount of uncertainty introduced into the conditional averages due to different regularization methods.

4.1 Combustion problem

The combustion problem corresponds to the asymmetric jet flame experimentally studied by Brookes and Moss [69]. The atmospheric non-premixed methane flame is selected due to the small amount of soot production. In the RANS-CSE simulations performed in Chapter 3, soot modelling was excluded and radiation from CO_2 and H_2O was modelled using an optically thin radiation model. In Chapter 3, the ensembles were defined such that they had an equal size in the axial direction and extended from the centreline to the furthest radial location. To reduce the computational requirements, only one of these ensembles is considered in the present study. The methodology and conclusion would be similar for other ensembles. Figure 4.1 shows some mean mixture fraction contours along with the location and shape of the CSE ensemble selected for the present study. For methane-air combustion the stoichiometric mixture fraction value is equal to 0.055. The computational spatial grid consisted of 58,800 cells in two dimensions. As a result, each CSE ensemble has approximately 2500 CFD cells. However, only cells that include a mean mixture fraction greater than 0.015 are kept for the inverse problem, while those containing very lean mixtures outside the flammability range are excluded. The sensitivity analysis performed on the mixture fraction range included for the inversion process in Chapter 3 showed that using additional cells with a mean mixture fraction less than 0.015 had a negligible impact on the results, but significantly increased the computational cost. As a result, for the inversion process only 798 cells of the 2500 CFD cells are used.

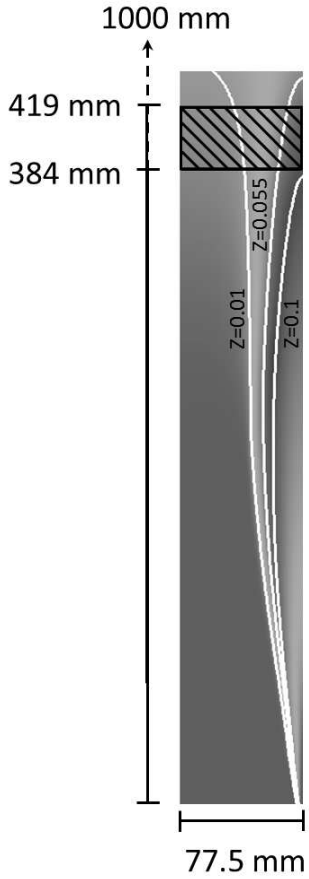

Figure 4.1: Mean mixture fraction contours and location of CSE ensemble (shaded area)

The conditional mass fraction of H_2O and CO_2 are obtained by deconvolving a Fredholm integral equation given by

$$\widetilde{Y}_k(x_j,t) = \int_0^1 \langle Y_k|\eta\rangle(\eta,t)\overline{P}(\eta,x_j,t)d\eta, \tag{4.1}$$

where $\langle Y_k|\eta\rangle$ is the conditional mass fraction for species k, $\widetilde{Y}_k$ is the unconditional mass fraction and $\tilde{P}(\eta)$ is the Favre-averaged PDF of mixture fraction. These conditional mass fractions are then used to obtain the conditional reaction rates from chemistry tables. Further detail on how these tables are generated can be found in Chapter 3. The mean

reaction rates are then calculated using

$$\overline{\dot{\omega}_k}(x_j,t) = \int_0^1 \langle \dot{\omega}_k|\eta\rangle(\eta,x_j,t)\tilde{P}(\eta,x_j,t)d\eta, \tag{4.2}$$

where $\langle \dot{\omega}_k|\eta\rangle$ is the conditional chemical source term of species k. The mean reaction rates are then returned to the CFD code to solve the averaged transport equations of species. Thus, it is extremely important to ensure that the conditional mass fractions of H_2O and CO_2 obtained from the inverse problem are accurate. This implies that they must contain several key attributes. The conditional mass fractions cannot be negative and cannot be larger than unity due to conservation of mass. In addition, it is expected that the conditional mass fraction profiles should be spatially smooth in mixture fraction space as diffusion promotes this behavior. Finally, for methane-air combustion the location of the peak in mixture fraction space is typically between 0.05 and 0.1 depending on the chemical mechanism used [23, 93]. All of this information can be included as prior information to reduce the ill-posedness of the inverse problem. In the remaining sections, tests and illustrations for the inverse problem will consider only the conditional mass fractions of CO_2.

4.2 Computational details for the inverse problem

In order to study and isolate the effect of regularization on the CSE solution to the combustion case presented in Chapter 3, the inverse problem is decoupled from the CFD calculations to eliminate transient effects. This means that the A matrix (integrated PDF over a mixture fraction interval) and $\vec{b}$ vector (unconditional mass fraction) in Eq. 4.3 remain constant,

$$A \cdot \vec{\alpha} = \vec{b}, \tag{4.3}$$

where $\vec{\alpha}$ is the conditional mass fraction, $\langle Y_k|\eta\rangle$. This is accomplished by obtaining the unconditional mass fractions of CO_2, mean mixture fraction and mean mixture fraction variance for one ensemble from the converged combustion simulation consisting of 798 cells completed in Chapter 3. The mixture fraction (η) space is divided into $N = 200$ equally spaced bins. Based on the simulations completed in Chapter 3 this results in 200 unknowns ($\langle Y_{CO_2}|\eta\rangle$), obtained from Eq. 4.1 and 798 equations. The β-PDF is calculated using the mean mixture fraction and variance extracted from the previously converged turbulent flame calculations completed in Chapter 3. The A matrix is constructed following Eq. 4.4.

$$A_{jm} = \int_{\eta_1}^{\eta_2} \widetilde{P}(\eta_m, x_j, t)\ d\eta, \tag{4.4}$$

where j is the spatial coordinate index and η_1 and η_2 are the lower and upper bounds of the mixture fraction bin, respectively.

One method for determining the ill-posedness of the problem is to perform Singular Value Decomposition (SVD) on the A matrix to obtain the singular values. For SVD the A matrix is decomposed such that

$$A = U\Sigma V^T, \tag{4.5}$$

where U is a column-orthogonal matrix, Σ are the singular values and V is another orthogonal matrix [80]. The singular values, σ_j, which are indicative of the ill-posedness of the problem, are shown in Fig. 4.2.

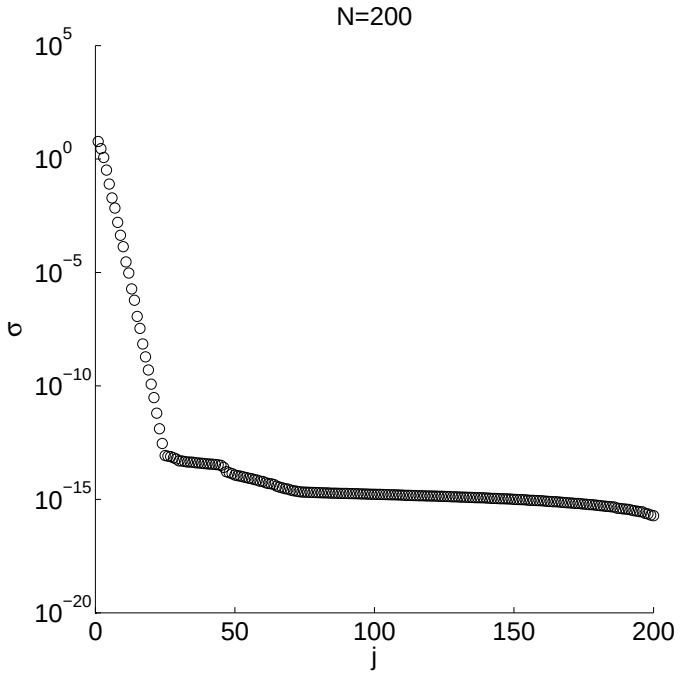

Figure 4.2: Singular values for A matrix for 200 mixture fraction points

The singular values vary by over 15 orders of magnitude, leveling off at at 10^{-15} for $j > 60$

which is typical for an ill-conditioned A matrix generated from a Fredholm integral equation of the first kind. The condition number of matrix A can be related to the singular values by the following equation

$$\text{Cond(A)} = \frac{\sigma_{max}}{\sigma_{min}}, \tag{4.6}$$

where σ_{max} and σ_{min} are the largest and smallest singular value, respectively. Further, there is a sharp drop in the magnitude of the singular values initially, showing that the low frequency components of the solution can be reconstructed from the first few Fourier coefficients.

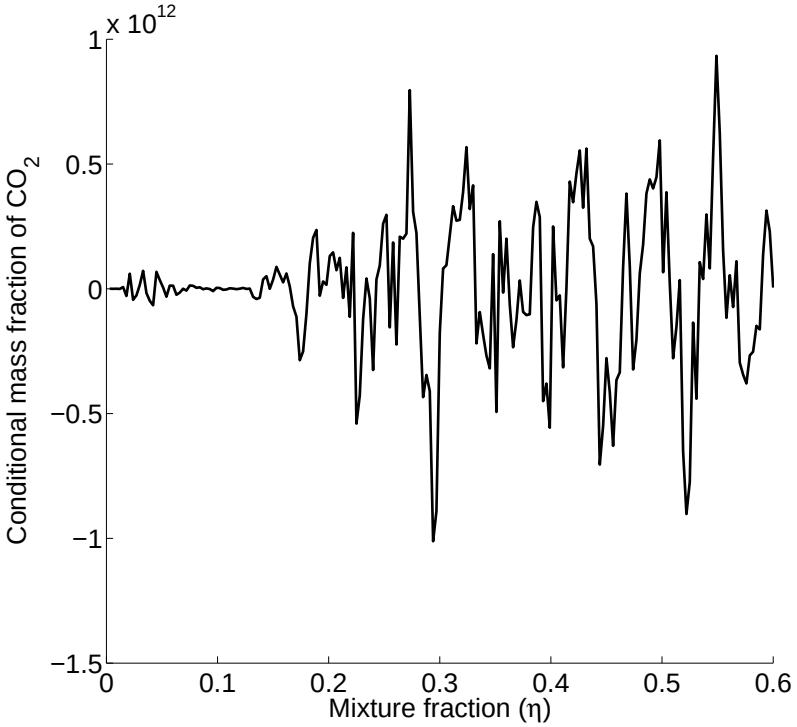

Figure 4.3: SVD solution to Eq. 4.3, with N=200

In an attempt to provide a baseline profile which can be compared to a regularized solution, a SVD solution to Eq. 4.3 is calculated for the 200 mixture fraction point grid and is shown in Fig. 4.3. It can be seen that without any regularization, the SVD solution is nonphysical due to the amplification of discretization error by small singular values. The

relative error in the solution vector $\vec{\alpha}$, $\delta\vec{\alpha}$, can also be related to the condition number of matrix A and the error in $\vec{b}$, $\delta\vec{b}$, by

$$\frac{||\delta\vec{\alpha}||}{||\vec{\alpha}||} \leq \text{Cond(A)} \frac{||\delta\vec{b}||}{||\vec{b}||}. \tag{4.7}$$

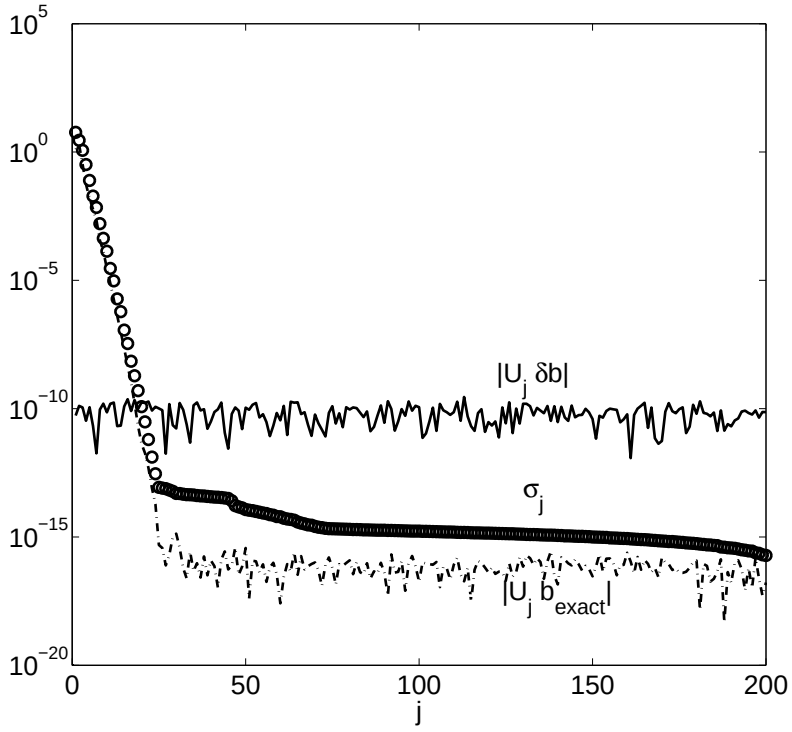

Figure 4.4: Perturbation analysis of Fourier coefficients, error term and singular values (same notation as in Eq. 4.8)

For further demonstration of the error amplification, a new $\vec{b}$, referred to as $\vec{b}_{exact}$, is calculated by multiplying the same A matrix with a presumed profile for the conditional CO_2 mass fractions, $\vec{x}$, as shown in Eq. 4.3. For the sole purpose of illustration, any presumed shape for $\vec{x}$ may be considered; in the current study, experimental values in a laminar flame are selected [23]. A small perturbation is applied to $\vec{b}_{exact}$ using a normally distributed noise with zero mean and standard deviation of 10^{-10} in order to determine the sensitivity of the solution of Eq. 4.3 to small perturbations. A standard deviation of 10^{-10}

is selected to demonstrate the ill-possedness of the CSE problem under investigation. 10^{-10} represents a level of noise that is greater than the accuracy of double precision calculations but, much smaller than the expected modelling error discussed in Section 4.3.4, on the order of 10^{-3}. For perturbations larger than 10^{-10}, the solution becomes unrecoverable without prior information. With SVD $\vec{x}$ may be written as the sum of two components, the exact solution and the error following

$$\vec{x} = \vec{x}_{exact} + \delta\vec{x} = \underbrace{\sum_{j=1}^{n} \frac{U_j \cdot \vec{b}_{exact}}{\sigma_j} V_j}_{\text{exact solution}} + \underbrace{\sum_{j=1}^{n} \frac{U_j \cdot \delta\vec{b}}{\sigma_j} V_j}_{\text{error}} . \tag{4.8}$$

Eq. 4.8 can only be used for illustration as in practice $\vec{b}_{exact}$ cannot be distinguished from $\delta\vec{b}$. Figure 4.4 presents the Fourier coefficients $U_j \cdot \vec{b}_{exact}$, and the error term $U_j \cdot \delta\vec{b}$, compared to the singular values previously shown in Fig. 4.3. It can be seen that without any perturbations the Fourier coefficients satisfy the discrete Picard condition, which states the Fourier coefficients must decay to zero faster than the singular values in order to recover a meaningful solution [94]. However, when $\vec{b}_{exact}$ is perturbed the error term is larger than the singular values for $j \leq 20$. Thus, the Discrete Picard condition is no longer satisfied and the amplified error will dominate the exact solution. Consequently, Eq. 4.3 is ill-posed and a regularization method is required to recover a solution.

4.2.1 TSVD

One way to regularize the problem is to simply exclude the summation terms in Eq. 4.8 that correspond to small singular values; this is called Truncated Singular Value Decomposition (TSVD), and is based on the fact that the Fourier coefficients that correspond to the smallest singular values reconstruct the high frequency solution components, and may not have much physical significance. Thus, TSVD effectively filters out high frequency noise from the solution by truncating the smallest singular values. The result is a significant reduction in the noise amplification in the solution while preserving its physicality. The following equation is used to recover a solution using TSVD [79],

$$\vec{x} = \sum_{j=1}^{n-p} \frac{U_j \cdot \vec{b}}{\sigma_j} V_j, \tag{4.9}$$

where n is the number of singular values, $\vec{b}$ is the unconditional mass fraction, U_j and V_j are the column vectors obtained from SVD as shown in Eq. 4.5, σ_j is the j^{th} singular

value and p is the number of singular values that are truncated. The Fourier coefficients can be used to estimate the number of singular values to be truncated. According to Fig. 4.4 approximately 180 singular values should be truncated to satisfy the discrete Picard condition. Figure 4.5 shows the recovered solution and error using TSVD with 184 singular values truncated. It is found that this degree of truncation produces a recovered solution in best agreement with the exact solution, with an error of less than 10^{-3}. However, to recover this solution, with perturbations of 10^{-10}, 92% of the singular values have to be truncated. With larger perturbations, the accuracy of the TSVD solution will further decrease as the truncation of additional singular values is required to suppress noise amplification. As a result, the remaining analysis focuses on zero-order and first order Tikhonov regularization [78].

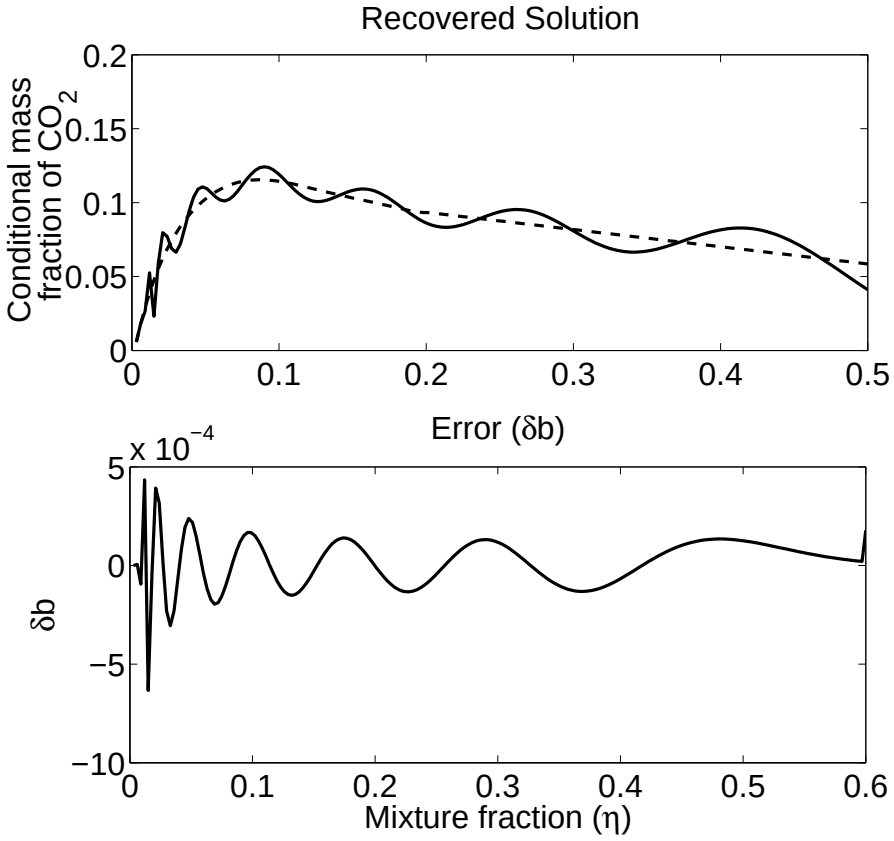

Figure 4.5: TSVD solution and error for perturbed $\vec{b}$ with 184 singular values truncated compared to exact solution (dashed line)

4.2.2 Origin of perturbations

The origin of the perturbations that occur in $\vec{b}$ needs to be identified so that they can be reduced in the simulations and modelled for the Bayesian analysis. As a first step, it is important to visualize the perturbations (δb) in the data, which can be estimated as the differences between $\vec{b}$ obtained from the CFD-CSE simulations from Chapter 3 and $\vec{b}$ calculated using the least squares solution to Eq. 4.3.

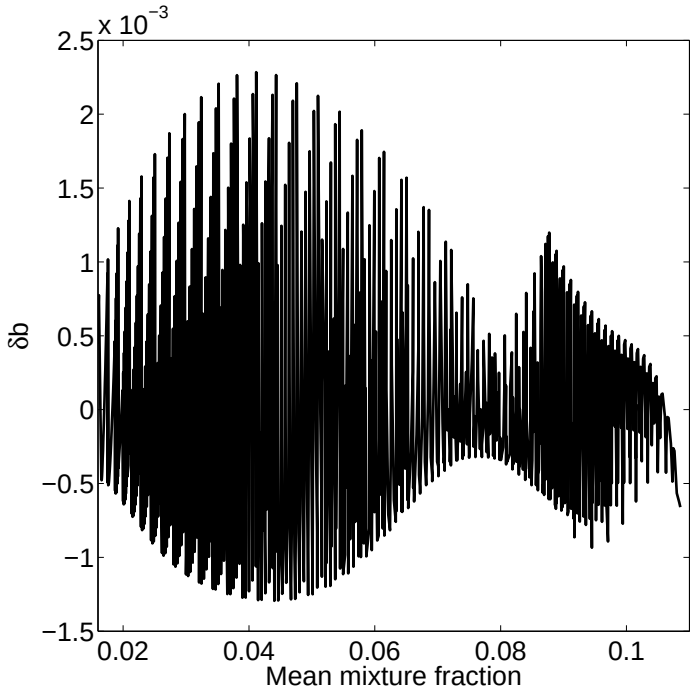

Figure 4.6: Perturbations in $\vec{b}_{exact}$ from the CSE simulations

Figure 4.6 shows the calculated perturbations as a function of the mean mixture fraction taken at each cell in the ensemble. Figure 4.6 reveals several important characteristics of the noise spectrum. First, the magnitude of the perturbations is not constant and highest at mean mixture fractions between 0.03 and 0.05. Second, for mean mixture fractions less than 0.04, the perturbations in the data do not appear to be random suggesting that there may be a correlated error. One possible explanation for this is that the current analysis does not take into account the variance of the mean mixture fraction. The perturbations

vary in physical space, but can be more easily expressed as functions of the mean mixture fraction and its variance in the Bayesian analysis. In the current problem, each cell in the ensemble has a unique mean mixture fraction and variance. As a result, there are not enough data points to represent the perturbations in both dimensions. For simplicity, the perturbations are only modelled as a function of the mean mixture fraction.

Another possible source of perturbations is related to the determination of the unconditional mass fractions in CSE. In the CSE simulations, the calculated conditional mass fractions are used to retrieve the conditional chemical source terms from the chemistry tables. Then, the unconditional chemical source terms are found by integrating the conditional chemical source terms with the PDF in mixture fraction space, as shown in Eq. 4.2. The mean species reaction rates are returned to the CFD code to solve the unconditional species concentrations. As a result, any error introduced in the calculation of the conditional averages propagates in the unconditional mass fractions. This would explain why some perturbations are seen in the unconditional mass fraction profile shown in Fig. 4.6. The PDF and the related A matrix are both crucial to the inverse problem to determine the conditional averages. As shown in Eq. 4.7, the A matrix is calculated at every point in the CSE ensemble in mixture fraction space resulting in 798 profiles for each of the 200 η values. Figure 4.7 displays the range of A_{jm} values for the entire ensemble for $\eta \leq 0.026$. It can be seen that the largest range occurs at the first η point equal to 0.003 and the range of A_{jm} values decreases with increasing η reaching approximately zero for η equal to 0.5, not shown in Fig. 4.7. This implies there exist large fluctuations in the PDF for this first η value. This phenomenon is caused by using a discrete mixture fraction grid. The kernel (A matrix) fluctuations may be attenuated if a finer mixture fraction mesh is included. However, an error will always be present due to the lack of information between $\eta = 0$ and the first grid point in η space. This may also occur for the last η value and unity. No peak is observed for rich mixtures for the present CSE ensemble due to its location in the flame, farther away from the fuel nozzle exit. Consequently, for a finite uniform mixture grid a more pronounced correlated error is expected for lean mixtures, as shown in Fig. 4.6.

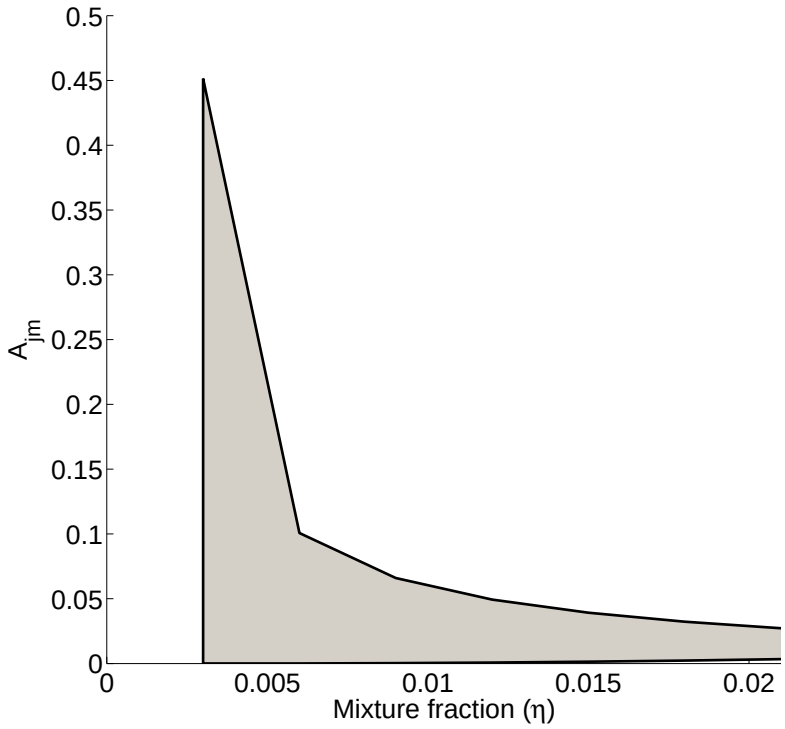

Figure 4.7: Range of A_{jm} for CSE domain cells

4.3 Bayesian analysis

4.3.1 Principle

Using a mixture fraction grid of 200 nodes, the system of equations represented by Eq. 4.3 contains 200 unknowns, the conditional species mass fractions. Each of these unknowns is equivalent to a solution parameter that may be changed to better match the unconditional mass fraction of CO_2. Bayesian analysis can be used to determine the uncertainty in each of these solution parameters by estimating the probability that a given value of a solution parameter satisfies Eq. 4.3 [80]. This is more formally done by computing the credible intervals on the unknown parameters, where a wider credible interval represents more uncertainty in the inferred solution and also less influence in inferring a solution. For example, if the credible intervals extend to infinity, no preferred solution exists and that parameter has no influence on the inferred solution. It should be stressed that Bayesian analysis is not, by itself, a regularization method. In Bayesian analysis, diverse sources of

information, such as measurements and prior knowledge, can be incorporated into a single estimate. In contrast, regularization is performed by promoting presumed aspects of the solution through priors in Bayesian analysis, as will be shown in Section 4.3.2.

In the current investigation, the objective is to find the solution that maximizes the conditional posterior probability, $P(\vec{x}|\vec{b})$, defined via Bayes's rule [95] as

$$P(\vec{x}|\vec{b}) = \frac{P(\vec{b}|\vec{x}) \cdot P_{pr}(\vec{x})}{P(\vec{b})}, \tag{4.10}$$

where $P(\vec{b}|\vec{x})$ is the likelihood of the observed data occurring for a given hypothetical $\vec{x}$, $P_{pr}(\vec{x})$ modifies the modelled probability based on prior knowledge and $P(\vec{b})$ is the marginal probability of the data, also known as the evidence. For a linear system as shown in Eq. 4.3, a linear model may be applied to determine the likelihood,

$$P(\vec{b}|\vec{x}) \propto exp\left(-\frac{1}{2}\left(\vec{b} - A\vec{x}\right)^T \Gamma_{noise}^{-1}\left(\vec{b} - A\vec{x}\right)\right), \tag{4.11}$$

where Γ_{noise} is the covariance matrix that is assumed to be invertible and is modelled in Section 4.3.4. The marginal probability, $P(\vec{b})$, can be calculated using

$$P(\vec{b}) = \int_{-\infty}^{\infty}\int_{-\infty}^{\infty}\cdots\int_{-\infty}^{\infty} P(\vec{b}|\vec{x})P_{Pr}(\vec{x})dx_1dx_2\cdots dx_m, \tag{4.12}$$

and scales the posterior probability so that it satisfies the Law of Total Probability [96]. However, calculating the marginal probability, $P(\vec{b})$, using Eq. 4.12 can be computationally expensive if m is large or the product $P(\vec{b}|\vec{x})P_{pr}(\vec{x})$ is expensive to solve.

Instead, in order to avoid the direct calculation of $P(\vec{b})$ using Eq. 4.12, Markov-Chain Monte Carlo (MCMC) is considered. The principle of MCMC is to generate a sequence of trial points, x that are ergodic to the posterior probability, and can be used to approximate the posterior probability as a normalized histogram [80, 95]. In MCMC, $P(\vec{b}|\vec{x})$ and P_{pr} are input parameters, $P(\vec{b}|\vec{x})$ is defined using Eq. 4.11 and different expressions for P_{pr} are selected, as shown in Section 4.3.2. Tikhonov regularization will be included in P_{pr} through Eq. 4.15 or Eq. 4.18. The output from the MCMC algorithm is $P(\vec{x}|\vec{b})$.

In a Markov-Chain, the next candidate solution, $\vec{x}_{k+1}$, depends only on $\vec{x}_k$ and is determined at each $\vec{x}_k$ by sampling a trial distribution $q\left(\vec{x}_{k+1}|\vec{x}_k\right)$. In MCMC, a random number between 0 and 1, R_{0-1}, is selected to determine if the candidate solution is accepted. If $R_{0-1} \leq \alpha\left(\vec{x}_k, \vec{x}_{k+1}\right)$ the candidate is accepted, otherwise the candidate is rejected and

a new candidate solution is selected. The acceptance criterion, $\alpha\left(\vec{x}_k, \vec{x}_{k+1}\right)$, is determined by

$$\alpha\left(\vec{x}_k, \vec{x}_{k+1}\right) = min\left(1, \frac{\pi\left(\vec{x^c}_{k+1}\right) \cdot q\left(\vec{x}_k | \vec{x^c}_{k+1}\right)}{\pi\left(\vec{x}_k\right) \cdot q\left(\vec{x^c}_{k+1} | \vec{x}_k\right)}\right), \tag{4.13}$$

where $\vec{x^c}$, is the candidate solution and $\pi(\vec{x}) = P(\vec{b}|\vec{x}) \cdot P_{Pr}(\vec{x})$. Further detail on MCMC methods may be found in [95]. The posterior probability is obtained using the slice sampling MCMC algorithm in Matlab [97]. For the current MCMC simulations, 10 000 samples are included and the MCMC calculation is initialized at the least squares solution of Eq. 4.3 to minimize the burn in period, which involves throwing away iterations at the start of MCMC simulation. Larger samples were also tested but the estimate trends were found to be similar, leading to the same analysis and conclusions as those shown.

4.3.2 Prior models

The ill-conditioning of the A matrix leads to an indefinite topography of the likelihood function. Thus, additional information is required to obtain a solution with a definable topography. One method to accomplish this is to include the regularization methods and *a priori* information as priors. In the present work, two prior distributions are considered. The first prior is created to disallow negative conditional averages and is defined as

$$P_{Pr}(\vec{x}) = \begin{cases} 0 & \text{if } \vec{x} < 0 \\ 1 & \text{if } \vec{x} \geq 0 \end{cases}, \tag{4.14}$$

which is similar to the truncation of negative values presented in Chapter 3. However, Eq. 4.14 represents a significant improvement as it incorporates the prior information directly into the problem and post processing nullification and rescaling does not maximize the posterior probability in Eq. 4.10. As a result, no post processing rescaling is required for the regularization methods in the Bayesian framework.

The second prior distribution used depends on the type of regularization applied. For temporal smoothing, which corresponds to the method outlined in Chapter 3, the prior distribution is defined as

$$P_{Pr}(\vec{x}) = exp(-\alpha_1(\vec{x} - \vec{x_t})^T(\vec{x} - \vec{x_t})), \tag{4.15}$$

where α_1 is a regularization parameter and x_t is the solution to the previous time step. This prior corresponds to zero-order Tikhonov regularization [98].

For spatial smoothing, which corresponds to first order Tikhonov in mixture fraction space, the following least squares problem is solved

$$\vec{x} = \arg\min \left\| \begin{bmatrix} A \\ \lambda L \end{bmatrix} \vec{x} - \begin{bmatrix} \vec{b} \\ 0 \end{bmatrix} \right\|_2^2 \quad , \tag{4.16}$$

where L is the smoothing matrix defined as

$$L = \begin{bmatrix} -1 & 1 & \cdots & 0 & 0 \\ \vdots & \vdots & \ddots & \vdots & \vdots \\ 0 & 0 & \cdots & -1 & 1 \end{bmatrix} \in \Re^{(m-1)\times m}, \tag{4.17}$$

which is a discrete representation of the first derivative operator. The prior distribution for first order Tikhonov is defined as

$$P_{Pr}(\vec{x}) = exp(-\alpha_2 \vec{x}^T L^T L \vec{x}), \tag{4.18}$$

where α_2 is a regularization parameter [98].

4.3.3 Bayesian credible intervals

As the posterior probability is a continuous function it is convenient to define credible intervals to quantify uncertainty. Using the method outlined by Charnigo et al. [99] the 95% Bayesian credible interval is defined

$$\int_I P(\vec{x}|\vec{b}) = 0.95, \tag{4.19}$$

where I is the width of the credible interval. Thus, the credible interval is the region which captures $\vec{x}$ with a 95% probability. However, Eq. 4.19 does not uniquely define the credible interval. To uniquely define a credible interval an additional constraint is required. In the present study, the credible intervals are defined following Chen and Shao [100] where the upper and lower credible intervals are calculated as

$$\left(\theta^{(\beta/2)}, \theta^{(1-\beta/2)} \right), \tag{4.20}$$

where $\beta = 0.05$ for the 95% credible interval and θ is the value of the credible interval. For illustration, Fig. 4.8 shows the 95% credible interval for a hypothetical marginal probability distribution. As shown in Fig. 4.8, for the 95% credible interval, 2.5% of the data lie outside each side of the credible interval.

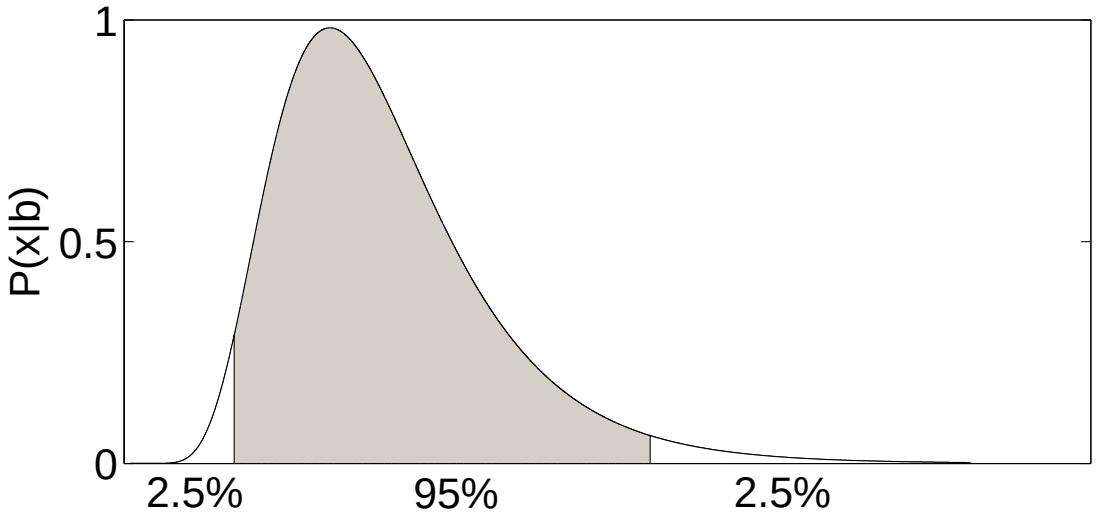

Figure 4.8: Demonstration of 95% credible interval (shaded area)

4.3.4 Estimation of Γ_{noise}

Before a Bayesian analysis can be completed an estimation of the noise matrix is required. In experimental studies the noise matrix often takes the form

$$\Gamma_{noise} = \sigma^2 \times I, \tag{4.21}$$

where σ is the noise in the experimental signal, frequently taken as a constant and I is the identity matrix. This definition of the noise matrix is valid when the the noise is random, homeostatic and uncorrelated. In experimental studies, the noise is often caused by uncertainties in the measurements which is unbiased and uniform for most measurement methods allowing Eq. 4.21 to accurately model the noise. As presented in Section 4.2.2 in the present study, the value of σ is not constant and the perturbations may be modelled as a function of the mean mixture fraction, Z. Thus, similar to Eq. 4.21, the noise matrix can be expressed as

$$\Gamma_{noise} = \sigma^2(Z) \times I. \tag{4.22}$$

A box filter is used to estimate the correlated error as a function of the mean mixture fraction, $\sigma(Z)$. The box filter takes the 12 nearest mean mixture fraction points on either

side of the point of interest. Using these 25 points the standard deviation is calculated and corresponds to an approximation of the error observed in Fig. 4.6 and discussed in Section 4.2.2. Next, the standard deviation profile is smoothed to obtain a continuous function of Z over the entire range of mean mixture fraction values. Γ_{noise} is calculated using Eq. 4.22 and is included in Eq. 4.11. The unsmoothed and smoothed standard deviation profiles are shown in Fig. 4.9.

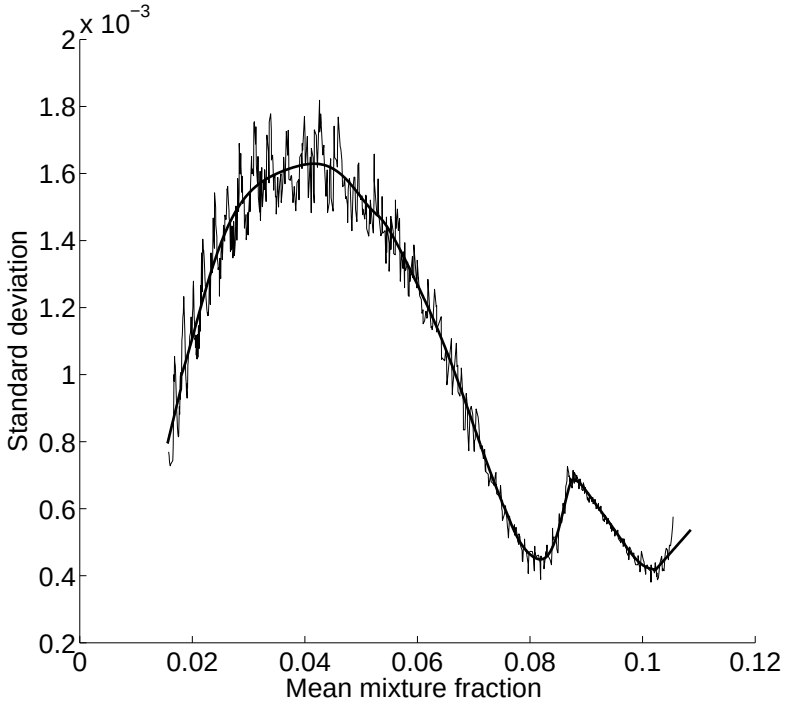

Figure 4.9: Standard deviation of the unconditional mean mass fraction of CO_2 as a function of mean mixture fraction, unsmoothed (thin) and smoothed (bold)

As part of the Bayesian analysis, the recovered solution from the inverse problem needs to be compared with the exact solution in order to evaluate different regularization methods. However, in the current turbulent flame simulations, the exact solution for the conditional species mass fractions is not known. To circumvent this issue, the unconditional species concentrations corresponding to $\vec{b}$, obtained from the CFD-CSE calculations performed in Chapter 3, are not considered. Instead, a new $\vec{b}$ is determined using a known presumed profile for the conditional CO_2 mass fractions following Eq. 4.3 keeping the A matrix from the CFD-CSE simulations. This new $\vec{b}$ is referred to as $\vec{b}_{exact}$ and the presumed

conditional values correspond to $\vec{x}_{exact}$. The conditional profile for a laminar methane air flame is obtained from the experimental profile presented by Peters [23]. Similar to what is done in Section 4.2, any presumed profile for the conditional averages could have been used. $\vec{b}_{exact}$ is then perturbed at each location by applying normally distributed noise with zero mean and the standard deviation calculated using the box filter.

4.3.5 Impact of prior on recovered solution

Before calculating the credible intervals it is important to determine how well the Bayesian solution agrees with the exact solution. This is done by comparing the Maximum a Posteriori (MAP) estimate solution obtained from the MCMC analysis to the exact solution used to calculate the data vector.

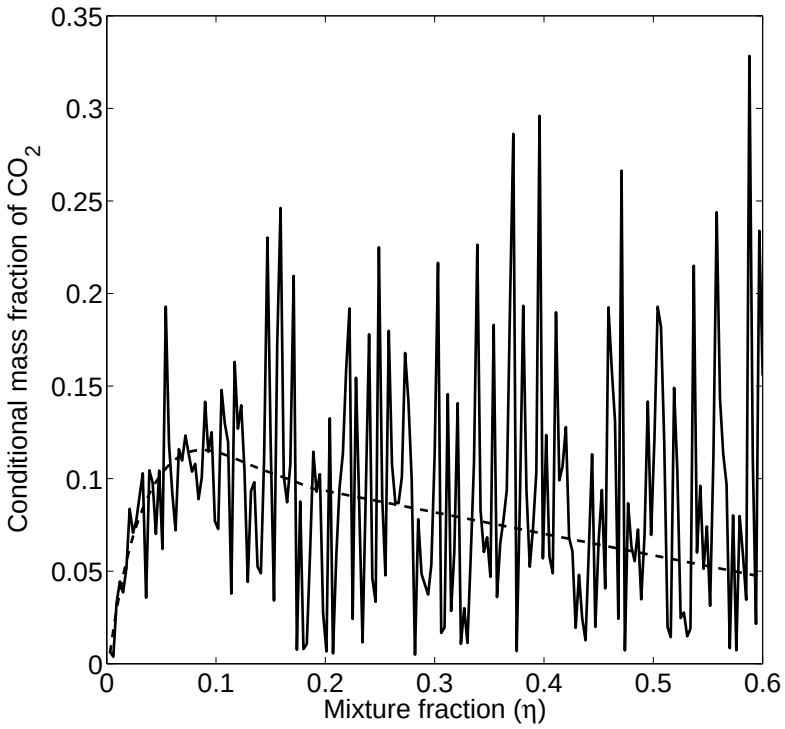

Figure 4.10: MAP estimate with no smoothing prior (solid line) compared to exact solution (dashed line)

The MAP estimate is the solution that maximizes the posterior probability distribution, and considers both the data contained in b, as well as the additional knowledge incorporated through the prior. As a first step, only the non-negativity prior is included, e.g. $\alpha_1 = \alpha_2 = 0$. The initial condition for the MCMC analysis is calculated using Matlab's least squares solver [101, 102, 103, 104] with the initial guess specified as the exact solution perturbed with normal noise. Figure 4.10 shows the MAP estimate obtained using the MCMC algorithm. Figure 4.10 shows that without any smoothing the MAP estimate contains large oscillations about the exact solution, $\vec{x}_{exact}$. Further information can be obtained from the MAP estimate profiles at different values of η.

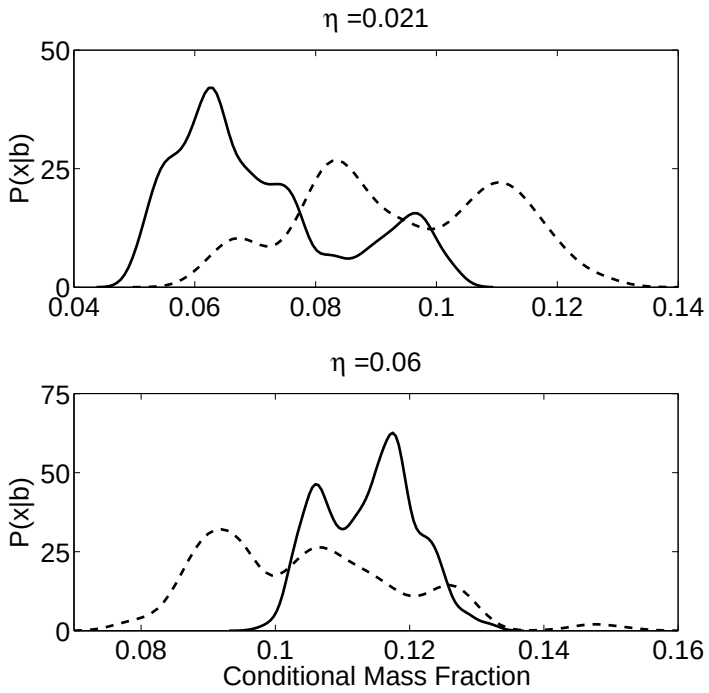

Figure 4.11: The effect of the smoothing prior on the maximum a posteriori estimate profile for two values of η, without a prior, $\alpha_2 = 0$ (dashed line) and with a prior, $\alpha_2 = 4000$ (solid line)

Figure 4.11 shows the MAP estimate at $\eta = 0.021$ (lean) and $\eta = 0.06$ (rich) obtained with and without a prior, $\alpha_2 = 4000$ and $\alpha_2 = 0$, respectively. Without a smoothing prior the MAP estimate is broad which indicates that no preferred solution exists for these

locations. To view the impact of a spatial smoothing prior, α_2 is slowly increased until a noticeable difference is observed in the profiles leading to $\alpha_2 = 4000$. This arbitrary value of α_2 is selected only for the present illustration. In Section 4.3.7, α_1 and α_2 will be determined in a more rigorous manner. As can be seen in Fig. 4.11, the first noticeable effect of adding a spatial smoothing prior is that the width of the marginal profile is reduced by approximately 30% at $\eta = 0.021$ and 50% at $\eta = 0.06$. More importantly, the peaks of the profiles are much more pronounced when the smoothing prior is included and consequently, the MAP is easier to determine. It should be noted that the noisy profiles presented in Fig 4.11 may indicate that the MCMC has not fully converged. Larger samples have been tested and the trends were found to be similar, leading to the same analysis and conclusions as those shown.

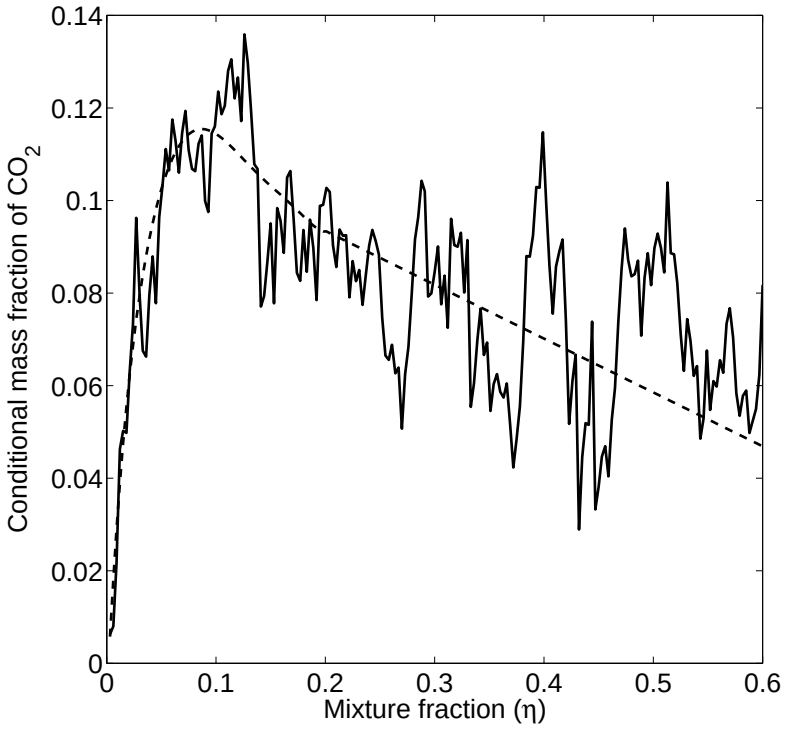

Figure 4.12: The effect of the smoothing prior on the MAP estimate, compared to exact solution (dashed line)

Figure 4.12 presents the effect that the spatial smoothing prior has on the MAP estimate produced by the MCMC method. As can be seen in Fig. 4.12, by including the

spatial smooth prior the magnitude of the oscillations in the solution is greatly reduced. In addition, the recovered solution follows the general shape of the exact solution well and is close to the exact solution between mixture fraction values of 0 and 0.1 corresponding to the η value where peak chemical activity occurs. Similar observations can be made if α_2 is set to 0 and α_1 is increased, corresponding to temporal smoothing. This further demonstrates the usefulness of including priors in the Bayesian analysis.

4.3.6 Impact of priors on credible intervals

The credible intervals are calculated using MCMC to determine the uncertainty in the solutions obtained with and without a smoothing prior, α_2. It is important to appreciate that the credible intervals are estimates and are noisy due to the stochastic nature of the MCMC method. Figure 4.13 shows the 95% credible using only the non-negativity prior.

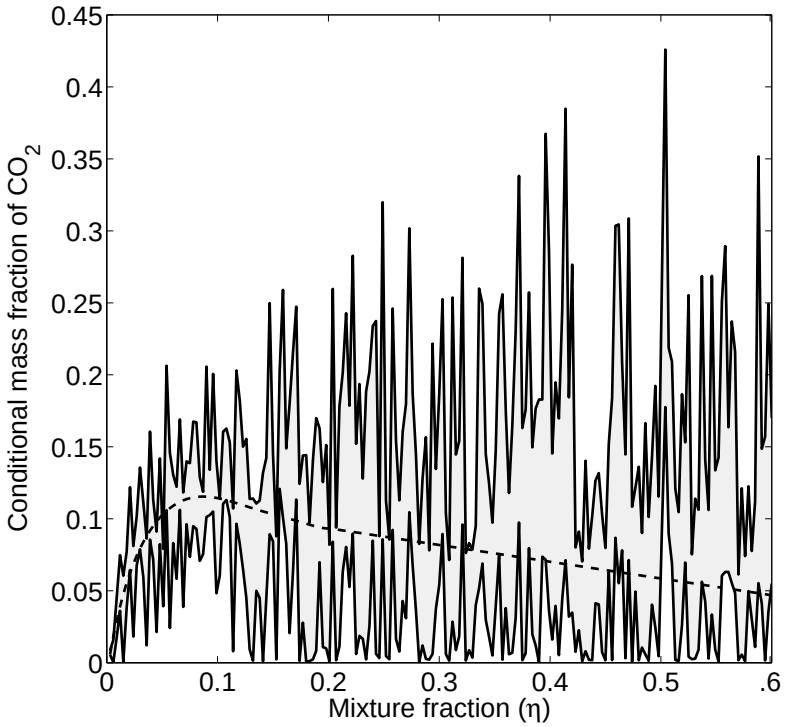

Figure 4.13: 95% credible intervals (shaded area) with no smoothing prior compared to the exact solution (dashed line)

As can be seen in Fig. 4.13, if no smoothing prior is included, corresponding to $\alpha_1 = \alpha_2 = 0$, the credible intervals for $\eta \geq 0.15$ are large. One explanation is that at lower values of η, the A matrix contains sufficient data to reconstruct the solution. However, as the maximum mean mixture fraction seen in the ensemble is approximately 0.11, the PDF values for $\eta \geq 0.15$ are approximately zero. Thus, any given profile in this region will satisfy Eq. 4.3. This indicates that the solution at these locations is uncertain and the posterior probability is indefinable. Since this location of the mixture fraction domain does not have a significant impact on the reaction rates, this uncertainty is not expected to lead to large errors in the CFD simulations. It is also important to note that the exact solution falls within the credible intervals over the majority of the mixture fraction domain. One possible method for reducing the credible intervals at higher values of η is to increase the size of the ensemble. As the ensemble increases additional data from cells with higher values of η are included and additional information will allow for a more accurate reconstruction of the conditional averages at these values. However, there is a limit to how much these ensembles can be enlarged as the assumption of spatially homogeneous conditional averages may break down. As a result, a compromise must be made between increasing the size of the ensemble, to include additional information and ensuring the assumption that the conditional averages are homogeneous remains valid.

Although knowing the credible intervals for the whole mixture fraction domain is desirable, the width of the credible intervals for $\eta \leq 0.15$ are more important as this is the location of maximum chemical reactivity. Figure 4.14 shows the credible intervals for $\eta \leq 0.15$ with and without a smoothing prior. When the smoothing prior is not included, the width of the credible intervals ranges from 0.0028 to 0.1605. This upper limit represents an uncertainty of over 100% of the exact solution. This uncertainty in the conditional mass fractions means that the calculated conditional chemical source terms are also highly uncertain. This uncertainty will also be present in other scalar predictions such as species concentration and temperature. From the analysis in Section 4.3.5 it is expected that when the spatial smoothing prior is included the width of the credible intervals will be reduced which is seen in Fig. 4.14. Further, the credible intervals are much smoother when the smoothing prior is included. This is expected as the smoothing prior enforces smoothness of the solution, preventing large oscillations. More importantly Fig. 4.14 also shows that the width of the credible interval decreases by 55%, with a maximum width of 0.0685. It can be concluded that the addition of a spatial smoothing prior results in a solution which is smooth with smaller error bounds. Similar observations can be made for temporal smoothing corresponding to $\alpha_2 = 0$ by increasing α_1 in Eq. 4.15, this further demonstrating the benefit of priors in Bayesian analysis.

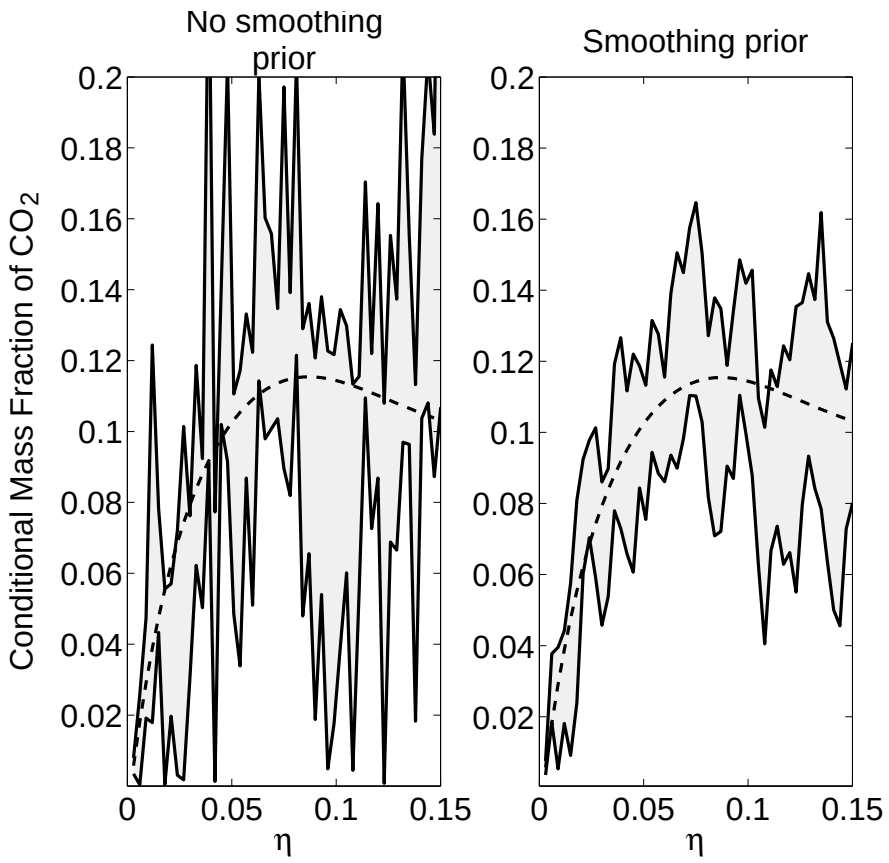

Figure 4.14: 95% credible intervals (shaded area) for $\eta \leq 0.15$ with and without smoothing prior compared to the exact solution (dashed line). No smoothing prior corresponds to the non-negativity prior only, Eq. 4.14 and smoothing prior is spatial smoothing defined by Eq. 4.18 with $\alpha_2 = 4000$

4.3.7 Temporal smoothing vs spatial smoothing

Bayesian analysis is a powerful tool commonly used to obtain statistical information on inversion problems, but is also computationally expensive. Cost factors prevent this method from being used to find a solution to Eq. 4.3 in fully coupled CFD-CSE simulations. For example, in the turbulent non-premixed flame CSE simulation completed in Chapter 3, zeroth order Tikhonov regularization is implemented with 50 mixture fraction bins. The computational time required for the inversion of both CO_2 and H_2O mass fractions averages to 0.028 CPU seconds. A similar order of magnitude is expected for first order Tikhonov or

TSVD. For comparison, the Bayesian analysis presented requires approximately 160 CPU seconds to complete the MCMC simulations for one species. Thus, the Bayesian analysis computational cost is more than 5,000 times as large as what is needed for zeroth order or first order Tikhonov regularization alone. However, statistical information obtained from the Bayesian analysis can be used to prototype less computationally expensive methods to determine if they provide an acceptable solution. This can be accomplished by comparing the solution to Eq. 4.3 using different Tikhonov regularization methods. By using the Bayesian framework, the size of the credible intervals gives an indication of the uncertainty in the solution and can be used to determine which regularization method is best suited for this inversion problem. The regularization methods investigated in this section are zeroth order Tikhonov in time (temporal smoothing) and first order Tikhonov in mixture fraction space (spatial smoothing). For the two methods the regularization parameters are selected to be consistent with Eqs. 3.10, from Chapter 3 and 4.16 and are shown in Table 4.1,

Table 4.1: Regularization parameters

Regularization parameter	Temporal (zeroth order Tikhonov)	Spatial (first order Tikhonov)
α_1	$\frac{\lambda^2}{2\sigma^2}$	0
α_2	0	$\frac{\lambda^2}{2\sigma^2}$

where σ is the average of the standard deviations calculated in Section 4.3.4 and λ is calculated using

$$\lambda^2 = \frac{Tr(A^T A)}{Tr(I)}, \tag{4.23}$$

where Tr is the trace of the matrix [80] and I the identity matrix. These definitions of the regularization parameters are selected so the change in the credible intervals is caused strictly by the change in the regularization methods.

Two different test cases are selected for temporal smoothing. The first test case represents the best case scenario, x_t in Eq. 4.15, is taken as the exact solution and will give an indication of what would occur if all errors could be eliminated from the simulation. For the second test case, x_t is generated by perturbing $\vec{b}_{exact}$ and obtaining a new least squares solution.

Figure 4.15 presents the credible intervals calculated using the two different solutions for x_t and shows that the width of the credible intervals for temporal smoothing are reduced by approximately 80% compared to the credible intervals calculated without using a smoothing prior. When the exact solution is used for x_t, the credible intervals are centred

about the exact solution. However, when the least squares solution is used for x_t, the credible intervals are noisy and follow the shape of x_t. Further, the exact solution does not always fall within the credible intervals. Thus, for temporal smoothing the recovered solution strongly depends on the quality of x_t and λ.

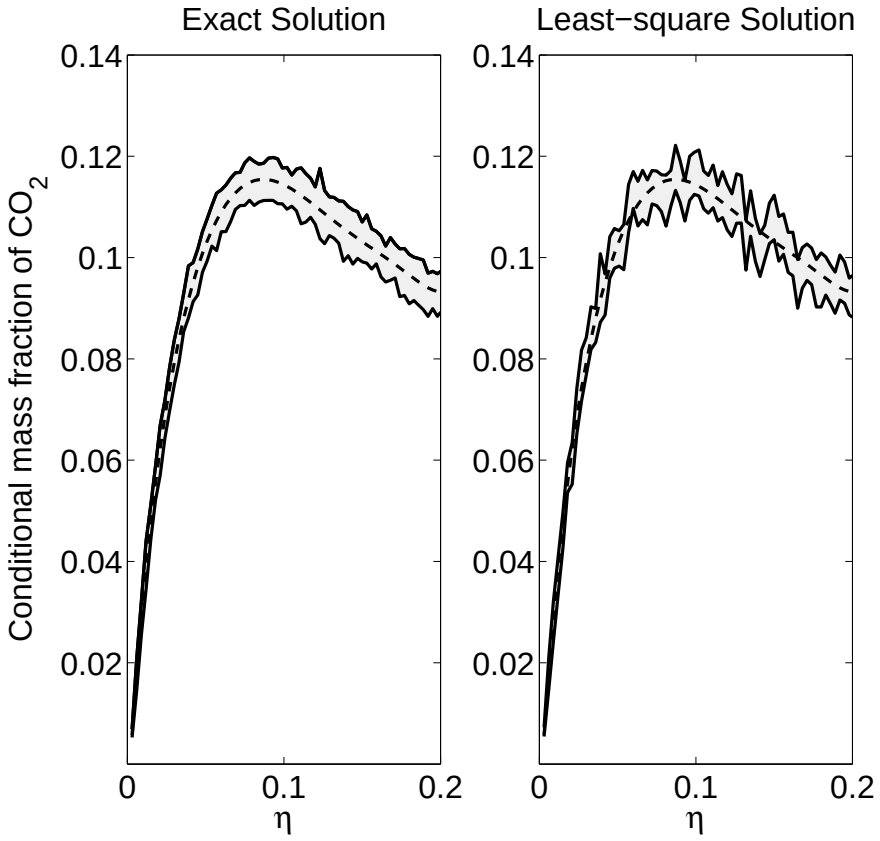

Figure 4.15: 95% credible intervals (shaded area) for zeroth order temporal Tikhonov with different specified x_t profiles, the exact solution (left) and the least squares solution using a perturbed $\tilde{\mathrm{b}}$ (right) compared to the exact solution (dashed line)

The alternative to temporal smoothing is spatial smoothing using first order Tikhonov as shown in Eq. 4.18. An attractive feature of spatial smoothing is that it only relies on one parameter, λ, eliminating x_t as a possible source of error. However, it is important to determine if spatial smoothing results in similar credible intervals. Figure 4.16 shows the credible intervals calculated for the first order Tikhonov regularization method. The

width of the credible intervals for spatial smoothing are similar to temporal smoothing, are not centred about the exact solution and contain small oscillations. Based on these characteristics it appears that first order Tikhonov is a good method for obtaining recovered solutions with small uncertainties.

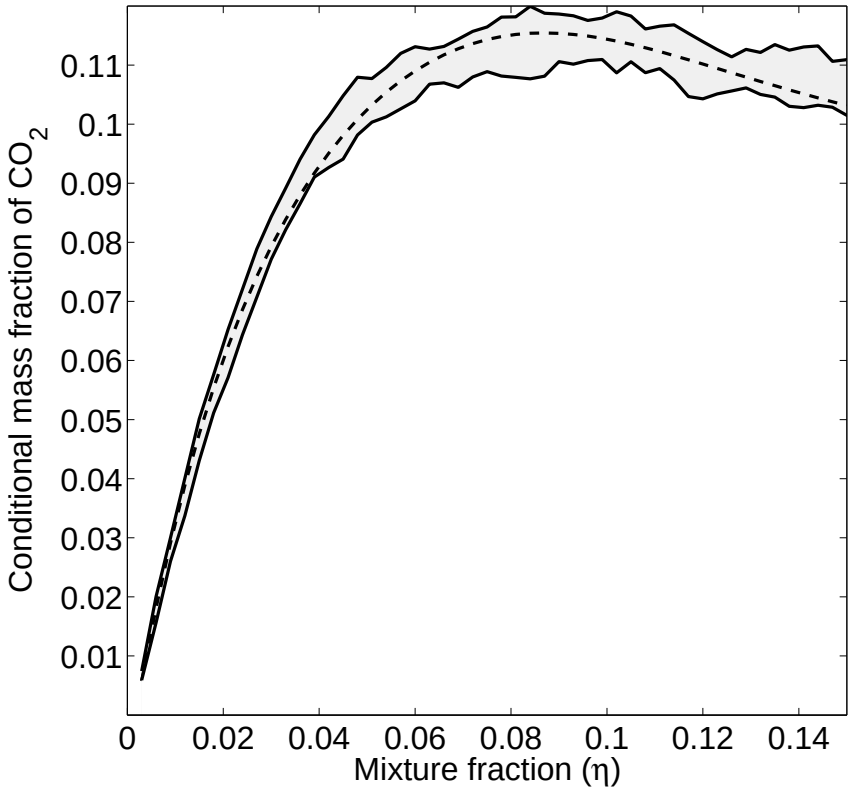

Figure 4.16: 95% credible intervals shaded area) for first order Tikhonov compared to the exact solution (dashed line) with $\alpha_2 = \lambda^2/(2\sigma^2)$, as shown in Table 4.1

It is also important to note that for both temporal and spatial smoothings the width of the credible intervals is not constant and increases past $\eta = 0.08$, but for values of η less than 0.08 the credible intervals are similar. This can be explained by the fact that for $\eta \leq 0.08$ the A matrix contains sufficient information to accurately predict the conditional mass fraction of CO_2. Outside this range, the A matrix contains little information and the retrieved/calculated conditional mass fraction is much more uncertain. Figure 4.17 shows

the credible intervals for $\eta \geq 0.2$ for temporal and spatial smoothing. As seen from Fig. 4.17, this increase in uncertainty is better predicted by spatial smoothing as the solution is not required to be close to any predefined profile. In comparison, the width of the credible interval remains approximately constant and is centred about the exact solution when using temporal smoothing. Thus, at this location the recovered solution using temporal smoothing is defined completely by the choice of x_t.

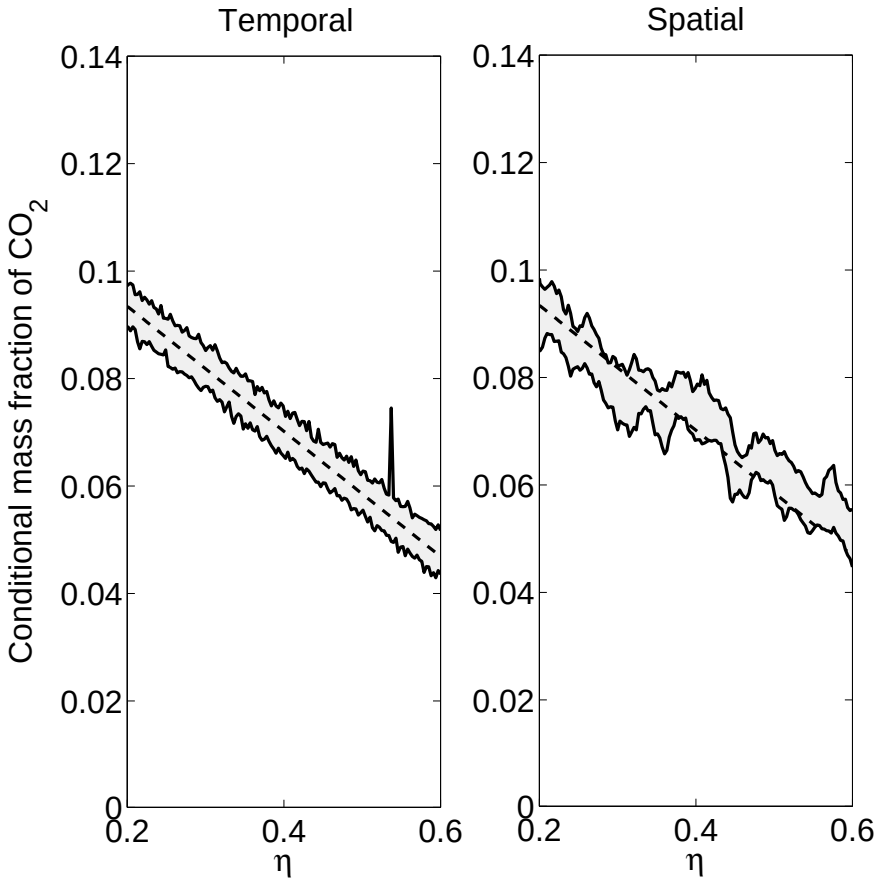

Figure 4.17: 95% credible intervals (shaded area) for temporal and spatial smoothing for $\eta \geq 0.2$, compared to the exact solution (dashed line)

It appears that both zeroth order temporal and first order spatial Tikhonov regularizations are plausible methods to obtain solutions to Eq. 4.3. However, it is difficult to determine which method is superior without a fully coupled CFD-CSE simulation comparison. Zeroth order temporal Tikhonov has been applied to actual simulations with good results. The analysis shows the recovered solution from this method strongly depends on the solution from the previous time step. However, it does not enforce a smooth solution, so convergence to a solution may be difficult. This problem can be avoided by including post-processing smoothing which can stabilize the solution, but this may not be a preferred step. Further, this method requires additional computational resources as the solution at the previous time must be stored. This can become problematic as the number of CSE domain increases or if detailed chemistry is included without tabulated tables. An accumulation of errors is possible when temporal smoothing is considered, which could result in large errors in the solution or divergence, particularly in areas where very little information is available in the A matrix. The problem of error accumulation is not present in first order Tikhonov as no information about the previous solution is used. This is an additional benefit of using first order Tikhonov over zeroth order Tikhonov. It should be noted that divergence of the solution has never been encountered in the fully coupled CSE simulations completed in Chapter 3. First order spatial Tikhonov regularization does not require any additional storage and does not rely on previous time steps, which makes this method attractive for CSE. However, in typical CFD-CSE simulations, the mixture fraction grid is non-uniform. As a result, the formulation for the smoothing matrix, L, must be defined for each simulation. This process is further complicated if a second conditioning variable is introduced as it would be for partially-premixed or MILD combustion. In this situation, a two dimensional smoothing matrix must be defined. Although first order spatial Tikhonov regularization is more mathematically complex compared to zeroth order temporal regularization, it appears to be a promising alternative.

4.4 Summary

A detailed study of the inverse problem encountered in CSE has been completed. It is found that the unconditional species mass fractions obtained from the CSE simulations contain perturbations. These perturbations may be caused by the use of a discrete mixture fraction grid, which results in inaccurate predictions of the PDF for very lean mixture fractions.

The Bayesian framework is used to investigate the impact of a smoothing prior on the recovered solution and credible intervals. The perturbations are approximated as a func-

tion of the mean mixture fraction and modelled using a non-uniform standard deviation. A new data vector is calculated using a known conditional profile and then perturbed at each location using normal distributed error, to enable a comparison between the recovered and exact solutions. It is found that including a smoothing prior decreases the credible interval width and the recovered solution better approximates the exact solution. As well, with the inclusion of a smoothing prior a narrower marginal probability with a more distinct peak is seen.

Two regularization methods, zeroth order temporal Tikhonov and first order spatial Tikhonov, are implemented in the Bayesian framework. Credible intervals are calculated to determine the level of uncertainty in the recovered solution. The width of the credible intervals calculated for zeroth order temporal Tikhonov and first order spatial Tikhonov are found to be similar. Further, for zeroth order temporal Tikhonov the credible intervals are not necessarily smooth and are dependent on the solution from the previous time step. In contrast, the credible intervals for first order spatial Tikhonov are smooth and not dependent upon a previous solution. First order spatial Tikhonov is found to better predict the characteristics of the credible intervals for higher mixture fraction values. Thus, first order spatial Tikhonov regularization is a promising alternative method for recovering a solution from the CSE inversion process.

Chapter 5

CSE simulations of a semi-industrial furnace

In this chapter, the non-premixed CSE formation from Chapter 3 is extended to include an enthalpy variable in the TGLDM tabulation. This represents the first time a CSE formulation which accounts for enthalpy in the TGLDM tabulations is applied to a semi-industrial MILD furnace. Chapter 3 demonstrated that CSE can accurately predict the flame characteristics of non-premixed flames, with low radiative heat loss. The semi-industrial furnace studied in this chapter has a high radiative heat loss which requires an additional variable in the TGLDM tabulation.

The objective of the current chapter is to determine if a CSE formulation which accounts for changing enthalpy of the mixture can correctly predict the flow characteristics seen in the semi-industrial MILD furnace. The CSE predictions are compared to available experimental data for the mean axial velocity, temperature and species profiles.

5.1 CSE formulation with radiation

The CSE formulation from Chapter 3 is selected to obtain the conditional mass fraction of CO_2 and H_2O as outlined in Section 3.1.1 and 3.1.2. In addition, the conditional enthalpy is calculated by inverting the following integral

$$\widetilde{h}(x_j,t) = \int_0^1 \langle h|\eta(\eta,t)\rangle \widetilde{P}(\eta,x_j,t)d\eta, \tag{5.1}$$

where x_j is the spatial coordinate, t the time and $\widetilde{P}(\eta)$ the Favre-averaged PDF of mixture fraction. In the present study, a presumed β-PDF distribution is used to model $\widetilde{P}(\eta)$ [73]. With the addition of the conditional enthalpy the TGLDM manifolds are tabulated as a function of mixture fraction, CO_2 and H_2O mass fractions, and enthalpy and the mean chemical source term is retrieved using

$$\overline{\dot{\omega}_k}(x_j,t) = \int_0^1 \langle \dot{\omega}_k|\eta\rangle(\langle Y_{CO2}|\eta\rangle, \langle Y_{H2O}|\eta\rangle, \langle h|\eta\rangle)\overline{P}(\eta, x_j, t)d\eta. \tag{5.2}$$

5.1.1 Ensemble selection

In each ensemble the conditional enthalpy, and CO_2 and H_2O mass fractions are assumed to be homogeneous and are obtained via the inversion process. In the past, different methods were applied to determine the ensembles based on a priori information about the flame. For premixed flames, a single ensemble covering the entire CFD domain has been defined in RANS simulations [45, 46], whereas for LES-CSE premixed simulations, the ensembles have been selected as subsections of the CFD grid [47]. For non-premixed combustion, the ensembles are usually defined as sections of planes perpendicular to the mean flow direction for jet flames. In the current study, a weak-strong jet interaction is observed and significant recirculation of burn products is present. Therefore, the conditional averages may vary along planes perpendicular to the mean flow direction. Thus, the ensembles are defined as rectangular sections of the CFD domain with a higher density of CSE ensembles near the fuel/jet interaction. Two simulations are completed to test the sensitivity of the CSE predictions to the number of the ensemble, one with 26 ensembles and one with 52 ensembles. Further detail is reported in Section 5.4.4.

5.1.2 Chemistry tabulation

Chemistry is tabulated using the TGLDM approach [105] prior to the simulations, for computational savings. The manifolds are stored in tables and are a function of four variables: mixture fraction, enthalpy, and CO_2 and H_2O mass fractions. Detailed chemistry is included using the GRI 2.11 mechanism [81] for methane-air combustion. The unconditional chemical source term is obtained using

$$\overline{\dot{\omega}_k}(x_j,t) = \bar{\rho}\int_0^1 \frac{\dot{\omega}_k^{TGLDM}}{\langle\rho|\eta\rangle}\widetilde{P}(\eta, x_j, t)d\eta, \tag{5.3}$$

where

$$\dot{\omega}_k^{TGLDM} = f(\langle Y_{CO2}|\eta\rangle, \langle Y_{H2O}|\eta\rangle, \langle h|\eta\rangle). \tag{5.4}$$

5.2 Experimental conditions

Experimental data is available from the IFRF experiments for a refractory lined semi-industrial scale furnace [57]. The furnace dimensions are 2 m x 2 m x 6.25 m and operates with a single burner. At steady-state operation, a fuel input of 0.58 MW is fed to the furnace with 0.35 MW of vitiated air. The experimental fuel is natural gas containing 87.8% CH_4, 4.6% ethane (C_2H_6), 1.6% propane (C_3H_8), 0.5% butane (C_4H_{10}) and 5.5% N_2 in volume. The vitiated air consists of 59.1% wet N_2, 19.5% wet O_2, 6.4% wet CO_2, 15% wet H_2O and 110 vppm (volume parts per million) dry nitric oxide (NO) [60]. The inlet temperatures for the fuel and vitiated air are reported to be 298.15 K and 1573.15 K, respectively. The vitiated air is supplied through a 124 mm diameter central jet with a velocity of approximately 85 m/s, while the natural gas is supplied through two injectors located 280 mm away from the burner centreline with an injection velocity of approximately 100 m/s. In addition, the furnace exit gases are measured and contain 1.6% wet O_2 and 140 vppm dry NOx. Steady state experimental measurements of the temperature and gas composition are obtained using a suction pyrometer and a gas sampling probe, respectively. Volume fractions for O_2, CO, CO_2, CH_4, H_2, and NOx are determined using a crank probe, obtained under a quenching rate of 10^7-10^8 K/s [57]. Experimental turbulent velocities were measured using Laser Doppler Velocimetry (LDV) and the furnace wall temperature is obtained using type B thermocouples. The experimental measurements used in the present study were obtained by traversing the furnace in the horizontal plane of the two fuel injectors.

5.3 Computational details

The computational domain closely follows the experimental set-up. Three dimensional RANS simulations are performed on one quarter of the furnace using two symmetry boundary conditions. The computational domain consists of approximately 520,000 cells with a higher density of cells near the fuel and vitiated air inlets. A schematic of the computational domain is also presented in Fig. 5.1.

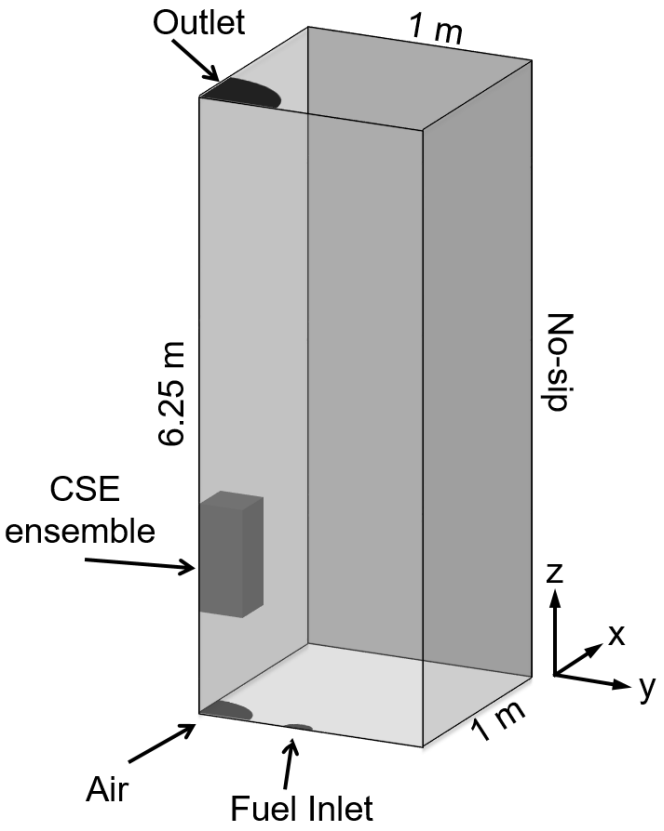

Figure 5.1: RANS computational domain showing one CSE ensemble and boundary conditions (not to scale)

Transport equation are solved for mass (continuity), momentum, enthalpy, mixture fraction and its variance, and the mass fraction of H_2O and CO_2. The mass fraction of CH_4, O_2, CO, OH, nitrogen dioxide (NO_2) and H_2, are obtained by integrating the conditional mass fraction interpolated from the TGLDM chemistry tables. In addition, a transport equation for NO is solved in a post-processing step using the steady-state flow-field. First, the forward and backward reaction rates of NO are obtained from the TGLDM tables based on the steady state conditional averages of H_2O and CO_2. Next, the net chemical source term of NO is calculated as

$$\dot{\omega}_{NO} = \dot{\omega}^{+}_{NO} + Y_{NO}\frac{\dot{\omega}^{-}_{NO}}{Y^{TGLDM}_{NO}}, \tag{5.5}$$

where $\dot{\omega}_{NO}^{+}$ is the production of NO, $\dot{\omega}_{NO}^{-}$ the destruction of NO, Y_{NO}^{TGLDM} the NO mass fraction from the TGLDM tables and Y_{NO} the mass fraction of NO from the CFD domain [106]. In the transport equation of h, radiation is included using an optically thin radiation model for the main combustion products H_2O and CO_2 and the natural gas fuel is approximated as 100% CH_4 following the work of Kim et al. [68]. In the present study, conjugate heat transfer is not included for the furnace walls and the wall temperature is assumed to be constant with an average temperature estimated from the experimental data. Closure for the Reynolds stresses is provided using the standard $k - \epsilon$ turbulence model consistent with previous studies of the same experimental conditions [60, 68, 107, 108].

5.4 Results

Velocity and temperature profiles are compared to available experimental data at six axial locations. Species predictions for CH_4, O_2, CO, H_2, CO_2, H_2O and NOx concentrations are compared at three axial locations, the same as those selected by Kim et al. [68]. All results presented in Sections 5.4.1-5.4.3 are obtained with 26 ensembles. In addition, the sensitivity of the predictions to the CSE ensembles is investigated for the temperature and species concentrations.

5.4.1 Velocity

The axial velocity profiles are compared to the experimental data at six axial locations and shown in Fig. 5.2. As can be seen in Fig. 5.2, 15 cm downstream of the jet exit, the computed velocity profile for the vitiated air is in very good agreement with the experimental data. At this location the velocity profile of the fuel stream is slightly shifted towards the vitiated air stream and is approximately 3 m/s higher than the experimental value at a radial distance of 25 cm. Farther downstream, at 45 cm, the velocity close to the centreline is in good agreement with the experimental data and a slight underprediction of approximately 4.5 m/s is seen at a radial location of 25 cm. Past 45 cm, the velocity profiles close to the centreline match the experimental data very closely. For axial locations larger than 73 cm, the CSE simulations show a slightly stronger recirculation compared to the experimental measurements close to the walls. The present results demonstrate that the current simulations accurately reproduce the weak/strong jet interaction and recirculation within the furnace.

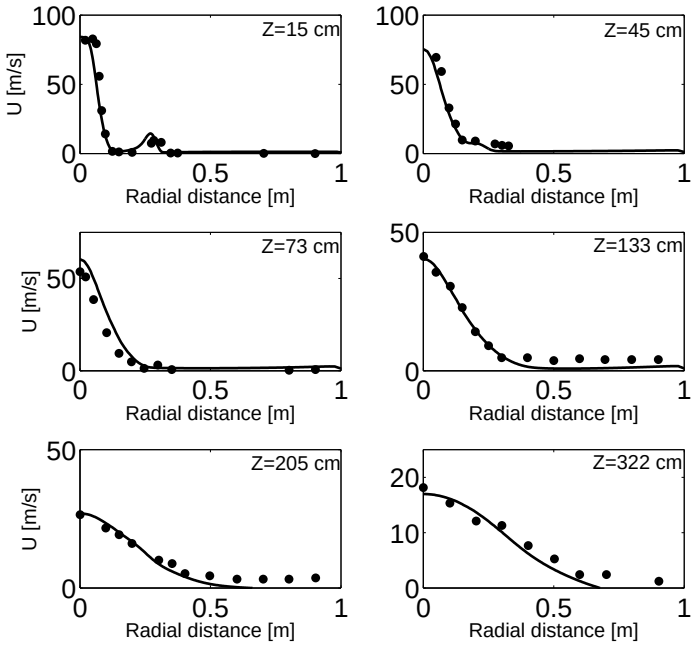

Figure 5.2: CSE mean velocity profiles (solid lines) compared to the experimental data [57] (symbols) at various axial locations

5.4.2 Temperature

The temperature profiles are investigated to determine if the CSE model can accurately predict the reaction zone location and interaction between the reaction zone and circulating hot products. The experimental temperature profiles are compared to the CSE results in Fig. 5.3.

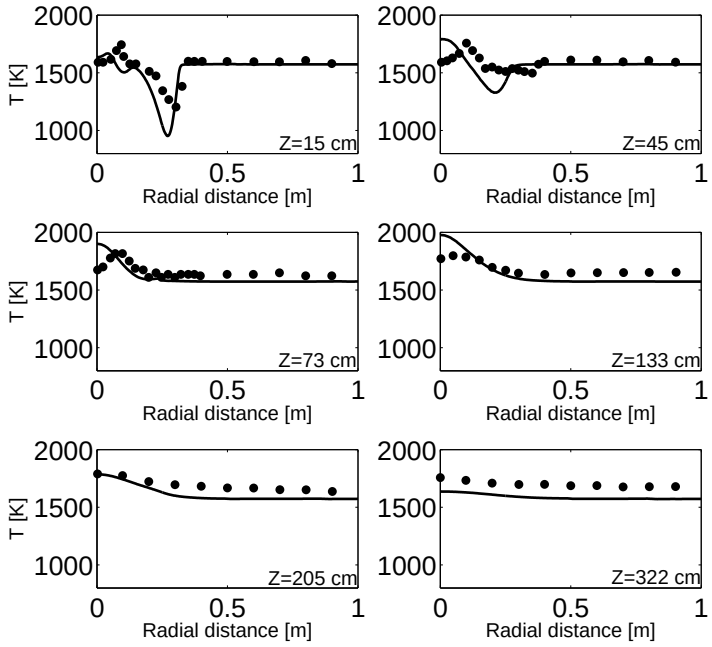

Figure 5.3: CSE radial temperature profiles (solid lines) compared to the experimental data [57] (symbols) at various axial locations

Close to the nozzle at 15 cm, the CSE centreline temperature is in good agreement with the experimental data. At this location, the peak temperature is underestimated by approximately 5% and the temperature of the fuel jet region is approximately 20% lower than the experimental data. The underprediction of the temperature may indicate that the interaction between the recirculated hot products, vitiated air and the cold fuel jet is not accurately modelled. A similar trend for the temperature is seen in [60, 68]. In the recirculation zone the temperatures match the experimental profiles very well. Farther downstream, at 45 cm, the calculated peak temperature is within 3% of the experimental value, but the location of the peak temperature in the simulations is much closer to the centreline compared to what is seen in the measurements. This suggests that the mixing between the fuel and vitiated air jet is not accurately reproduced and the fuel jet is entrained towards the centreline too quickly. At this location, the underprediction of the temperature for radial distances between 20 and 30 cm has decreased to less than 15% as the fuel jet continues to mix with the recirculated products. Farther downstream, the centreline temperature is higher than the experimental data by 14% and 12%, at 73 cm and

133 cm, respectively. Away from the centreline the predicted temperature is within 5% of the experimental data. For the last two axial locations, 205 and 322 cm respectively, the temperature is in good agreement with the experimental profile, with slightly lower temperature compared to what is experimentally observed. The higher temperature observed near the centreline may be a result of using the optically thin radiation model or may be due to the overestimation of the centreline temperature upstream. A more advanced and accurate radiation model may be required to accurately predict the temperature profiles, and their impact on the simulation results needs to be investigated in the future. Similarly, the lower temperature near the wall for axial locations 133 and 322 cm may be a consequence of assuming a constant wall temperature for the furnace. In the experimental data the wall temperature varies by approximately 100 K between an axial height of 15 and 322 cm. Thus, including conjugate heat transfer for the walls is expected to improve the calculated temperature profiles near the walls.

5.4.3 Species concentration

The CO_2 and CO dry volume fractions are compared to the experimental data at three axial locations and are shown in Fig. 5.4. Near the burner exit very good agreement is seen between the CO volume fractions and the experimental values. At this location, the CO_2 volume fractions obtained in CSE are lower than the measurements past a radial distance of 35 cm by approximately 3%. Closer to the centreline where the vitiated air jet and fuel jets mix, an underprediction of between 10 and 50% is observed. The lower CO_2 volume fraction indicates that production of CO_2 is underestimated very close to the burner exit. Farther downstream, at 73 cm, the CO profiles are in good agreement with the experimental data with the peak CO volume fraction approximately 10% lower than what is seen experimentally. The CO_2 profiles at this location remain underpredicted for radial distances between 14 and 25 cm, but follow the general trend seen in the experimental profiles. Further, the significant increase in CO_2 between these locations, which is also observed experimentally, demonstrates that the CSE model correctly replicates a strong reaction zone between these two locations. At the final axial location very good agreement is found between the CSE predictions of CO_2 and the experimental data. For CO the correct magnitude is obtained from the simulations but the general shape of the profile is not accurately captured.

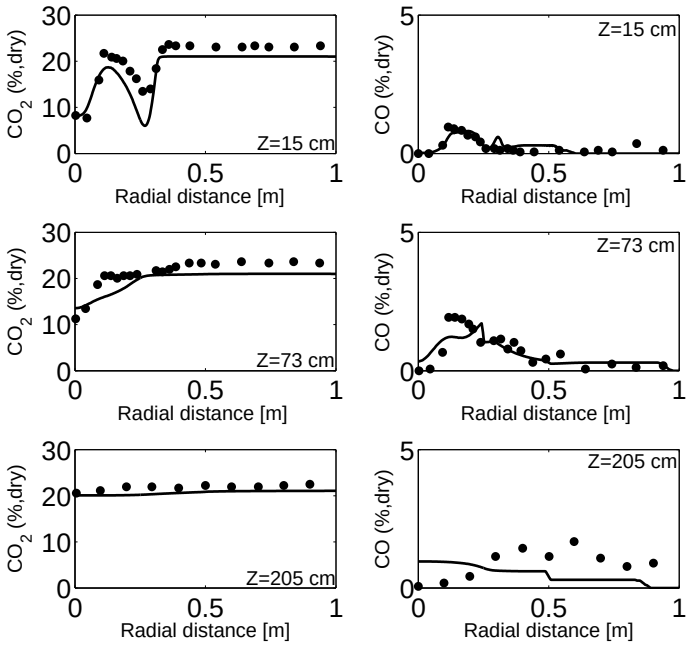

Figure 5.4: CSE radial CO_2 and CO concentration (volume, dry) profiles (solid lines) compared to the experimental data [57] (symbols) at three axial locations

The dry volume fractions of CH_4 and O_2 for the three axial locations are presented in Fig. 5.5. Near the burner exit, good agreement for the O_2 predictions is observed. At the same axial distance, the peak of the CH_4 volume fraction is significantly higher than what is observed experimentally. A similar trend for the CH_4 volume fraction is also seen in [60, 68], using the EDC, PDF/mixture fraction and EBU combustion models. The difficulty in accurately predicting the concentration of CH_4, CO_2 and temperature in the fuel jet has been observed for different combustion models [60, 68, 108]. Mancini et al. [109] further investigated this phenomenon and determined that the inability to accurately model the species and temperature in the fuel jet is not related to the chemistry submodel. Instead, they determined these errors are due to limitations of the RANS approach to replicate the structure of the weak jet [109]. Improved modelling for the weak jet structure is expected using LES, but is beyond the scope of the current study. At 73 cm, the calculated CH_4 concentration profile is in good agreement with the experimental value and the peak CH_4 volume fraction is within 8% of the experimental data. The CSE simulations show a slightly narrower CH_4 profile with a peak closer to the centreline. This behavior may explain why

the CSE results produce higher peak temperatures closer to the centreline, as shown in Fig 5.3. For the O_2 volume fraction very good agreement is seen at 15 and 73 cm. Farther downstream, at 205 cm, the centreline O_2 concentration is significantly underpredicted, consistent with the results of Kim et al. [68] who also estimated the fuel as pure CH_4.

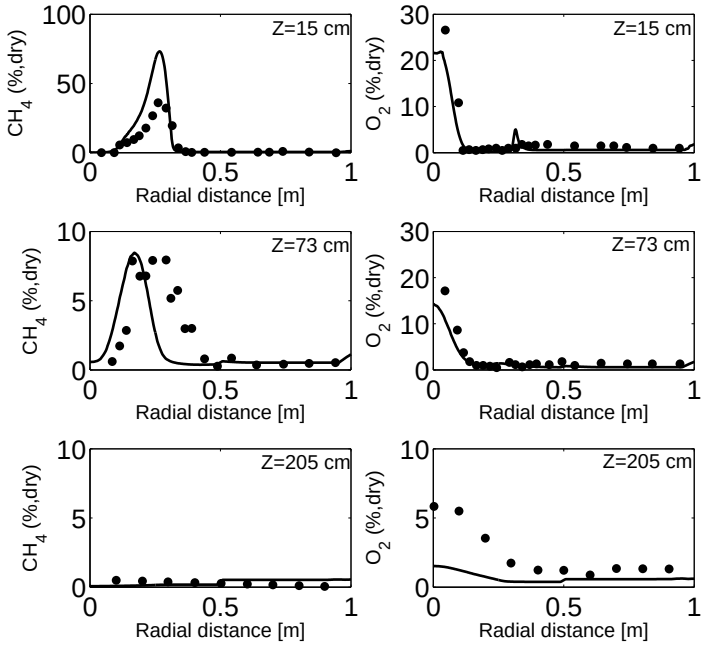

Figure 5.5: CSE radial CH_4 and O_2 concentration (volume, dry) profiles (solid lines) compared to the experimental data [57] (symbols) at three axial locations

In addition, the volume fractions of H_2 and NOx are also examined and shown in Fig. 5.6. As can be seen in Fig. 5.6, the H_2 profiles are not as good as the results for CH_4, O_2, CO and CO_2. The H_2 volume fraction is higher than the experimental profile at 15 cm and contains two peaks, similar to the EDC predictions of Kim et al. [68]. Farther downstream, the peak H_2 volume fraction is underestimated by approximately 64% and 78% at an axial height of 73 cm and 205 cm, respectively. The NOx concentrations are in good agreement with the experimental measurements at 15 and 73 cm. Farther downstream, at 205 cm, the centreline concentration of NOx is lower than the measurements. The current TGLDM tables have some difficulty predicting the NOx concentrations due to the

high level of NO in the oxidizer stream. Currently, the species concentrations at the start of each trajectory are calculated using conservation of elements and a one-step chemical mechanism, which excludes NO . The initial NO concentration at each trajectory is then approximated based on the oxidizer and fuel mixture. Improvement of the NOx predictions could be obtained by post-processing the NOx reaction rates similar to [60] or by improving the TGLDM tabulation approach by using a more sophisticated method of estimating the NO concentrations at the start of each trajectory.

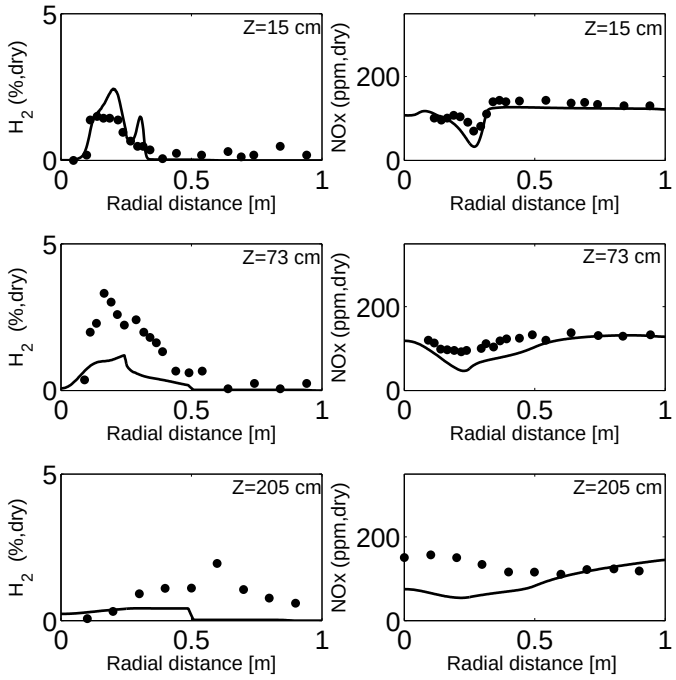

Figure 5.6: CSE radial H_2 and NOx concentration (volume, dry) profiles (solid lines) compared to the experimental data [57] (symbols) at three axial locations

5.4.4 Sensitivity to CSE ensemble selection

In previous CSE simulations, the conditional and unconditional species mass fractions have been shown to have some sensitivity to the definition of the ensembles. In the present study, two different sets of CSE ensembles are selected to ensure the present results are not affected by the definition of the CSE ensembles. First, the CO_2 volume fraction and temperature are compared. The three axial locations shown in Fig 5.4 are selected to determine the differences in the CO_2 volume fraction and temperature and are included in Table 5.1.

Table 5.1: Maximum absolute difference between the CSE predictions for 26 and 52 ensembles at three axial locations. Species concentration, X_{CH_4}, X_{CO_2}, X_{O_2}, X_{CO} and X_{H_2} are (%, dry). 15, 73 and 205 cm are axial locations

Variable	15 cm	73 cm	205 cm
T (K)	27	49	9
X_{CH_4}	1.9	1.3	0.3
X_{CO_2}	0.6	0.4	0.1
X_{O_2}	0.6	0.5	0.2
X_{CO}	0.3	1.4	0.2
X_{H_2}	1.8	1.0	0.4

As can be seen in Table 5.1, the maximum difference in the predicted temperature is less than 50 K. For the CO_2 volume fraction, the maximum difference occurs at 15 cm with the two simulations predicting a volume fraction of 18.3% and 18.9%, respectively. This represents a relative difference between the two simulations of approximately 6%. Thus, the CO_2 volume fraction and temperature are not very sensitive to the ensembles selected in the current study. Also included in Table 5.1 are the differences in the predicted species volume fraction obtained via the TGLDM tables (CH_4, O_2, CO and H_2). For these species larger relative differences are seen between the two sets of ensembles. As there is not clear improvement in the results using the refined set of ensembles, the coarser set of ensembles is used to reduce the computational requirements of the simulation.

5.5 Summary

In the present work, the effect of radiation on the conditional reaction rates is accounted for by calculating the conditional enthalpy. The extended CSE approach is applied with the standard $k - \epsilon$ turbulence approach to model a semi-industrial MILD furnace with detailed measurements for temperature, velocity and species concentration.

The peak velocities and general shape of the axial velocity profiles at each axial location are in good agreement with the experimental data. The recirculation is slightly stronger than that seen in the experimental results and the axial velocity of the fuel jet region is slightly underpredicted away from the centreline. The temperature profiles are also in good agreement for most axial positions. The location of the predicted peak temperature is closer to the centreline compared to the experimental observations, suggesting that the mixing between the fuel jet and vitiated air jet is overestimated at this location and the fuel jet is entrained towards the centreline too quickly. Good agreement between the predicted species concentrations and the experimental data is observed. Near the burner exit, the CO_2 concentration is lower than the experimental data near the fuel jet and a corresponding higher CH_4 concentration is observed, consistent with the results of [60, 68]. The NOx concentrations are in good agreement with the experimental measurements near the burner exit. Farther downstream the centreline concentration of NOx is found to be underpredicted. The major species and temperature predictions are shown to be independent of the CSE ensembles tested. The minor species, (H_2 and CO), exhibit some sensitivity to the CSE ensembles. However, the finer ensemble set does not improve the CSE predictions significantly.

The current study indicates that RANS-CSE can accurately predict the species concentration seen in a semi-industrial MILD furnace. Improved NOx predictions are expected by changing the TGLDM tables to properly account for the NO in the oxidizer stream. Further improvements are expected by extending the current formulation to LES so that the time dependent and 3-D interaction between the weak and strong jets can be better modelled. In addition, the implementation of conjugate heat transfer boundary conditions for the walls and an improved radiation model could be considered to further improve the species and temperature predictions.

Chapter 6

Two mixture fraction CSE for MILD combustion

This chapter is focused applying RANS-CSE in the context of a three stream MILD combustion burner. The objective of the current chapter is to assess the capabilities of CSE to accurately reproduce the velocity field, temperatures and lift-off height using the Delft-Jet-in-Hot-Coflow (DJHC) experimental conditions [54, 55]. In the following sections, the CSE formulation is presented, the experimental conditions and computational details are given and the CSE results are compared with available experimental data [54, 55], previous Eddy Dissipation Concept (EDC) results [29] and stochastic fields combustion model [9] predictions, whenever available.

6.1 Mulitstream CSE formulation

6.1.1 Theory

CSE uses conditional averages to determine the Favre-averaged chemical source term in a turbulent reacting flow. The principle is similar to the CMC approach. In CMC, the conditional averages are determined by solving transport equations [24]. In contrast, in CSE, the conditional averages are calculated by inverting an integral equation. In non-premixed combustion, a conserved scalar called mixture fraction is commonly used as the conditioning variable. However, in cases where the coflow is not uniform or when multiple streams are present, an additional conditioning variable, which accounts for the variation

in the third stream, is required to obtain accurate predictions. In MILD combustion, where the oxygen concentration in the coflow is not constant, a second mixture fraction is needed and can be defined [65] as

$$W = \frac{Y_O - Y_O^{O(0)}}{Y_O^{O(1)} - Y_O^{O(0)}}, \tag{6.1}$$

where $Y_O^{O(0)}$ and $Y_O^{O(1)}$ are the minimum elemental oxygen mass fraction in the coflow and elemental oxygen mass fraction of the air stream, respectively. By defining W in this manner, it is independent of Z, the first mixture fraction defined according to the amount of fuel in the flow. Z is equal to zero when no fuel is present and unity when pure fuel is found. For the two mixture fractions the sample space variables are defined as η for Z and υ for W. The definition of W can also be derived using elemental mass fractions following the formulation of Bilger et al. [110], but is found to be more difficult to implement due to the mixture fraction dependence of W and sensitivity to small errors in the measured species mass fractions [65]. In a later study, Ihme et al. [111] refine the definition of the oxidizer split by introducing a dependence on Z and using a modified oxidizer split that remains statistically independent on Z. The numerical predictions reported in [65] do not appear to be significantly different than those shown in [111].

In multiple-stream problems, where the conditional averages are conditioned on two variables, it is reasonable to assume that first order closure is valid, as the fluctuations about the doubly conditioned averages should be even smaller than the fluctuations about the singly conditioned scalars [112]. Thus, the conditional chemical source term for the k^{th} species, $\langle \dot{\omega}_k | \eta, \upsilon \rangle$ can be assumed to be only a function of $\langle Y_k | \eta, \upsilon \rangle$, $\langle T | \eta, \upsilon \rangle$, $\langle Y_k | \eta, \upsilon \rangle$ being the conditional mass fraction for species k and $\langle T | \eta, \upsilon \rangle$ the conditional temperature. The conditional averages are determined by inverting Eq. 6.2

$$\widetilde{Y}_k(x_j, t) = \int_0^1 \int_0^1 \langle Y_k | \eta, \upsilon \rangle (\eta, \upsilon, x_j, t) \widetilde{P}(\eta, \upsilon, x_j, t) d\eta d\upsilon, \tag{6.2}$$

where x_j is the spatial coordinate, t is the simulation time and $\widetilde{P}(\eta, \upsilon, x_j, t)$ is the Favre-averaged joint PDF of Z and W. Since Z and W are independent [65], it is possible to rewrite the joint PDF as $\widetilde{P}(\eta, \upsilon, x_j, t) = \widetilde{P}(\eta, x_j, t) \cdot \widetilde{P}(\upsilon, x_j, t)$. A presumed β-PDF distribution is used to model $\widetilde{P}(\eta)$ and $\widetilde{P}(W)$ [73]. The mean and variance of W and Z are needed for the PDFs and obtained by solving transport equations. Equation 6.2 becomes

$$\underbrace{\widetilde{Y}_k(x_j, t)}_{known} = \int_0^1 \int_0^1 \underbrace{\langle Y_k | \eta, \upsilon \rangle (\eta, \upsilon, x_j, t)}_{unknown} \underbrace{\tilde{P}(\eta, x_j, t)}_{known} \underbrace{\overline{P}(\upsilon, x_j, t)}_{known} d\eta d\upsilon, \tag{6.3}$$

where $\widetilde{Y}_k(x_j,t)$ is obtained from mean species transport equations. Thus, the only unknowns are the conditional averages, which are calculated via the inversion process. Once the conditional averages are determined, the conditional chemical source terms are found in the chemistry look-up tables. Further detail on the chemistry tabulation is given in Section 6.1.3. Finally, the unconditional chemical source term is obtained using

$$\overline{\dot{\omega}_k}(x_j,t) = \int_0^1 \int_0^1 \langle \dot{\omega}_k|\eta,\upsilon\rangle(\eta,\upsilon,x_j,t)\overline{P}(\eta,\upsilon,x_j,t)\,d\eta d\upsilon. \tag{6.4}$$

6.1.2 Inversion method

The main challenge in the CSE combustion model resides in the inversion of the Fredholm integral equation, as shown by Eq. 6.3. For this process, the CFD domain is divided into CSE ensembles, consisting of a sub-set of CFD cells. In each ensemble, the conditional averages are assumed to be homogeneous. This assumption is required for the inversion process as it removes the spatial dependency of the conditional averages within an ensemble. It is justified by the fact that conditional averages have been shown to vary less in space than their unconditional counterparts [24]. Thus, Eq. 6.3 can be rewritten for a given ensemble as

$$\widetilde{Y}_k(x_j,t) = \int_0^1 \int_0^1 \langle Y_k|\eta,\upsilon\rangle\widetilde{P}(\eta,x_j,t)\overline{P}(\upsilon,x_j,t)\,d\eta d\upsilon \tag{6.5}$$

and the same inversion process outlined in Chapter 3 is applied.

The CSE ensembles are selected using *a priori* knowledge of the characteristics of the flame. For premixed flames [45, 46], one ensemble has been defined covering the entire computational domain. In non-premixed combustion, the conditional averages have a weak radial dependence [24] and the ensembles are taken as a set of planes in the axial direction [42]. Recently, a more sophisticated method has been investigated to create ensembles for complex geometries based on a Morton order algorithm [113]. In the current study, the ensembles are defined following the method used for non-premixed CSE from Chapter 3.

6.1.3 Chemistry tabulation

In the present study, detailed kinetics are included using the GRI-Mech 2.11 mechanism [81] for methane/air combustion with 49 species and 277 reactions. In principle, CSE can determine the conditional averages for all species in a given mechanism and does not require

any chemistry tabulation. However, for computational savings, tabulated chemistry has always been implemented in past CSE studies [42, 53]. Computational time and storage are even more critical in LES. In recent LES-CMC calculations, tabulated chemistry has also been implemented to determine the conditional averages [114]. In the current study, the chemistry is tabulated using the TGLDM approach [105] prior to the simulations. Other chemistry tabulation techniques could have been considered, but have not been investigated in the present work.

Species mass fractions and reaction rates are tabulated as functions of the mixture fraction, η and the oxidizer split, υ. The initial fuel mass fraction and the composition of the oxidizer are specified by η and υ, respectively. In TGLDM, the trajectories are then determined by solving the governing Ordinary Differential Equations (ODEs) using a stiff ODE system solver for 0-D ignition trajectories. The trajectories end when the equilibrium composition of the mixture is reached. The effect of strain rate on the reaction rates is not considered in the current TGLDM tables. Differential diffusion is also neglected as it is shown to have a minimal impact on the simulation results [29]. Differential diffusion has also been omitted in previous LES of the same DJHC flames [9]. The experimental studies do not report any preferential diffusion [54, 55]. The mixture fraction sample space is discretized into 50 different values ranging from 0.003 to 0.99, with a greater concentration of points around the stoichiometric mixture fraction of 0.02 [9, 54]. The oxidizer split is discretized into 10 different values ranging from 0 to 1. Two species mass fractions are selected to characterize the chemical activity. In the present study, the mass fraction of Y_{CO_2} and Y_{H_2O} are selected due to their long formation times [43] and have been shown to work well in previous CSE studies [43, 50, 53]. By selecting these two mass fractions as tabulation coordinates, the trajectories collapse towards a single trajectory as the table approaches equilibrium. However, away from equilibrium the tables remain a strong function of Y_{H_2O} and Y_{CO_2}, as can be seen in Fig. 1 of [50]. Thus, the TGLDM tables are created as functions of four variables; η, υ, Y_{CO_2} and Y_{H_2O}

6.1.4 Experimental conditions

The axisymmetric burner experimentally studied by Oldenhof et al. [54, 55] is selected for the current study. The experimental setup consists of a primary burner with a diameter of 4.5 mm surrounded by a hot coflow, 82.8 mm in diameter, provided by a partially premixed secondary burner. The main burner uses Dutch natural gas, while the secondary burner consists of a ring of premixed flames with additional air injected on both sides, resulting in a hot coflow with low oxygen concentrations. Non-uniform temperature and species profiles are found in the coflow due to the nature of the secondary burner. The

burner is also open to atmospheric cold air (third stream). A database for this burner configuration consisting of different coflow temperatures, oxygen mass fractions and jet Reynolds numbers can be found in [54, 55]. In the current study, two different burner configurations are investigated corresponding to two different Reynolds numbers. These two flames are selected to determine if the LES-CSE simulations can correctly predict the change in flame characteristics and lift-off height that occurs with a change in Reynolds number. The inlet boundary conditions for these two cases are given in Table 6.1.

Table 6.1: Experimental conditions selected for the present simulations (Re_d is the jet Reynolds number, T^c_{CO-max} the maximum coflow temperature and $Y^c_{O_2}$ the calculated mass flux weighted mean mass fraction in the coflow)

Simulation Case	Experimental label [54, 55]	Re_d	T^c_{CO-max} [K]	$Y^c_{O_2}$
DJHC-I 4100	DJHC-I	4100	1540	0.076
DJHC-I 8800	DJHC-I	8800	1540	0.076

Velocity and temperature measurements are available at different heights from the fuel burner exit, 3, 15, 30, 60, 90, 120 and 150 mm. Note that no temperature measurement is given at 15 mm and 150 mm for the DJHC-1 8800 flame. In addition for this flame, few velocity measurements are available at 15 mm and none at 150 mm. Thus, for the DHJC-I 8800 case, in Section 6.3, the comparison between the numerical predictions and the experiments will focus on the axial locations of 30, 60, 90 and 120 mm. Mean velocities and Reynolds stresses were obtained by Laser Doppler Anemometry (LDA). Temperatures were measured using Coherent Anti-Stokes Raman Spectroscopy (CARS) with estimated inaccuracy of 20 K [55]. The relative uncertainty in the fuel temperature is given at $\pm$ 5% and the uncertainty in the Reynolds numbers is estimated at $\pm$ 200 for Re = 4100 and $\pm$ 300 for Re = 8800. The uncertainty in oxygen measurements is specified at $\pm$ 0.2%. No uncertainty is provided for the velocity measurements.

6.2 Computational details

A schematic of the computational domain is shown in Fig. 6.1. The computational domain is a cylindrical wedge with a radius of 80 mm. As suggested by De et al. [29], the computational domain is extended past the coflow to allow for entrainment of ambient air. In the axial direction the computational domain begins 3 mm downstream of the jet

exit, being the first axial position with experimental data available for the inlet conditions, and extends an additional 225 mm. Due to symmetry, a two dimensional simulation is performed using a wedge angle of 5°. The current grid, consisting of 31250 cells, is non-uniform with a higher density of cells near the nozzle and close to the centreline. The current results have been shown to be grid independent.

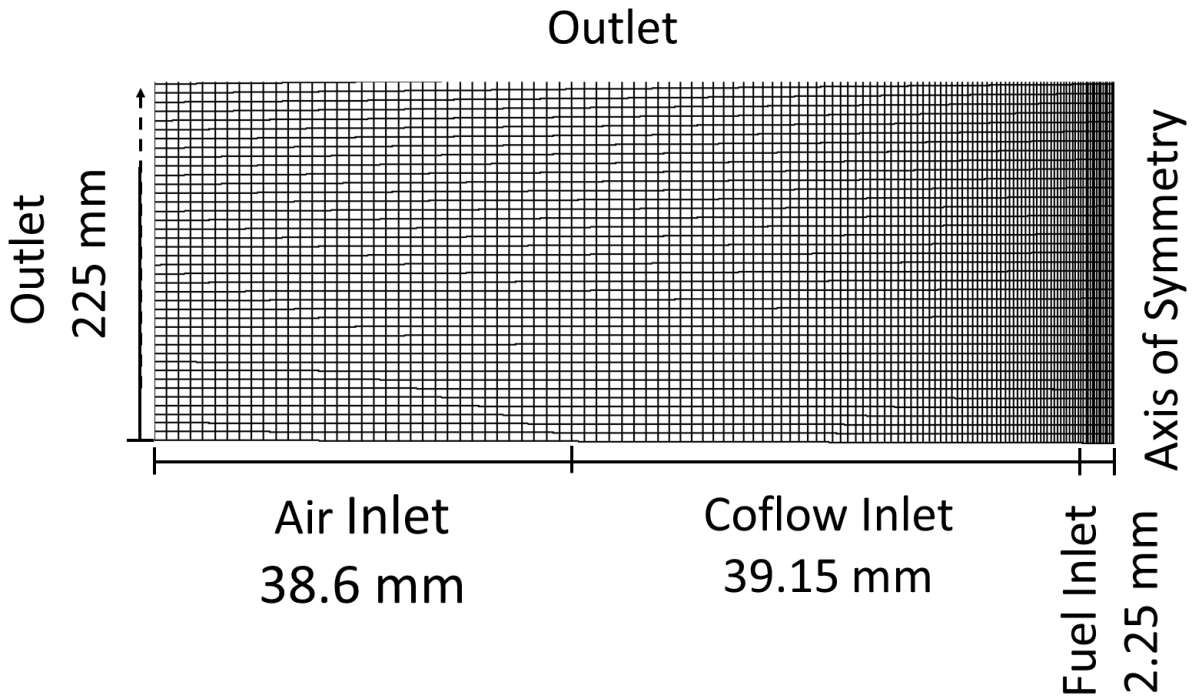

Figure 6.1: Schematic of the computational domain

The RANS flow and continuity equations are solved using OpenFOAM [86] with a finite volume low Mach number pressure based solver. Radiation heat loss due to the main combustion product species, H_2O and CO_2, is included using an optically thin radiation model. In previous simulations of the DJHC flames, the effect of radiation is found to be small [29]. Thus, it is assumed that radiation will have a negligible effect on the conditional reaction rates and non-strained adiabatic TGLDM manifolds are used.

The boundary conditions for velocity, temperature, $\widetilde{Y}_{O2}$, turbulent kinetic energy and turbulent energy dissipation, are determined from the experimental data taken 3 mm above

the burner. The main fuel burner is modelled as 85% CH_4 and 15% N_2 by volume, has the same calorific value as Dutch natural gas [29] and corresponds to Fuel I, from the experiments [55]. The oxidizer inlet profiles must be approximated as there is no experimental oxygen mass fraction data for radial distances smaller than 7 mm. In the present study, the coflow boundary condition for W is estimated using the method suggested by Kulkarni and Polifke [9]. By assuming that the oxygen concentration and temperature are correlated, W can be calculated using

$$W(x) = \frac{T^c_{co_{max}} - T(x)}{T^c_{co_{max}} - T_{air}}, \tag{6.6}$$

where $T^c_{co_{max}}$ is the maximum temperature in the coflow and $T(x)$ is the local temperature. This approximation is only used to calculate the W boundary conditions for radial distances, r, equal to or larger than 2.25 mm and is independent definition of W presented in Eq. 6.6. For $r \leq 2.25$ mm, W is set to 0 and Z set to 1. The mass fractions for the coflow are calculated assuming equilibrium combustion, with the local elemental oxygen mass fraction estimated using W calculated from Eq. 6.6. It should be noted that Eq. 6.6 neglects the heat transfer that may occur through the burner walls. If this heat transfer is significant near the inner wall, Eq. 6.6 would overpredict the O_2 concentration, which may lead to an underprediction in the lift-off height. However, without detailed experimental data estimating the heat transfer through the burner walls, the lift-off height sensitivity to this assumption cannot be determined.

The CFD code provides the mean mixture fractions, Z and W, their variance, and the unconditional Favre-averaged mass fractions of CO_2 and H_2O to CSE. The CSE routine then calculates the conditional averages for $\langle Y_{CO_2}|\eta, \upsilon\rangle$ and $\langle Y_{H_2O}|\eta, \upsilon\rangle$ by inverting Eq. 6.3. Once $\langle Y_{CO_2}|\eta, \rangle$ and $\langle Y_{H_2O}|\eta, \upsilon\rangle$ are found, the conditional chemical source terms are determined from the TGLDM tables. The unconditional chemical source terms are then obtained via Eq. 6.4 and passed back to the CFD code as a chemical source term in the species transport equation. The unconditional Favre-averaged mass fractions can then be calculated and the process repeats until steady-state is reached. The CSE routine also requires a minimum number of CFD cells, defined by the size of $\langle Y_k|\eta, \upsilon\rangle$, for the inversion process, the number of Z bins $\times$ number of W bins. If fewer CFD cells are present, the inversion problem becomes rank-deficient and a different regularization method is required. For the current simulations a minimum of 500 CFD cells are required in each ensemble for the inversion process. In the current CSE, a progress variable is not included as it would increase the dimension of the conditional averages. For example, if ten values were used for the progress variable 5000 conditional averages would be required. This would require each CSE ensemble to contain a minimum of 5000 CFD cells which is not feasible for the current RANS simulation.

6.3 Results

The present results include radial profiles for velocity, turbulent kinetic energy, temperature and lift-off heights for two flames, DJHC-I 4100 and DJHC-I 8800. The predictions are compared with the experimental data and previous numerical simulations. Further, the impact of CSE ensemble selection is examined.

6.3.1 Velocity and turbulent kinetic energy

To ensure that the flow field is properly modelled two turbulence models, the standard $k-\epsilon$ [115] and realizable $k-\epsilon$ [116] are considered. For the DJHC-I 4100 flame both the $k-\epsilon$ and realizable $k-\epsilon$ turbulence models are found to predict similar velocity profiles with a slight advantage to the standard $k-\epsilon$ turbulent model. The radial velocity profiles using the $k-\epsilon$ turbulence model at various axial locations are shown in Fig. 6.2. As seen in Fig. 6.2, the CSE velocity profiles are in very good agreement with the experimental data. For the DJHC-I 8800 flame the realizable $k-\epsilon$ turbulence model is found to better predict the velocity profile, consistent with the observations of De et al. [29]. The velocity profiles for the DJHC-I 8800 flame are also in good agreement with experimental data and are shown in Fig. 6.3.

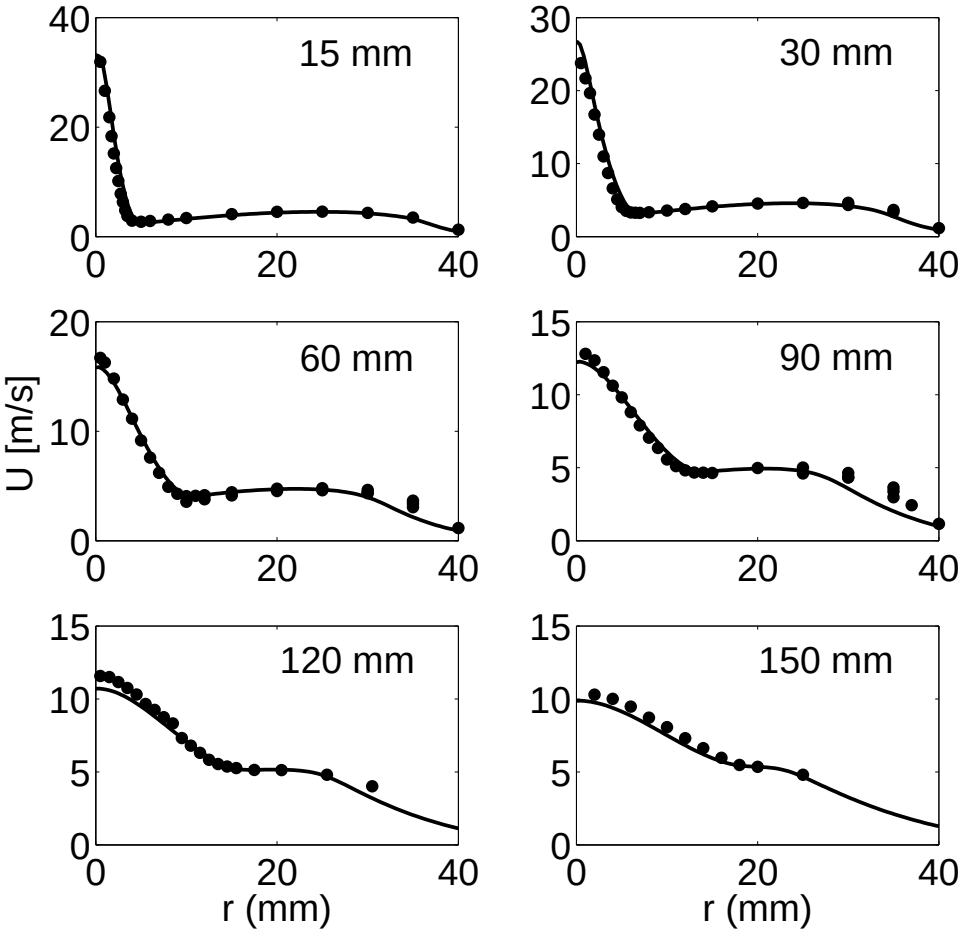

Figure 6.2: CSE mean axial velocity profiles in the radial direction (solid lines) compared to experimental data [54, 55] (symbols) at various axial locations for the DJHC-I 4100 flame

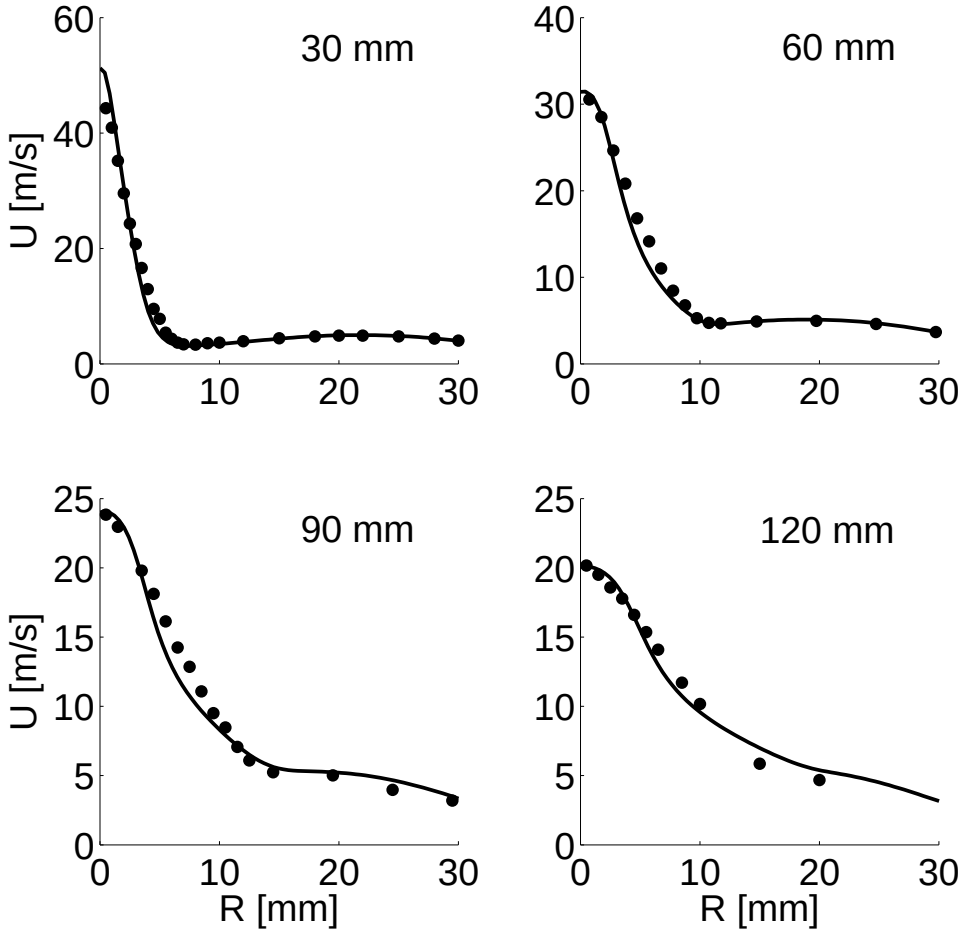

Figure 6.3: CSE mean axial velocity profiles in the radial direction (solid lines) compared to experimental data [54, 55] (symbols) at various axial locations for the DJHC-I 8800 flame

The turbulent kinetic profiles for the two flames are also examined and are shown in Figs. 6.4 and 6.5. A slight underprediction of the turbulent kinetic energy centreline profiles is observed in the CSE results for both flames. Downstream of the nozzle past 30 mm the radial turbulent kinetic energy profiles closely follow the experimental data.

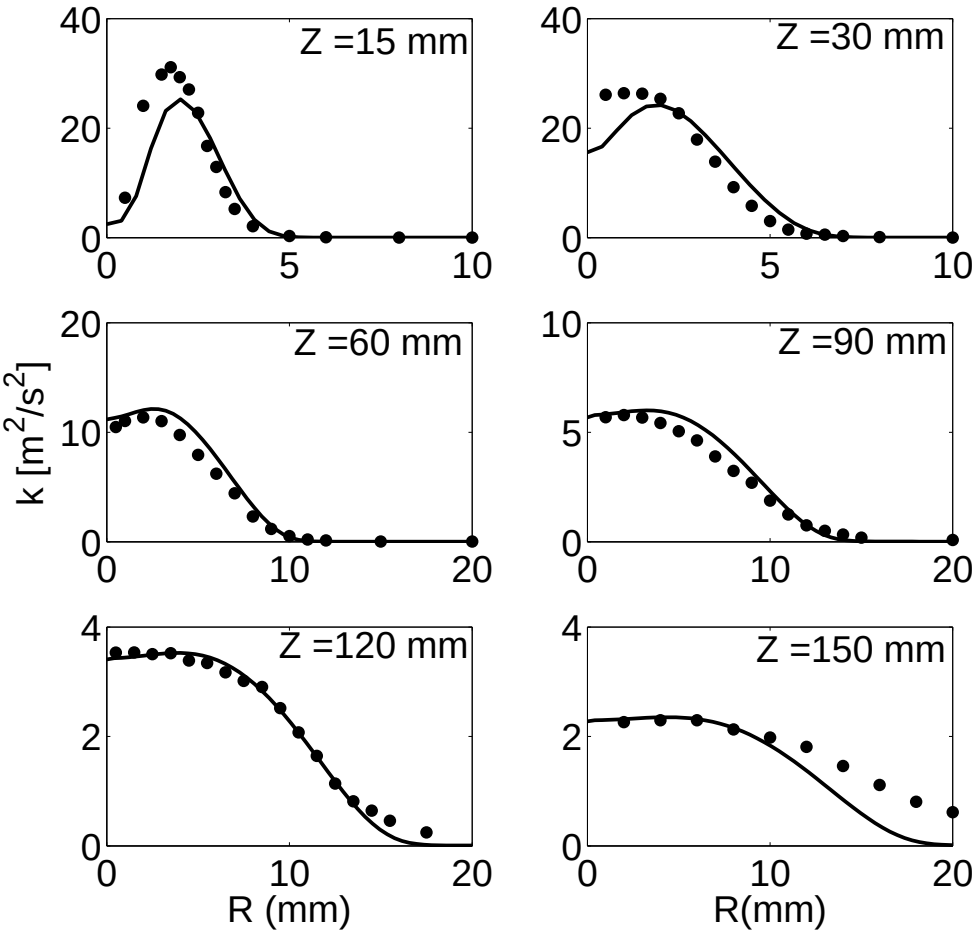

Figure 6.4: CSE mean turbulent kinetic profiles in the radial direction (solid lines) compared to experimental data [54, 55] (symbols) at various axial locations for the DJHC-I 4100 flame

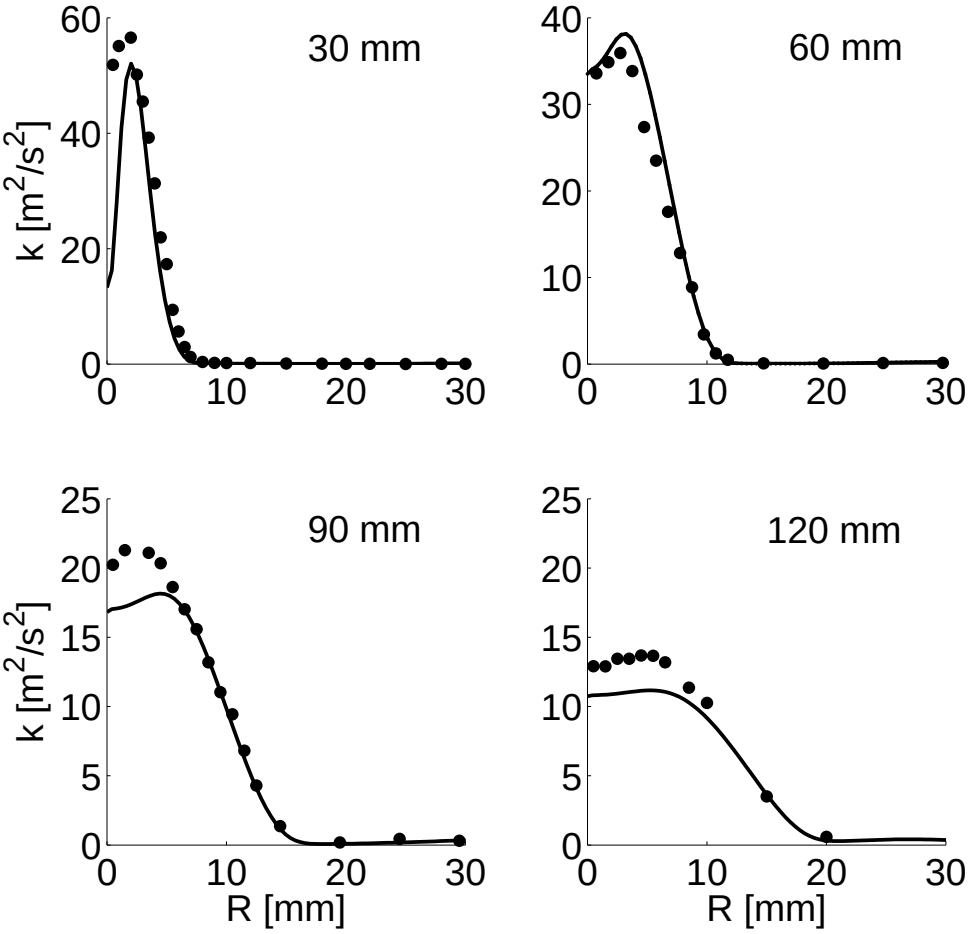

Figure 6.5: CSE mean turbulent kinetic profiles in the radial direction (solid lines) compared to experimental data [54, 55] (symbols) at various axial locations for the DJHC-I 8800 flame

6.3.2 Temperature

The radial temperature profiles for the DJHC-I 4100 flame are shown in Fig. 6.6 for four axial locations and compared with the experimental data [54, 55], standard EDC [29] and LES-stochastic fields [9] results. Close to the nozzle at 30 mm, the CSE results match the experimental data and previous numerical simulations closely. This location is upstream of the lift-off height. Thus, the combustion model selected is not expected to have a significant

impact on the calculated temperature profiles. Farther downstream, at 60 mm, the CSE temperature profile is very close to the experimental data. Only a slight overprediction on the order of 10% is seen 10 mm from the centreline, which is similar to the results shown in the LES-stochastic fields [9]. For comparison, the standard EDC model overestimates the temperature at this location by approximately 25%. Past 10 mm, when compared to previous simulations, the CSE temperatures are in better agreement with the experimental data. Similar trends can also be seen at 90 and 120 mm downstream of the nozzle: the CSE and LES-stochastic fields overpredict the peak temperature by less than 10% and for radial distances larger than 15 mm, the CSE temperature profiles are in excellent agreement with the experimental data. For comparison, previous RANS-EDC overpredict the peak temperature by approximately 20%-25%. The improvements seen in the CSE results as compared to the EDC model, can be attributed to the inclusion of a second mixture fraction. The differences between the CSE predictions and the stochastic fields model may be due to different mesh geometries and differences in the model formulation.

The predicted radial CSE temperatures are presented in Fig. 6.7 at the same previous four axial locations for DJHC-I 8800. Note that only the experimental data [54, 55] and previous LES [9] are available for this flame. At 30 mm downstream from the nozzle, the CSE temperatures are in close agreement with the experimental values and comparable to the LES results [9]. Farther downstream at 60 and 90 mm, CSE produces temperatures that are higher than those seen in the experiments from the centreline to approximately 15 mm. The peak temperature is overpredicted by approximately 10%. The CSE results are very close to the LES predictions between the centreline and approximately 15 mm in the radial direction. In the second part of the flame, the predicted temperatures are in very good agreement with the experimental profiles and CSE performs better than the LES-stochastic fields. At 120 mm, the temperature overprediction seen at 60 and 90 mm is accentuated and for radial distances larger than 15 mm, the temperatures remain overpredicted to a smaller extent. For this last location, the LES results are closer to the experiments for radial locations smaller than 15 mm, but do not agree as well in the second part of the flame. The CSE temperature overprediction is attributed to inaccurate modelling of the entrainment between the ambient air and coflow in the current RANS.

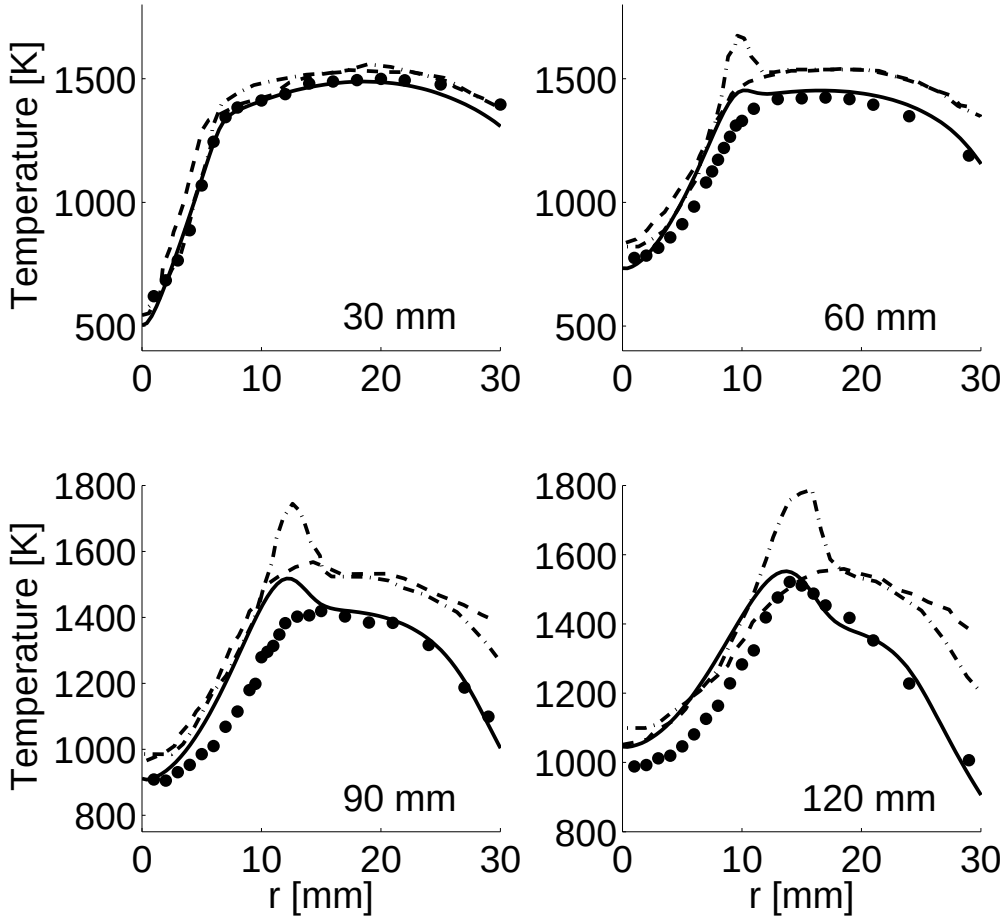

Figure 6.6: CSE radial temperature profiles (solid lines) compared to previous numerical results, standard EDC [29] (dot dashed line) and stochastic fields combustion model [9] (dashed line), and experimental data [54, 55] (symbols) at various axial locations for the DJHC-I 4100 flame

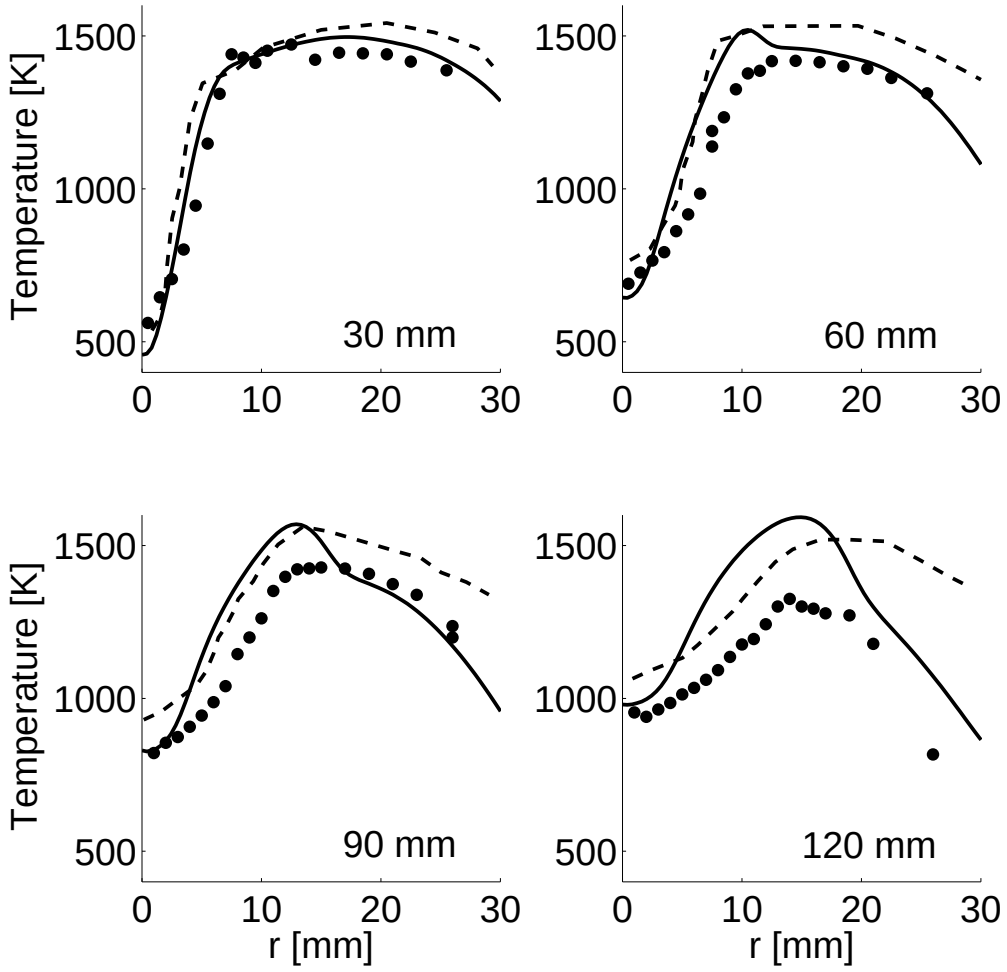

Figure 6.7: CSE radial temperature profiles (solid lines) compared to previous numerical results, stochastic fields combustion model [9] (dashed line), and experimental data [54, 55] (symbols) at various axial locations for the DJHC-I 8800 flame

6.3.3 Lift-off height

In the experiments [54, 55], the lift-off height is determined using the probability of encountering a flame pocket, defined as a location containing a OH mass fraction of 10^{-3}. The same criterion is applied to the LES results [9] and a good agreement is found between LES and experiments. However, this method needs instantaneous values and is not applicable to RANS simulations. In the present study, a different criterion is applied, inspired from the work of De et al. [29]: the mean mass fractions of OH, $\widetilde{Y}_{OH}$, for cells with mean mixture fractions in the range $0.065 \leq \widetilde{Z} \leq 0.075$ are plotted as a function of the axial distance for the two flames. Other mixture fraction ranges are expected to produce different predictions of lift-off height. However, without being able to apply the experimental criterion, only approximate values and general trends can be obtained. The lift-off height corresponds to the axial distance when the mean OH mass fraction reaches 10^{-3}. This method still provides an indication of the capability of CSE to accurately predict the lift-off height. For the DJHC-I 4100 and DJHC-I 8800 flames, the CSE lift-off height is found to be 55.5 mm and 46 mm, respectively. With a different criterion, defined based on the probability of finding a flame pocket at a given axial location, the experimental lift-off height is 80 mm for DJHC-I 4100 and 78 mm for DJHC-I 8800. RANS-CSE simulations correctly predict a lower lift-off height for the DJHC-I 8800 flame, due to increased entrainment of the surrounding coflow, in agreement with the experimental observations. However, the predicted lift-off height appears to be underpredicted compared to the experimental values. A possible explanation for the observed underprediction is that a measure of small scale straining is not included in the current CSE formulation. Thus, the effect of strain on autoignition and local extinction cannot be captured. This problem could be avoided by including an additional dimension to the model to account for small scale straining. For further improvement and direct comparison with the experiments, CSE needs to be implemented in LES.

6.3.4 Conditional mass fractions

In the current CSE method, the conditional mass fractions are used to determine the conditional reaction rates. In the present study, conditional profiles are calculated for $\langle Y_{CO_2}|\eta,\upsilon\rangle$ and $\langle Y_{H_2O}|\eta,\upsilon\rangle$ for the 12 CSE ensembles. There is no experimental data available for the conditional averages. For illustration, the conditional mass fraction of CO_2 for the DJHC-I 8800 flame is presented in Figs. 6.8a) and b) at 90 mm and 225 mm, respectively. As can be seen in Fig. 6.8a), $\langle Y_{CO_2}|\eta,\upsilon\rangle$ reaches a maximum at $Z = 0.0237$ and $W = 0.11$. For comparison, at 225 mm (Fig. 6.8b)), corresponding to the last

ensemble, the maximum value of $\langle Y_{H_2O}|\eta,\upsilon\rangle$ occurs at $Z = 0.062$ and $W = 0.44$. This demonstrates that as ambient air is entrained, the peak of $\langle Y_{CO_2}|\eta,\upsilon\rangle$ shifts towards the stoichiometric mass fraction in pure air.

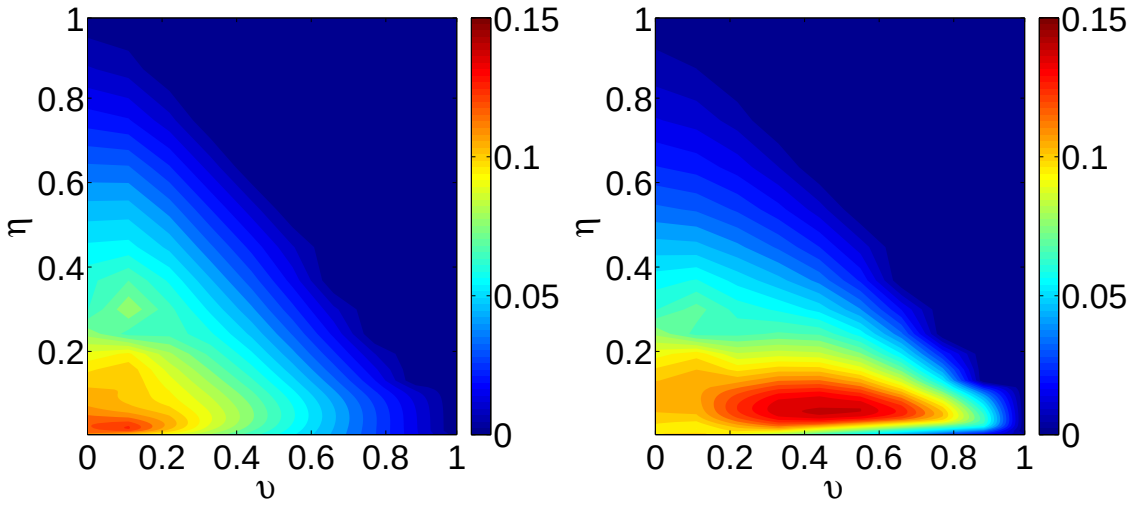

(a) 90 mm (b) 225 mm

Figure 6.8: Conditional mass fraction of CO_2 at two axial positions, 90 mm and 225 mm

6.3.5 Sensitivity to CSE ensemble selection

The non-premixed CSE simulations from Chapter 3 have shown that the predictions obtained using CSE can be sensitive to the size and location of the ensembles used for the inversion process. In the current study, two simulations using 8 and 12 CSE domains have been performed to determine the sensitivity of the CSE predictions to the ensemble selection. Both the temperature and lift-off height are used as indicators to ensure the CSE ensembles selected has minimal impact on the solutions. The maximum temperature difference between the two simulations is approximately 10 K, or less than 1%. Thus, it can be concluded that the temperature profiles are independent of the CSE ensembles selected in the present study. Figure 6.9 presents the predicted $\widetilde{Y}_{OH}$ profile for the DJHC-I 4100 flame using 8 and 12 CSE ensembles. For illustration, only the profiles for the DJHC-I 4100 flame are shown, but similar conclusions are found for the DJHC-I 8800 flame. It can be seen that the $\widetilde{Y}_{OH}$ predictions are very similar until approximately 50 mm in the axial direction. A small difference is seen between the two simulations at 30 mm but the

shape remains almost identical. As shown in Fig. 6.9, the predicted lift-off height varies with the number of CSE ensembles. However, the difference in the predicted lift-off height is approximately 2 mm which is less than the difference seen by changing the turbulence model. The number of CSE ensembles may be further increased to refine the lift-off height predictions. However, there is a limit to how many CSE ensembles can be used, as each CSE ensemble in the current simulations must contain a minimum of 500 CFD cells for the inversion process to remain accurate. Further, as shown in Chapter 3 the computational time required increases as the number of CSE ensembles gets larger. As the temperature is independent of the CSE ensembles selected and difference in the predicted lift-off height is small, less than 4%, the present results are considered independent of further CSE ensemble increase.

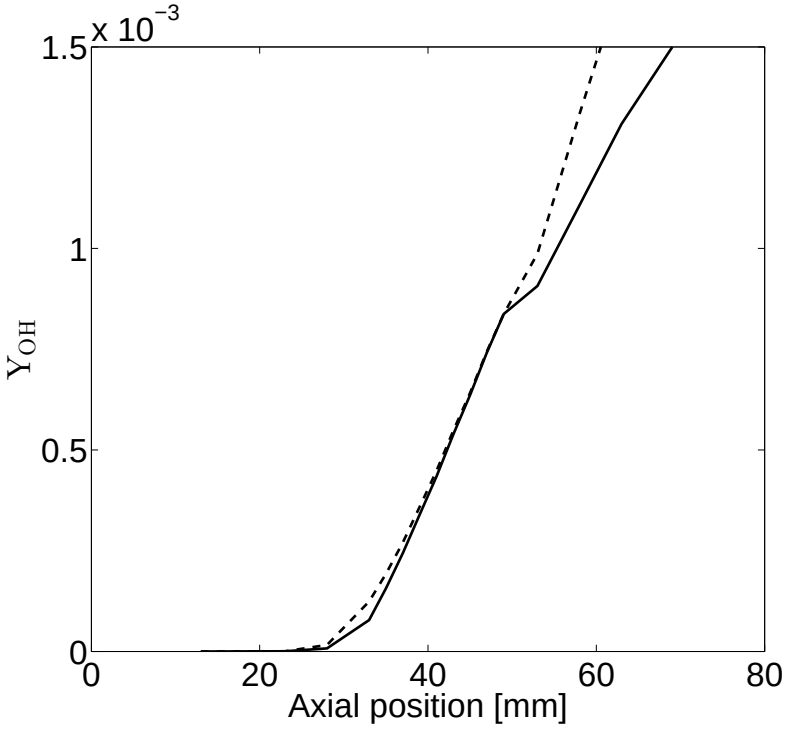

Figure 6.9: Sensitivity to CSE ensemble selection: CSE predicted $\widetilde{Y}_{OH}$ profiles as a function of axial height using 8 (dashed line) and 12 (solid line) CSE ensembles for the DJHC-I 4100 flame

6.4 Summary

For the first time, CSE was implemented to model the DJHC burner by introducing a second mixture fraction to account for the variation in the coflow. Two different flames were considered corresponding to DJHC-I 4100 and DJHC-I 8800.

For the DJHC-I 4100 flame the standard $k-\epsilon$ turbulence model was found to accurately predict the radial velocity profiles. The realizable $k-\epsilon$ turbulence model produced better velocity profiles for the DJHC-I 8800 flame, consistent with the observations of De et al. [29]. In both flames, the predicted turbulent kinetic energy was in good agreement with the experimental data.

For the DJHC-I 4100 flame, the radial CSE temperature predictions were in close agreement with the experimental data and CSE performed better compared to RANS-EDC [29] and LES-stochastic fields [9]. For the DJHC-I 8800 flame, at 30, 60 and 90 mm downstream of the nozzle, in the first half of the flame near the centreline, the radial CSE temperature profiles were slightly larger than the experimental values, but of comparable quality compared to the LES-stochastic field results [9]. In the second half of the flame, the CSE predictions were in close agreement with the experimental results. The CSE temperature predictions were not as good for the last axial location, in particular for radial distances smaller than 18 mm. The discrepancies in the temperature predictions were attributed to some inaccuracies in predicting the entrainment of the ambient air and coflow due to RANS limitations.

CSE correctly predicted the trend of lift-off height decreasing with increasing Reynolds number. Although the lift-off height criterion is different, the predicted lift-off height appeared underpredicted compared to the experiments.

Two different numbers of CSE ensemble were tested. The temperatures were found to be independent of the CSE ensembles selected and the difference in the predicted lift-off height was less than 4%. Thus, the results are considered to be independent of further CSE ensemble increase and demonstrate that RANS-CSE using two mixture fractions as conditioning variables, can capture the main properties of MILD combustion for the DJHC flame.

Chapter 7

LES-CSE applied to MILD combustion

In this chapter, the multistream CSE formulation developed in Chapter 6 is extended to the LES framework. This represents the first time a double conditioned CSE formulation is applied in LES. In Chapter 6 this model was used to simulate the Delft-Jet-in-Hot-Coflow (DJHC) burner using a RANS turbulence model, with good agreement with experimental data. Due to the transient nature of the lift-off height, the experimental definition of the lift-off height is based on the probability of finding a flame pocket at a given axial location. For the RANS simulations, only an approximation of the lift-off height could be made due to the time-averaging applied in RANS. Further, the RANS simulations were unable to predict the time-dependent ignition kernel formation mechanism seen in these flames. Thus, to accurately capture all the flame characteristics, LES is required.

The objective of the current chapter is to further explore the ability of CSE to correctly predict the flow characteristics seen in the Dutch natural gas DJHC flames. The CSE predictions are compared to available experimental data [54, 55] for the mean axial velocity, axial velocity fluctuation, temperature and lift-off height. In addition, the ability of CSE to reproduce the ignition kernel formation mechanism seen in the DJHC flames is examined. Finally, the sensitivity to the coflow inlet boundary conditions is investigated.

7.1 LES formulation for mulitstream CSE

In the present work, simulations are performed using the two mixture fraction CSE formulation for multistream combustion problems developed in Chapter 6, applied in the

LES framework. In the context of LES, the filtered conditional chemical source term is expressed in terms of conditional filtered means. Following the work of Bushe and Steiner [39], the doubly conditional filtered operation is defined as

$$\langle f(x_j,t)|\eta,\upsilon\rangle = \frac{\int_V f(x',t)\delta[\eta - Z(x',t)] \times \delta[\upsilon - W(x',t)]\ G(x_j,x')dx'}{\overline{P}(\eta,\upsilon,x_j,t)}, \tag{7.1}$$

where V is the spatial domain over which the filtering occurs, f may be any scalar of interest such as species mass fraction, temperature or chemical production, x_j is the spatial coordinate, t the time, δ the delta function and $\overline{P}(\eta,\upsilon,x_j,t)$ the subgrid joint PDF or Filtered Density Function (FDF) given by

$$\overline{P}(\eta,\upsilon,x_j,t) = \int_V \delta[\eta - Z(x',t)] \times \delta[\upsilon - W(x',t)]G(x_j,x')dx'. \tag{7.2}$$

A Favre joint FDF, $\widetilde{P}(\eta,\upsilon,x_j,t)$, can also be defined as

$$\widetilde{P}(\eta,\upsilon,x_j,t) = \frac{\langle\rho(x_j,t)|\eta,\upsilon\rangle\ \overline{P}(\eta,\upsilon,x_j,t)}{\overline{\rho}(x_j,t)}. \tag{7.3}$$

The unconditional filtered chemical source term for species k, $\overline{\dot{\omega}_k}$, is determined by integrating the conditional filtered chemical source term multiplied by the joint FDF over both mixture fraction spaces,

$$\overline{\dot{\omega}_k}(x_j,t) = \int_0^1\int_0^1 \langle\dot{\omega}_k|\eta,\upsilon\rangle(\eta,\upsilon,x_j,t)\overline{P}(\eta,\upsilon,x_j,t)\,d\eta d\upsilon. \tag{7.4}$$

Using the fact that Z and W are independent [65], the joint FDF can be rewritten as

$$\overline{P}(\eta,\upsilon,x_j,t) = \overline{P}(\eta,x_j,t)\cdot\overline{P}(\upsilon,x_j,t), \tag{7.5}$$

with a presumed β-FDF distribution to model $\overline{P}(\eta,x_j,t)$ and $\overline{P}(\upsilon,x_j,t)$ [73]. The presumed β-PDF is shown to be inaccurate in the context of premixed combustion [117, 118]. However, it provides a reasonable description of the subgrid mixture fraction distribution in LES for non-premixed combustion [119] and is commonly used for the mixture fraction FDF [120]. Without any further information of the FDF shape in the present three-stream conditions and for consistency with the RANS simulations from Chapter 6, the β presumed form is selected.

The use of ensembles is similar to what is done in LES-CMC where a coarse CMC grid is defined for the solution of the CMC equations and the flow equations are solved on the

LES grid [121]. This also introduces an inconsistency between the definition of the spatial LES filter and the coarser spatial filter assumed for the conditionally filtered averages. However, in LES-CSE, the transport equations for the main species are filtered and solved at the LES grid level. The size of each ensemble may be compared with the integral length scale for the current conditions. Further investigation is needed to assess the impact of the LES-CSE filter width on the numerical predictions.

7.2 Computational details

The three dimensional computational domain closely follows the experimental set-up and consists of a cylinder with a radius of 80 mm and extends 225 mm in the axial direction. Boundary conditions for mean velocity and temperature at the inlet are specified based on measured experimental data corresponding to the two cases shown in Table 6.1. A schematic of the computational domain is also presented in Fig. 7.1. The grid includes approximately 1.5 million cells and is non-uniform with a higher density of cells near the nozzle and close to the centreline. As a result, the filter widths range between 0.16 mm and 2.7 mm. In particular, in the flame stabilization region, the filter width is approximately 0.65 mm and 0.80 mm for the DJHC-I 4100 and DJHC-I 8800 flames, respectively. The filter width values may be compared with the turbulent length scales determined in the experiments. In the experimental investigation, the integral and Taylor length scales are evaluated at two different heights for each flame [54]. For the two flames, the integral length scale is found to vary between 2 and 5 mm and the Taylor length scales are between 1 and 3.5 mm [54]. The Kolmogorov length scale is estimated to be on the order of 10^{-4} m [54]. Thus, the filter widths remain below the experimental values for the integral length scale, smaller or on the same order as the values reported for the Taylor length scales, and sometimes close, but always larger than the Kolmogorov length scale, consistent with what would be expected in well-resolved LES. Several grids were tested by successive refinements and examination of the variations of time-averaged velocities in non-burning conditions.

The LES simulations are performed using OpenFOAM [86] with a finite volume low Mach number pressure based solver. Transport equations are solved for mass (continuity), momentum, enthalpy, the resolved mixture fraction, $\widetilde{Z}$, its Sub-Grid Scale (SGS) variance, $\widetilde{Z''^2}$, the resolved oxidizer split, $\widetilde{W}$, and its SGS variance $\widetilde{W''^2}$. The transport equations for $\widetilde{Z}$ and $\widetilde{Z''^2}$ are

$$\frac{\partial \bar{\rho}\widetilde{Z}}{\partial t} + \frac{\partial(\bar{\rho}\widetilde{u}_i\widetilde{Z})}{\partial x_i} = \frac{\partial}{\partial x_i}\left(\bar{\rho}(D + D_t)\frac{\partial \widetilde{Z}}{\partial x_i}\right) \tag{7.6}$$

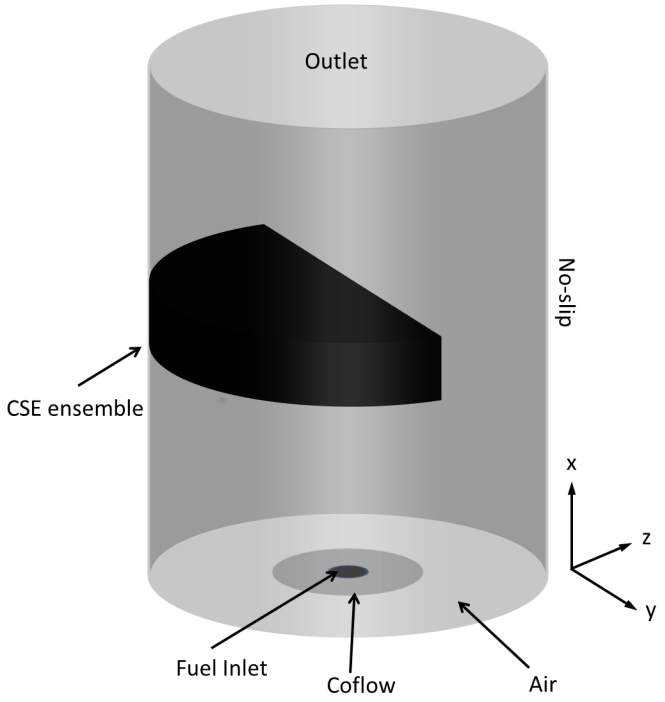

Figure 7.1: LES computational domain showing one CSE ensemble and boundary conditions

and

$$\frac{\partial(\overline{\rho}\widetilde{Z''^2})}{\partial t} + \frac{\partial\left(\overline{\rho}\widetilde{u}_i\widetilde{Z''^2}\right)}{\partial x_i} = \frac{\partial}{\partial x_i}\left(\bar{\rho}(D+D_t)\frac{\partial\widetilde{Z''^2}}{\partial x_i}\right) - 2\bar{\rho}(D+D_t)\frac{\partial\widetilde{Z}}{\partial x_i}\frac{\partial\widetilde{Z}}{\partial x_i} - \overline{\rho}\widetilde{\chi}_Z, \quad (7.7)$$

where D and D_t are the molecular and turbulent diffusivity, respectively. In the present study, differential diffusion is neglected as it has been shown to have a minimal impact on the simulation results [29]. Differential diffusion has also been neglected in a previous LES study of the DJHC burner [9].

The transport equations for $\widetilde{W}$ and $\widetilde{W''^2}$ are

$$\frac{\partial\bar{\rho}\widetilde{W}}{\partial t} + \frac{\partial(\bar{\rho}\widetilde{u}_i\widetilde{W})}{\partial x_i} = \frac{\partial}{\partial x_i}\left(\bar{\rho}(D+D_t)\frac{\partial\widetilde{W}}{\partial x_i}\right) \quad (7.8)$$

and

$$\frac{\partial(\overline{\rho}\widetilde{W''^2})}{\partial t}+\frac{\partial\left(\overline{\rho}\widetilde{u}_i\widetilde{W''^2}\right)}{\partial x_i}=\frac{\partial}{\partial x_i}\left(\bar{\rho}(D+D_t)\frac{\partial\widetilde{W''^2}}{\partial x_i}\right)-2\bar{\rho}(D+D_t)\frac{\partial\widetilde{W}}{\partial x_i}\frac{\partial\widetilde{W}}{\partial x_i}-\overline{\rho}\widetilde{\chi}_W. \quad (7.9)$$

In Eqs. 7.6-7.9, the SGS scalar fluxes are modelled by a standard gradient assumption. For example, in Eq. 7.6, $\widetilde{u_iZ}-\widetilde{u}_i\widetilde{Z}=-D_t\frac{\partial\widetilde{Z}}{\partial x_i}$. Closure of the scalar dissipation of the mixture fraction and oxidizer split is provided using spectral arguments [122] such that

$$\widetilde{\chi}_W=C_{\chi W}\frac{\widetilde{\epsilon}_{sgs}}{\widetilde{k}_{sgs}}\widetilde{W''^2}, \quad (7.10)$$

$$\widetilde{\chi}_Z=C_{\chi Z}\frac{\widetilde{\epsilon}_{sgs}}{\widetilde{k}_{sgs}}\widetilde{Z''^2}, \quad (7.11)$$

where a value of 2 is used for $C_{\chi W}$ and $C_{\chi Z}$. $\widetilde{\epsilon}_{sgs}$ is calculated internally by OpenFOAM using

$$\widetilde{\epsilon}_{sgs}=c_\epsilon\frac{\widetilde{k}_{sgs}\sqrt{\widetilde{k}_{sgs}}}{\Delta}, \quad (7.12)$$

where Δ is the filter size, calculated using the cube root volume, $\Delta=(\Delta x\Delta y\Delta z)^{\frac{1}{3}}$ with Δx, Δy, and Δz being the grid spacing in each x, y and z direction, respectively, c_ϵ is a specified constant and k_{sgs} is determined based on the SGS closure model, the constant Smagorinsky model in the present work.

In addition, transport equations for the Favre-averaged mass fraction of the major species, CH_4, O_2, H_2O, CO_2, CO, OH and H_2, are solved to allow these species to be transported by the main flowfield. Mass conservation is enforced for the Favre-averaged species mass fractions in the LES solver

$$\frac{\partial\bar{\rho}\widetilde{Y}_k}{\partial t}+\frac{\partial(\bar{\rho}\widetilde{u}_i\widetilde{Y}_k)}{\partial x_i}=\frac{\partial}{\partial x_i}\Big((D+D_t)\frac{\partial\widetilde{Y}_k}{\partial x_i}\Big)+\bar{\dot{\omega}}_k. \quad (7.13)$$

In Eq. 7.13, the SGS scalar fluxes are also modelled by a standard gradient assumption. A SGS Schmidt number of 0.7 is used.

The chemical source term for each filtered species transport equation is determined in CSE via Eq. 7.4, where $\langle\dot{\omega}_k|\eta,\upsilon\rangle$ is the conditional chemical source terms for species k,

obtained from the TGLDM tables.
The filtered enthalpy equation is also solved using

$$\frac{\partial(\overline{\rho}\widetilde{h})}{\partial t} + \frac{\partial\left(\overline{\rho}\widetilde{u}_i\widetilde{h}\right)}{\partial x_i} = \frac{\partial}{\partial x_i}\left(\bar{\rho}(\alpha+\alpha_t)\frac{\partial\widetilde{h}}{\partial x_i}\right) + \frac{D\overline{p}}{Dt} - Q, \tag{7.14}$$

where $\frac{D\overline{p}}{Dt}$ is the total derivative of the filtered pressure, α and α_t are the molecular and turbulent thermal diffusivity and Q is the radiation source term. A turbulent Prandtl number of 0.7 is used and α_t is determined using the gradient assumption. In the current study, radiation heat loss due to the main combustion product species, H_2O and CO_2, is included using an optically thin radiation model.

A first order implicit Euler method is applied to advance the transport equations in time, using a variable time step with a maximum Courant number of 0.2. A second order implicit backward differencing time scheme was also tested for the simulation applied to the DJHC-I 8800 flame. Negligible differences are found for the time averaged velocity and temperature statistics. Thus, the first order temporal scheme is kept for reduced computational cost. The convective and diffusive terms are discretized using a Normalized Variable Diagram (NVD) gamma differencing scheme [123] and a central differencing scheme, respectively. The Pressure-Implicit with Splitting of Operators (PISO) algorithm is applied for pressure-velocity coupling with Rhie-Chow interpolation.

A constant Smagorinsky model for compressible flows included in OpenFOAM is selected to close the SGS stress terms and SGS scalar fluxes with the SGS eddy viscosity, μ_{sgs}, calculated using

$$\mu_{sgs} = (C_s\ \Delta)^2|\tilde{S}|, \tag{7.15}$$

where C_s is the Smagorinsky constant and $|\tilde{S}|$ the magnitude of the filtered strain rate tensor. In the OpenFoam implementation, two constants, c_k and c_ϵ, need to be set. c_k and c_ϵ can be related to the standard C_s constant [124] found in the standard Smagorinsky model using

$$C_s = \left(\frac{c_k^3}{c_\epsilon}\right)^{\frac{1}{4}}. \tag{7.16}$$

In the current simulations a range of c_k and c_ϵ values are tested and best agreement with experimental data for the velocity field is found with $c_k = 0.02$ and $c_\epsilon = 0.202$, corresponding to $C_s = 0.079$.

The inlet boundary conditions for temperature, velocity and mass fraction of O_2 are determined based on the experimental data available 3 mm downstream of the nozzle.

Turbulence at the inlet is generated using the synthetic turbulence method of Kornev and Hassel [125] based on prescribed mean velocity profiles, the corresponding Reynolds stress tensor and integral length scales. No turbulent fluctuations for temperature, mixture fraction, oxidizer split or species mass fraction are included at the inlet. At the outlet, an OpenFoam inletOutlet boundary condition is used for the velocity which switches velocity and pressure between a fixed value and zero gradient depending on the direction of the velocity. It corresponds to zero gradient for velocity when the flow is out of the domain and a fixed value, 0.5m/s in the present setup, if there is inflow. A slip boundary condition is imposed on the side of the domain. The pressure boundary at the inlet is set to zero gradient and a fixed pressure of 1 atm is imposed at the outlet. The remaining boundary conditions are identical to those specified in Chapter 6.

In the current investigation, the W inlet boundary condition is approximated based on the temperature of the coflow. Two methods are used to calculate the temperature of the coflow based on the available experimental data. The first approach assumes that the temperature of the coflow is axisymmetric with the temperature calculated from a radial line stretching from the centreline to the edge of the coflow. The second method calculates the temperature by averaging the experimental temperature at a given radius. These two temperature profiles are then used to calculate the W inlet condition using Eq. (6.6). The difference between the two W profiles at the inlet differ by up to 30% with the largest difference occurring between 5 and 25 mm in the radial direction. A sensitivity analysis is performed to determine the effect of the hot coflow temperature on the LES-CSE predictions. The difference in predicted time-averaged temperatures between the two methods is found to be smaller than 5% across the computational domain for both DHJC flames. In the DJHC-I 4100 flame, a 10% difference in the predicted lift-off height is seen between the two methods. For the DJHC-I 8800 flame, the difference between the predicted lift-off height is much smaller differing by less than 3%. Thus, the temperature predictions do not appear to be sensitive to W inlet condition for any Reynolds number, whereas the lift-off height shows some small sensitivity. For the present simulations, the coflow temperature is calculated by averaging the experimental temperature at a given radius. It should be noted that Eq. 6.6 neglects the heat transfer that may occur through the burner walls. If this heat transfer is significant near the inner wall, Eq. 6.6 would overpredict the O_2 concentration, which may lead to an underprediction in the lift-off height. However, without detailed experimental data estimating the heat transfer through the burner walls, the lift-off height sensitivity to this assumption cannot be determined.

In the current implementation of LES-CSE, the resolved mixture fraction, $\widetilde{Z}$ and oxidizer split $\widetilde{W}$, their SGS variance and the resolved unconditional Favre averaged mass fractions of CO_2 and H_2O are first passed to the CSE routines. Based on these inputs, the conditional averages for $\langle Y_{CO_2}|\eta,\upsilon\rangle$ and $\langle Y_{H_2O}|\eta,\upsilon\rangle$ are obtained by inverting the Fredholm

integral. Using the calculated conditional averages, the conditional chemical source terms for all the species are found from the TGLDM look-up tables. Next, the unconditional chemical source terms are obtained via Eq. 7.4 and used by the CFD code as a chemical source term in the species transport equations. The transport equations for the unconditional Favre averaged resolved mass fractions are then solved and the process repeats. An analysis for the computational time required to complete a single time step has been conducted to determine the relative cost of the CSE combustion model compared to the LES code. It is found that approximately 80% of the computational time is spent by the CSE routine. Within the CSE calculations, approximately 66% of the computational time is used for the integral inversion with the remaining time spent retrieving the conditional reaction rates from the tables and determining the unconditioned reaction rates. Thus, by implementing more efficient numerical methods for the integral inversion, a significant reduction in the computational time required for LES-CSE is expected. The current CSE implementation follows what is done in the previous RANS-CSE calculations from Chapter 6. Instead of solving the transport equations for the species mass fractions, it is also possible to retrieve the conditional species mass fractions directly from the TGLDM tables without solving the transport equations for the species, except for CO_2 and H_2O. Both approaches include modelling and numerical errors, which will need to be accurately assessed in the future. The present experimental data sets do not have any measured species concentrations. Thus, predicted mean or conditional species mass fractions cannot be compared and evaluated against experimental values.

For the inversion, it is assumed that the conditional averages within a given ensemble are homogeneous and the inversion problem is discrete ill-posed. As a result, a minimum number of LES cells is required for the inversion process. The minimum number of LES cells, N_{min}, is determined by the number of bins used to discretize the conditional averages (number of η bins multiplied by number of υ bins). In the event that a CSE ensemble has fewer LES cells than N_{min} the inversion problem becomes rank-deficient and a new regularization method would be required. In the current simulations, the CSE ensembles are defined following the method used for non-premixed CSE from Chapter 3. In the previous RANS-CSE study of the same flames, a minimum of 8 CSE ensembles, defined as axial slices of the CFD domain, were needed to obtain an ensemble independent solution. For the present LES, a total of 64 CSE ensembles following the domain decomposition for parallel computation, are used to ensure an ensemble independent solution. First, the domain is divided into 32 axial slices, defined as planes perpendicular to the centreline axis. Each axial slice is further divided in half along the centreline, as shown in Fig. 7.1. In previous RANS-CSE calculations [46, 53], the predictions are shown to be sensitive to the number of CSE ensembles, but to a relatively small degree. Further investigation is needed for the most suitable choice of CSE ensemble in the context of LES.

For post-processing of the present LES-CSE results, statistics are collected over ten flow-through times (one flow-through time corresponds to the length of the computational domain divided by the bulk fuel jet velocity) after steady-state conditions are reached. This corresponds to approximately 64,000 and 60,000 time steps for the DJHC-I 4100 and DJHC-I 8800 flames, respectively. For the DJHC-I 8800 flame, data is also collected over approximately 100,000 time steps to check the sensitivity of the time-averaged values to the time period. The differences between the statistics calculated using 60,000 time steps and those computed over 100,000 time steps are found to be negligible. Thus, values are collected over ten flow-through times to save computational time. The resolved temperature and velocity fields are then time-averaged. The resolved time-averaged fluctuating quantities are calculated as $\langle u_i' u_i' \rangle = (\langle (\widetilde{u}_i)^2 \rangle - \langle \widetilde{u}_i \rangle^2)$,$\langle u_i' u_j' \rangle = \langle \widetilde{u}_i \widetilde{u}_j \rangle - \langle \widetilde{u}_i \rangle \langle \widetilde{u}_j \rangle$ where the brackets represent time averages and $\widetilde{u}_i$ is the instantaneous Favre-averaged i$^{\text{th}}$ velocity component. The temperature rms is calculated as $\langle T' \rangle = (\langle (\widetilde{T})^2 \rangle - \langle \widetilde{T} \rangle^2)^{1/2}$. In the current study, unresolved fluctuations have been neglected assuming that they have a negligible contribution to rms, as commonly done in LES [126, 127]. This assumption will need to be verified in the future. Further, following the method proposed by Veynante and Knikker [126], time-averaged statistics and time-averaged density weighted statistics (Eq. 8 in [126]) were also calculated and compared as a post-process. The differences between the two sets are found to be negligible within the flames. Thus, in the present investigation, the time-averaged statistics are assumed to be representative of the turbulent flow, mixing and temperatures fields. For consistency with the experimental data, the time-averaged LES-CSE results are extracted from the (x,z) centreplane.

In addition to the comparison of the LES filter width with the turbulent length scales included at the beginning of the current section, the present LES resolution may also be examined in terms of turbulent kinetic energy resolved. A simple criterion may be applied by calculating the amount of resolved turbulent kinetic energy, k_{res}, relative to the total kinetic energy, $k_{res} + k_{sgs}$, such as

$$R = \frac{k_{res}}{k_{sgs} + k_{res}}. \tag{7.17}$$

In Eq. 7.17, k_{res} corresponds to $\frac{1}{2}(\langle u'^2 \rangle + \langle v'^2 \rangle + \langle w'^2 \rangle)$, and k_{sgs} is retrieved directly from the LES code using the Smagorinsky model and time averaged. Pope indicates that this ratio R must be at least equal to 0.8 for well-resolved LES everywhere in the domain [128]. For the DJHC-I 4100 and 8800 flames, approximately 94% and 91% of the total turbulent kinetic energy is resolved over the entire computational domain. For illustration, the values of R are shown on the centreplane in Fig. 7.2 for the two flames selected. As can be seen in Fig. 7.2, near the centreline and in the fuel/coflow mixing layer over 80% of the turbulent kinetic energy is resolved, except for a small region close to the nozzle exit.

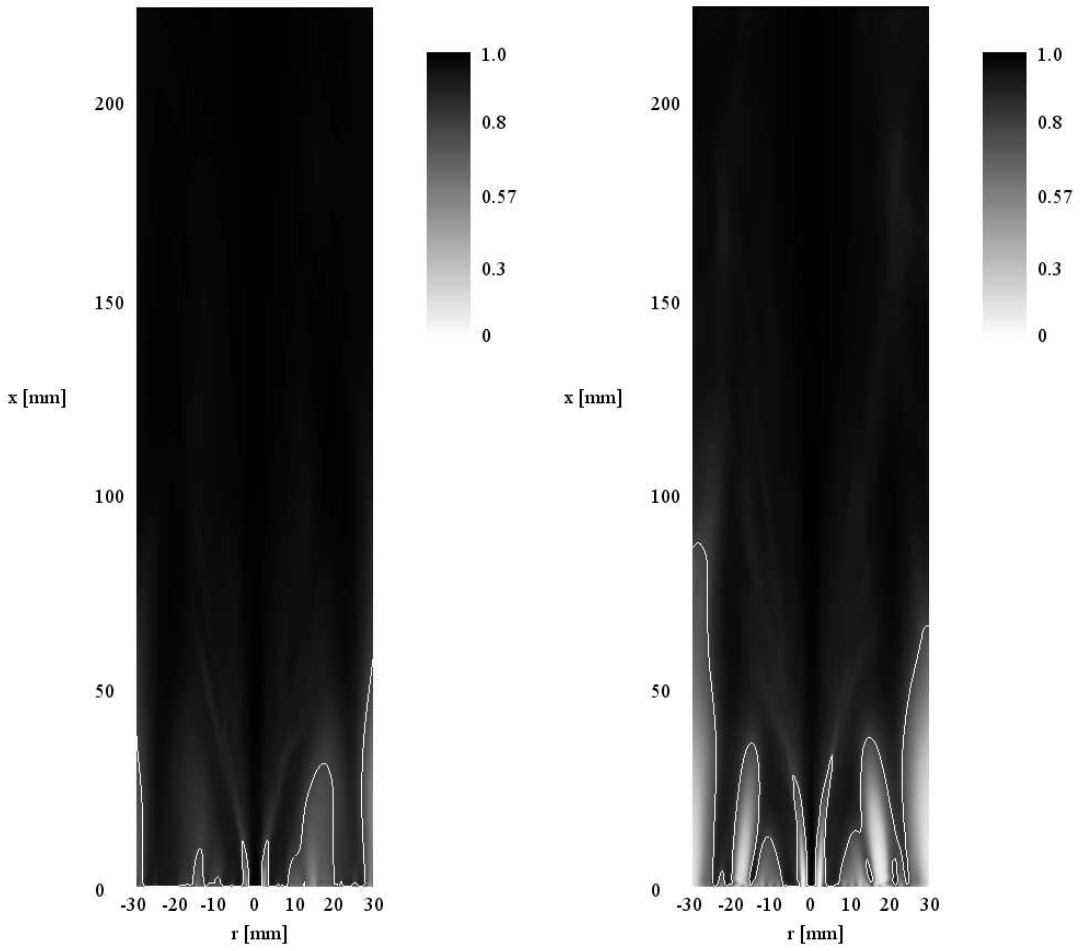

(a) DJHC-I 4100

(b) DJHC-I 8800

Figure 7.2: Resolution of the turbulent kinetic energy on the centreplane using Eq. 7.17 for the two flames under consideration. The isoline corresponding to R = 0.8 is also shown to distinguish between the well-resolved and under-resolved regions

In the shroud air and the beginning of the coflow less than 80% of the turbulent kinetic energy is resolved, due to the very low turbulence levels at these locations. The kinetic energy ratio, R, as shown in Fig. 7.2, is similar to what is displayed in Fig. 4 of [63] for the same DJHC flames.

7.3 Results

7.3.1 Turbulent flow field statistics

In the absence of detailed experimental measurements for Z, W or any species concentrations, the accuracy of the predicted turbulent mixing field cannot be assessed directly. However, the comparison of the turbulent flow field quantities with available experimental data may be used as an indicator to determine if turbulent mixing is properly captured in the present LES. The radial profiles of time-averaged resolved axial velocity, $\langle U \rangle$, are shown in Fig. 7.3 for the DJHC-I 4100 flame and Fig. 7.4 for the DJHC-I 8800 flame, at different axial locations across the computational domain, and compared with available experimental data [54, 55].

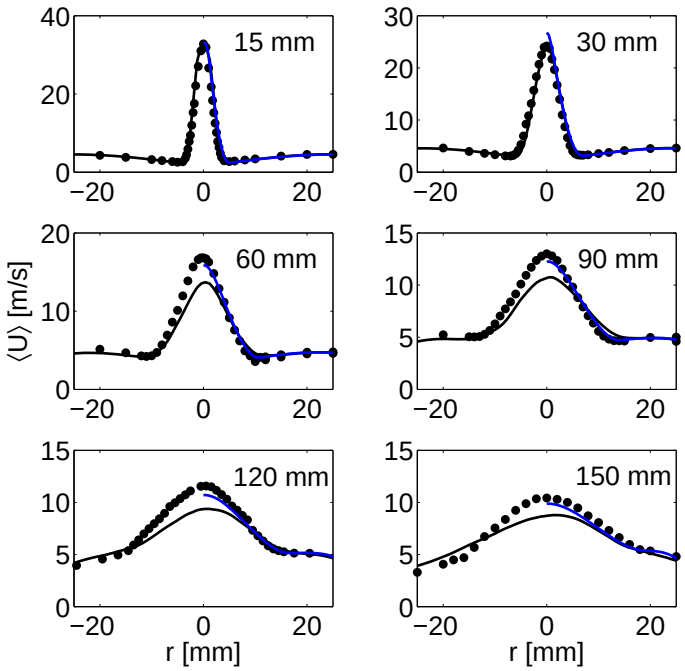

Figure 7.3: LES-CSE time-averaged resolved axial velocity profiles in the radial direction (solid line) compared to RANS-CSE numerical predictions (blue line) and compared to experimental data [54, 55] (symbols) at various axial locations for the DJHC-I 4100 flame

As can be seen in Fig. 7.3, for axial locations close to the nozzle, 15 and 30 mm, the predicted velocity profiles are in excellent agreement with the experimental data. Farther downstream, past 30 mm, the LES time-averaged axial velocities remain close to the experimental values, but near the centreline, the axial velocity is underpredicted by between 16% and 19% depending on the axial location.

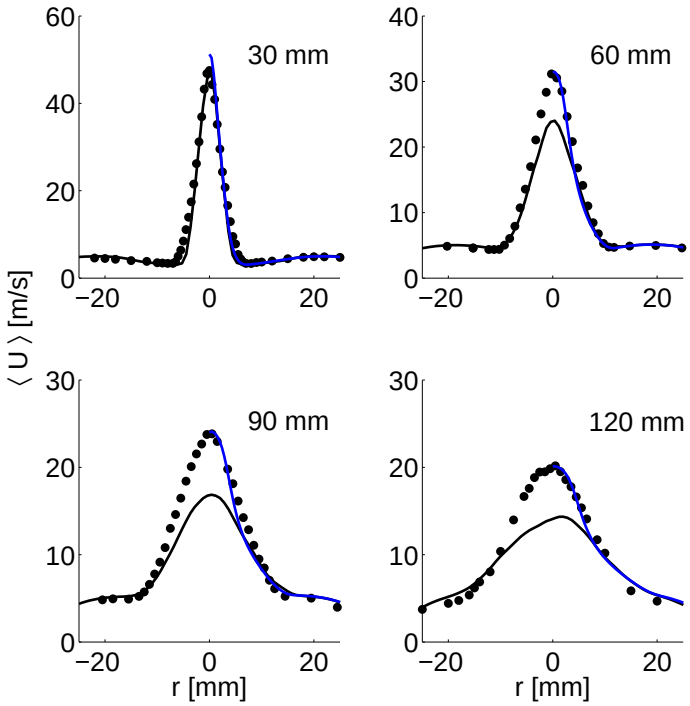

Figure 7.4: LES-CSE time-averaged resolved axial velocity profiles in the radial direction (solid line) compared to RANS-CSE numerical predictions (blue line) and compared to experimental data [54, 55] (symbols) at various axial locations for the DJHC-I 8800 flame

For the DJHC-I 8800 flame, as displayed in Fig. 7.4, similar trends can be seen. Close to the nozzle, at 30 mm, the time-averaged resolved axial velocity is well predicted, within 4% of the experimental data. Farther downstream, at 60, 90 and 120 mm, a lower centreline velocity is seen in comparison with the experimental values. The underprediction of the centreline velocity ranges from 30% at 90 mm to 40% at 120 mm. The discrepancies observed in the predicted axial velocity can be explained by inaccuracies in the modelled

entrainment of the hot coflow with the fuel jet. It should also be noted that for the DJHC-I 4100 flame, the axial locations of 15 and 30 mm are clearly below the lift-off height and for the DJHC-I 8800 flame, the lift-off height is approximately 80 mm. Further discussion on the lift-off height is included in Section 7.3.3. Thus, flow field discrepancies at axial locations below the lift-off height may be mostly attributed to the modelled turbulent mixing even if some ignition kernels can occur below the lift-off height. At positions inside the burning region, additional sources of discrepancies are possible and would come from the description of the turbulence-chemistry interactions and the chemical kinetics. In the present LES implementation, the constant Smagorinsky SGS model and turbulence inlet conditions for fuel and coflow are identified as potentially having the largest impact on the modelled turbulent flow and mixing fields. A sensitivity analysis of the Smagorinsky constant did not show any significant improvement in the predictions. In a previously published LES study for the same flames including different PDF models, negligible differences are noticed for the velocity and temperature predictions using either a dynamic Smagorinsky model or a dynamic kinetic energy transport for a given mesh [63].

In the context of LES-CSE, a dynamic Smagorinsky may still improve the predictions and will be investigated in the future. As described in Section 7.2, inlet turbulence is set using synthetic turbulence. Close to the nozzle, the time-averaged axial velocity is well-predicted in comparison to the experimental data, as shown in Figs. 7.3 and 7.4. However, inaccuracies may be present for the radial velocity components and fluctuating components which are not visible directly in the axial velocity predictions and may have an impact for the turbulent flow field farther downstream. These quantities are examined to refine the assessment of the present LES predictions.

Also shown in Figs. 7.3 and 7.4, are the RANS predictions previously obtained in Chapter 6. In comparison to the LES-CSE results, the RANS-CSE calculations produce higher centreline velocities. In both flames, at 30mm, the RANS-CSE predictions overestimate the centreline velocity, whereas the LES-CSE centreline velocity is in very good agreement with the experimental data at this location. Farther downstream, the RANS-CSE results are in very good agreement with the experimental data, and agree well with the LES-CSE results away from the centreline.

The radial profiles of time-averaged resolved radial velocity, $\langle V \rangle$, are given in Fig. 7.5 for the DJHC-I 4100 flame and Fig. 7.6 for the DJHC-I 8800 flame, at different heights, and compared with available experimental data [54, 55]. For both flames, the agreement between the LES predictions and experimental values are not as good for the radial velocity component compared to what is observed for the axial component, in particular close to the nozzle, at 15 mm and 30 mm.

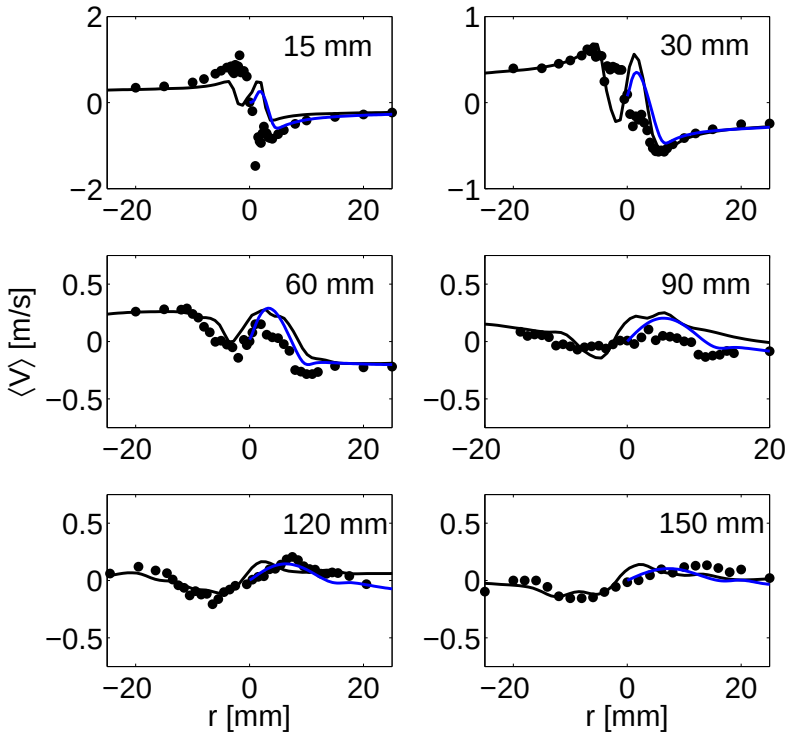

Figure 7.5: LES-CSE time-averaged resolved radial velocity profiles in the radial direction (solid line) compared to RANS-CSE numerical predictions (blue line) and compared to experimental data [54, 55] (symbols) at various axial locations for the DJHC-I 4100 flame

Farther downstream, at 120 mm and 150 mm for the DJHC-I 4100 flame (Fig. 7.5) and 120 mm for the DJHC-I 8800 flame (Fig. 7.6), the LES radial velocity is in reasonable agreement with the experimental profiles. For the radial velocity profiles, the RANS-CSE and current LES-CSE predict similar profiles, both in shape and magnitude. The discrepancies observed close to the fuel and coflow inlets may point towards some inaccuracies in the inlet conditions. It should be noted that the rms level for the radial component measured in the experiments is high, exceeding 3.5 m/s for some radial velocities between -1 and 1 m/s. These conditions are typically more difficult to capture in any simulation.

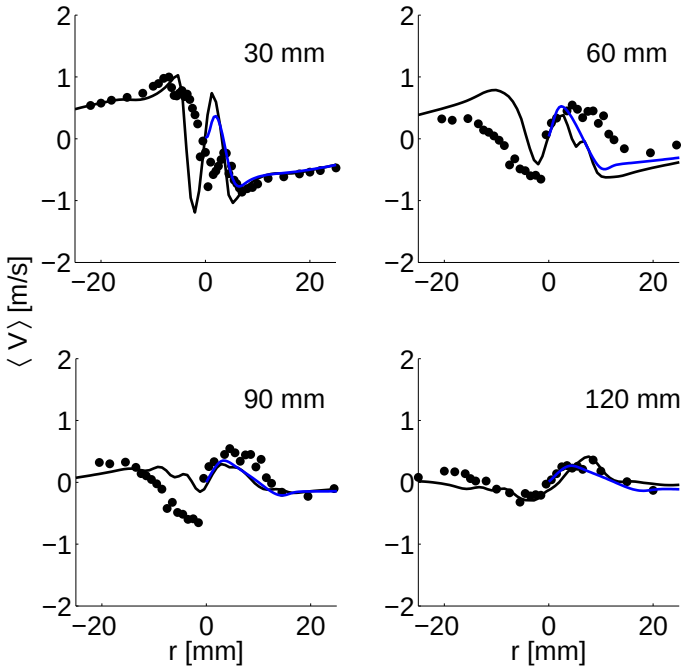

Figure 7.6: LES-CSE time-averaged resolved radial velocity profiles in the radial direction (solid line) compared to RANS-CSE numerical predictions (blue line) and compared to experimental data [54, 55] (symbols) at various axial locations for the DJHC-I 8800 flame

The time-averaged normal stress $\langle u'u' \rangle$ profiles are presented and compared with available experimental data in Fig. 7.7 for the DJHC-I 4100 flame and Fig. 7.8 for the DJHC-I 8800 flame. As shown in Fig. 7.7, close to the nozzle, at 15 mm, the predicted normal stresses are in excellent agreement with the experimental data, both in shape and magnitude. Farther downstream at 30 mm, the shape of $\langle u'u' \rangle$ is captured well, but the centreline values are overestimated by approximately 40%, when compared with the experimental values. At the axial location of 60 mm, excellent agreement between the LES results and experimental data is regained. Farther away, past 60 mm, near the centreline, $\langle u'u' \rangle$ values are shown to be underestimated, but closely follow the shape of the experimental profiles.

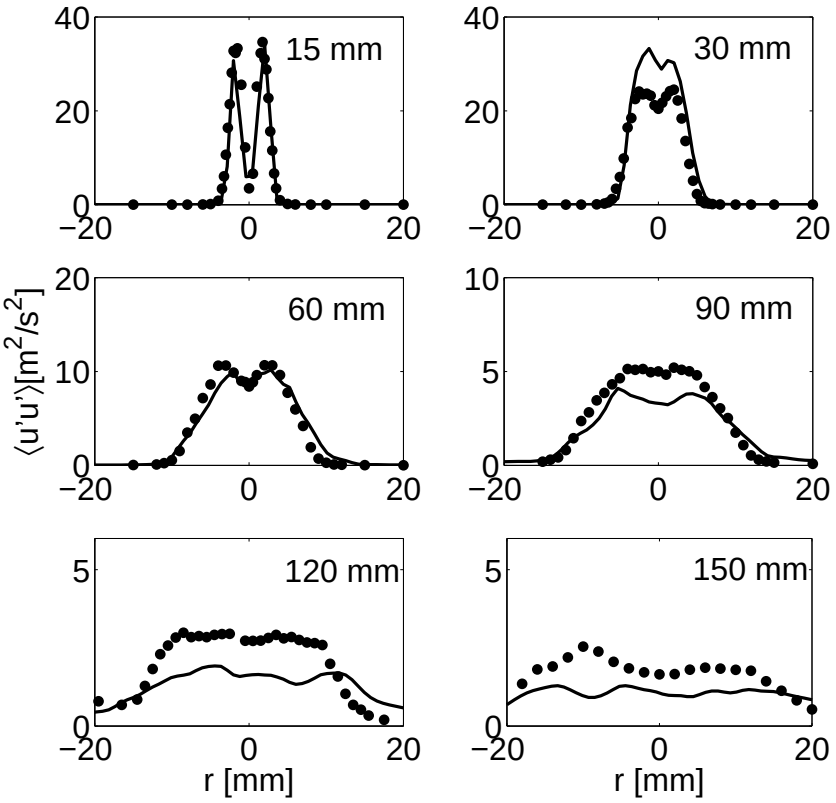

Figure 7.7: LES-CSE time-averaged resolved axial velocity fluctuation profiles in the radial direction (solid line) compared to experimental data [54, 55] (symbols) at various axial locations for the DJHC-I 4100 flame

As can be seen in Fig. 7.8, similar observations can be made for the DJHC-I 8800 flame. At 30 and 60 mm, the normal stresses are larger than the experimental measurements by approximately 50%. Farther downstream, the present LES predicts the correct trends, but underpredict the peak by 30% and 50% at 90 and 120 mm, respectively.

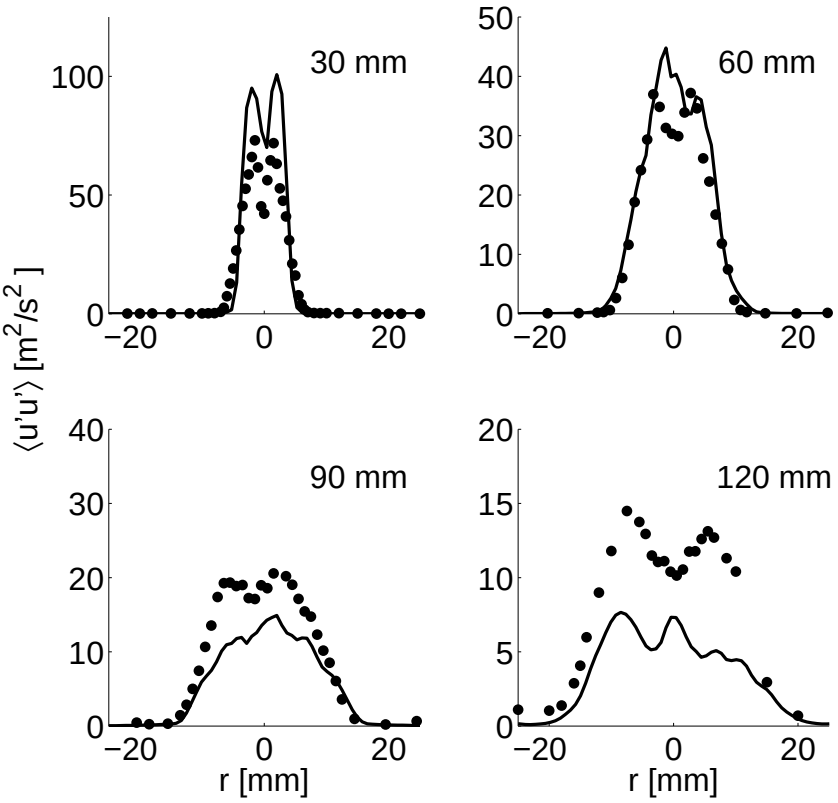

Figure 7.8: LES-CSE time-averaged resolved axial velocity fluctuation profiles in the radial direction (solid line) compared to experimental data [54, 55] (symbols) at various axial locations for the DJHC-I 8800 flame

The shear stress $\langle u'v' \rangle$ profiles are presented for five axial locations in Figs. 7.9 and 7.10 for the DJHC-I 4100 case and the DJHC-I 8800 flame, respectively. As shown in Fig. 7.9, near the nozzle at 15 mm and at 30 mm, the shape and magnitude of $\langle u'v' \rangle$ match the experimental profiles closely. Farther downstream, the present LES correctly predicts the shape and general trend of decreasing $\langle u'v' \rangle$ with increased axial distance from the nozzle.

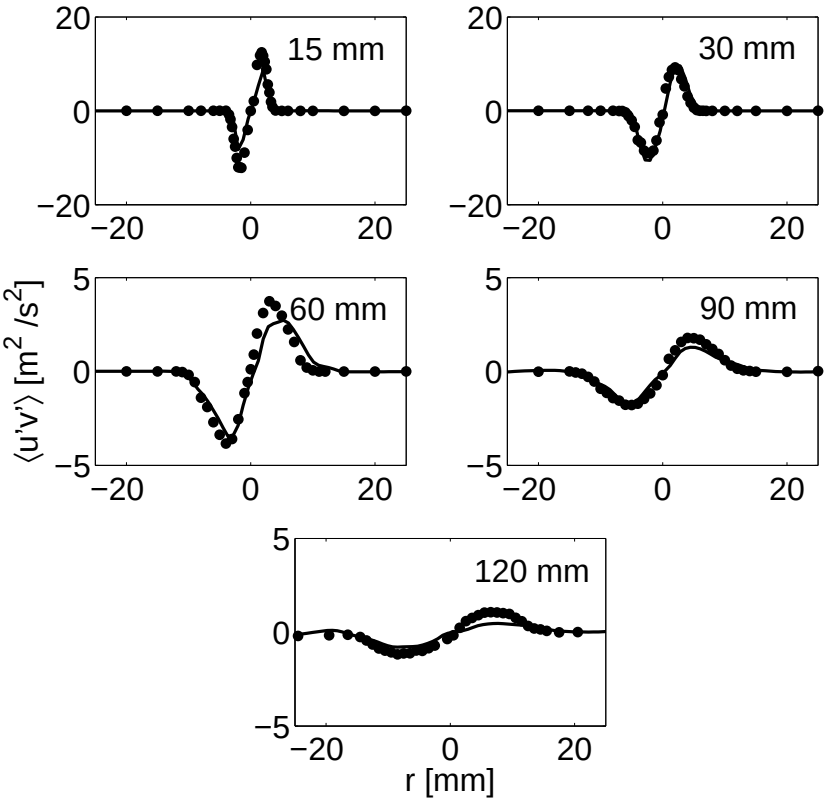

Figure 7.9: LES-CSE time-averaged resolved u′v′ profiles in the radial direction (solid line) compared to experimental data [54, 55] (symbols) at various axial locations for the DJHC-I 4100 flame

As can seen in Fig. 7.10, the predicted $\langle u'v' \rangle$ is in good agreement with the experimental data. The largest discrepancy is shown for the peak values at 30 mm with an overprediction of approximately 40% compared to the experimental data, and at 90 and 120 mm with an underprediction on the order of 50%. The fact that $\langle u'u' \rangle$ and $\langle u'v' \rangle$ are accurately captured near the nozzle, as shown in Figs. 7.7 and 7.9 at 15 mm, seems to indicate that the synthetic turbulence produces appropriate profiles for these fluctuating components.

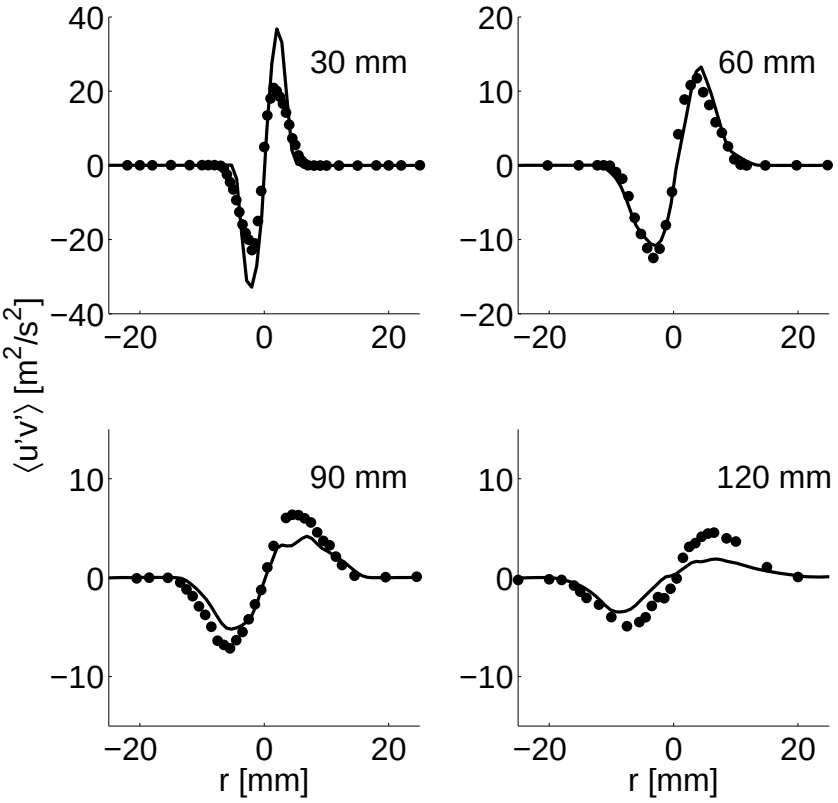

Figure 7.10: LES-CSE time-averaged resolved u′v′ profiles in the radial direction (solid line) compared to experimental data [54, 55] (symbols) at various axial locations for the DJHC-I 8800 flame

Figure 7.11 presents the time-averaged resolved turbulent kinetic energy profiles for the DJHC-I 4100 and DJHC-I 8800 flames at different downstream locations. The turbulent kinetic energy profiles reported in the experimental investigations are calculated using the u′u′ and v′v′ profiles by assuming w′w′ = v′v′ [55]. The numerical resolved turbulent kinetic energy is determined by extracting $\langle u'u' \rangle$, $\langle v'v' \rangle$ and $\langle w'w' \rangle$, as shown in Section 7.2. In the DJHC-I 4100 flame, the shape of turbulent kinetic energy profile at 15 mm is well captured. However, the peak values for the resolved turbulent kinetic energy are underestimated by approximately 25%. Thus, the time-averaged resolved radial and azimuthal fluctuations at 15 mm must be underpredicted as the simulations accurately reproduce the experimental values of axial normal stress at this location, as shown in Fig. 7.7.

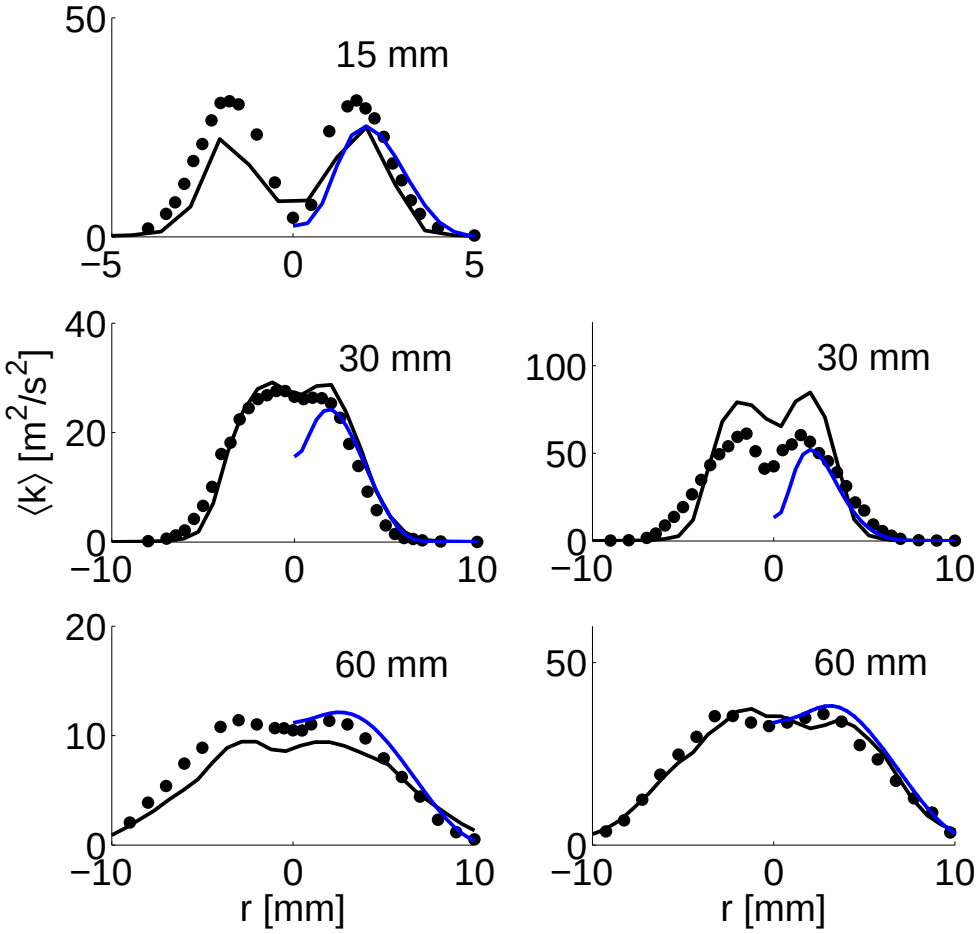

Figure 7.11: LES-CSE time-averaged resolved turbulent kinetic energy profiles in the radial direction (solid line) compared to RANS-CSE numerical predictions (blue line) and compared to experimental data [54, 55] (symbols) at various axial locations for the DJHC-I 4100 flame (left) and DJHC-I 8800 flame (right)

A lower turbulent kinetic energy may indicate a lower amount of entrainment of the coflow, compared to the experiment. This effect is not obvious from the time-averaged resolved axial velocity profiles, as can be seen in Fig. 7.3, due to the low amount of entrainment at this location. Farther downstream at 30 and 60 mm, the turbulent kinetic energy is in good agreement with the experimental data. However, as the $\langle u'u' \rangle$ values

are higher than the experimental data at 30 mm, the $\langle v'v' \rangle$ and $\langle w'w' \rangle$ profiles are underestimated. For the DJHC-I 8800 flame, the axial velocity underprediction seen in Fig. 7.4, may be linked to the overestimation of the peak turbulent kinetic energy at 30 mm, by approximately 40%. Thus, at this location the entrainment of the coflow is significantly overpredicted and the time-averaged resolved centreline axial velocity is lower for all downstream positions. For the DJHC-I 4100 flame, at 15mm, LES-CSE and RANS-CSE simulations yield similar turbulent kinetic energy profiles. Farther downstream at 30mm, the RANS-CSE centreline values are much lower. Combined with the higher centreline velocity seen in the RANS-CSE simulations (Fig. 7.3), this suggests that the velocity underpredictions seen in the current LES-CSE may be due to incorrectly capturing the mixing between the jet and coflow. At 60mm, the turbulent kinetic energy profiles obtained from the RANS-CSE and LES-CSE calculations follow the same shape with the LES-CSE values being slightly lower than the experimental data. Similar conclusions can be made when comparing the turbulent kinetic energy profiles obtained for the LES-CSE and RANS-CSE calculations of the DJHC-I 8800 flame. The velocity profiles and the Reynolds stress components show that accurate modelling of the turbulent fluctuations is needed at the inlet to accurately capture the mixing between the coflow and the fuel stream. The present results along with those of Kulkarni and Polifke [9] and Bhaya et al. [63] demonstrate that this is not a trivial task. The mixing between the fuel, coflow and ambient air is reasonably well predicted, consistent with previous LES work completed on the DJHC-I 4100 and DJHC-I 8800 flames [9, 63].

7.3.2 Temperature predictions

The predicted time-averaged resolved radial temperature profiles are presented in Fig. 7.12 and 7.13 for the DJHC-I 4100 flame and DJHC-I 8800 flame, respectively. As can be seen in Fig. 7.12, at 15 and 30 mm, good agreement between the LES-CSE predictions and the experimental data is observed. As shown in Section 7.3.3, the axial locations of 15 and 30 mm are below the lift-off height and good agreement with the experimental results is expected. Farther downstream at 60 mm, near the centreline, a slight overprediction of the temperature can be seen, but the agreement with the experimental values remains very good. With increasing axial distances, the overprediction of the centreline temperature increases from 15% at 90 mm to 20% at 150 mm. In comparison with previous RANS-CSE simulations from Chapter 6, the peak temperatures are better predicted in the current LES-CSE. Much smoother temperature profiles are obtained in the current simulations, in agreement with the experimental data.

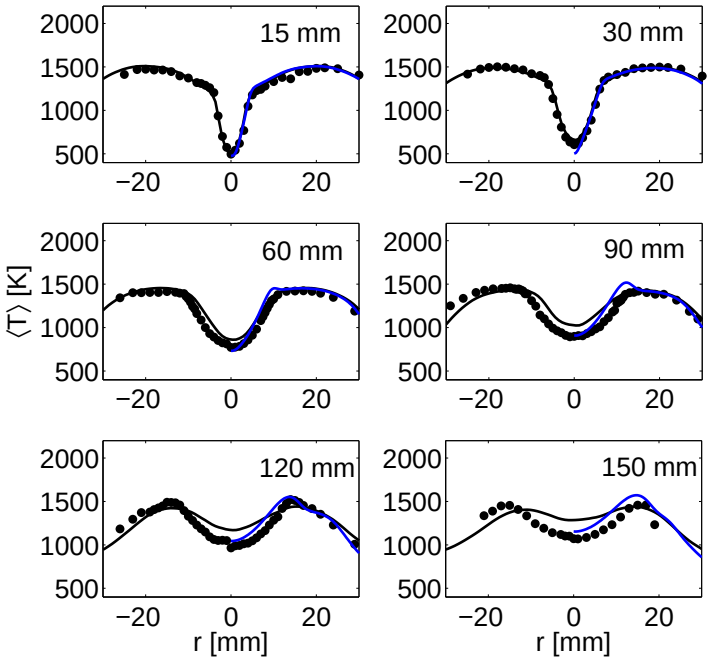

Figure 7.12: LES-CSE time-averaged resolved temperature profiles in the radial direction (solid line) compared to RANS-CSE numerical predictions (blue line) and experimental data [54, 55] (symbols) at different axial locations for the DJHC-I 4100 flame

For the DJHC-I 8800 flame, as shown in Fig. 7.13, close to the nozzle, at 30 mm, the predicted temperatures are in very good agreement with the experimental data. An overestimation, on the order of 19%, of the centreline temperature can be observed at 60 mm. By examining the transient evolution of temperature and OH mass fraction in the present LES, no transient ignition kernels are seen at this location in the present results. Thus, the higher centreline temperature appears to be caused by inaccuracies in the predictions of the coflow entrainment. Farther downstream, at 90 and 120 mm, the overprediction of the centreline temperature increases. At the final axial location, the peak temperature is 7% higher than the experimental data. In comparison to the previous RANS-CSE simulations, the current simulations predict the peak temperatures and the shape of the temperature profile more accurately. At 120 mm, the peak temperature predicted in the simulations is overestimated by 7%, compared to 20% in the RANS calculations. Thus, the higher temperature seen in the RANS simulation is most likely caused by inaccurately predicting the mixing between the ambient cold air, coflow and fuel. Only close to the centreline, the

RANS predictions are closer to the experimental values compared to what is seen in LES, for all axial locations. Thus, overall, the present LES-CSE calculations yield improved predictions over the previous RANS-CSE values. Based on the LES and RANS temperature profiles, the importance of calculating the correct mixing between the three streams is reinforced since it has a direct impact on the reaction rates and temperatures predicted by the CSE combustion model.

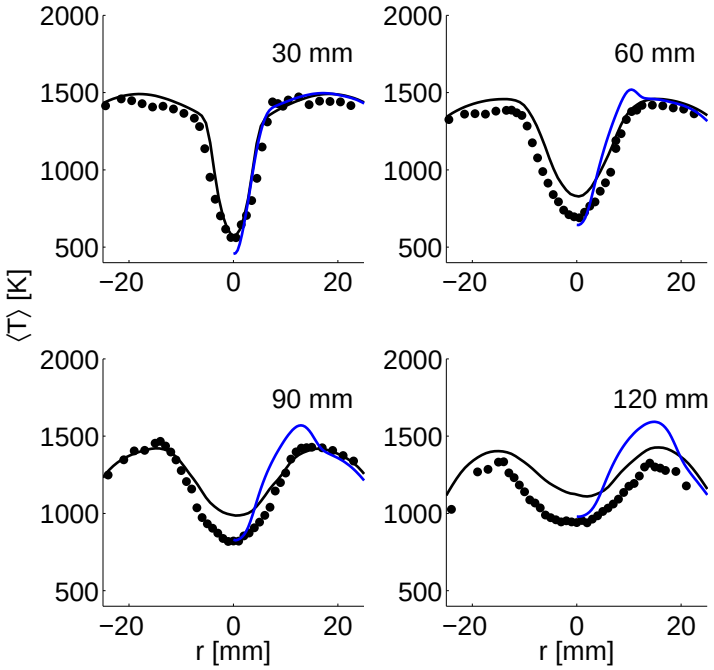

Figure 7.13: LES-CSE time-averaged resolved temperature profiles in the radial direction (solid line) compared to RANS-CSE numerical predictions (blue line) and experimental data [54, 55] (symbols) at various axial locations for the DJHC-I 8800 flame

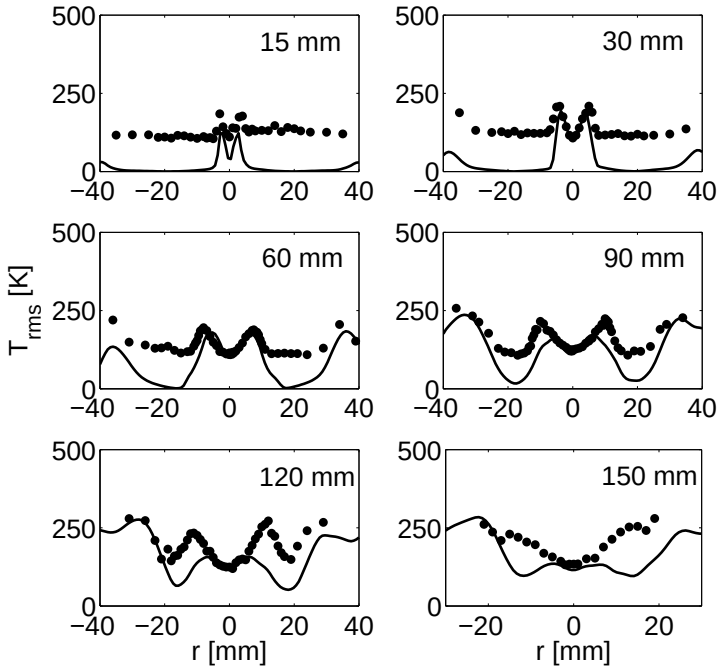

Figure 7.14: LES-CSE temperature rms profiles in the radial direction (solid line) compared to experimental data [54, 55] (symbols) at various axial locations for the DJHC-I 4100 flame

In addition to the time-averaged resolved temperature profile, the temperature rms fluctuations are also obtained and shown in Fig. 7.14. Similar to the work of Bhaya et al. [63], no temperature fluctuation is imposed at the inlet of the computational domain. Thus, the temperature fluctuations in the coflow are expected to be significantly underpredicted near the nozzle. This can be clearly seen at 15 mm where the temperature rms values at the centreline are underpredicted by 70 K, whereas the coflow temperature rms fluctuations are underpredicted by 130 K. However, the general shape of the temperature rms profile is qualitatively similar to the experimental profile. Downstream at 30 and 60 mm, the rms profiles match the experimental data well close to the centreline. Away from the centreline, the rms values are underpredicted, but the trend of increased rms fluctuations near the coflow/air boundary is correctly reproduced. At 90 mm, the general shape of the temperature rms profile is well captured, but the temperature rms peak, 10 mm away from the centreline, is lower than the experimental measurement. This trend continues for the remaining axial locations with the centreline rms fluctuations being accurately captured

and the peak values being underpredicted.

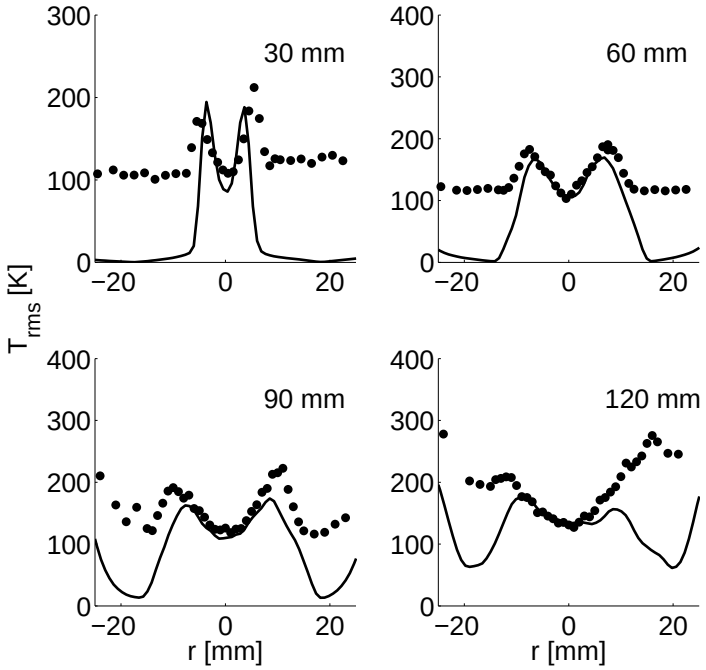

Figure 7.15: LES-CSE temperature rms profiles in the radial direction (solid line) compared to experimental data [54, 55] (symbols) at various axial locations for the DJHC-I 8800 flame

The temperature rms fluctuations for the DJHC-I 8800 flame are presented in Fig. 7.15 and compared to experimental data. As can be seen in Fig. 7.15, the temperature rms values are in very good agreement with the experimental data, both in terms of magnitude and shape at 30 and 60 mm near the centreline. Away from the centreline, lower rms values are seen and are caused by assuming zero temperature fluctuations at the inlet. Farther downstream, at 90 and 120 mm, the general shape of the temperature rms is well reproduced, but the peak values are lower than the experimental data. At these locations, a noticeable increase in the temperature rms fluctuations compared to what is observed at lower axial locations, can be seen for radial positions greater than 10 mm. This increase in the temperature rms indicates that the interaction between the coflow and ambient air has an impact on the flame. At the last axial location, 120 mm, the peak temperature rms occurs at 25 mm in the radial direction and are 50% higher than the fluctuations at the

same radial positions seen upstream at 90 mm. From the temperature profile at 120 mm, as shown in Fig. 7.13, it can be seen that the temperature at these radial locations has decreased compared to the value displayed upstream at 90 mm, from 1248K to 1137K, indicating that colder fluid has been entrained between these positions. The present LES-CSE calculations capture this phenomenon showing a corresponding decrease in temperature and increase in temperature fluctuations at these locations. Further improvement in the LES results may be obtained by including the temperature fluctuations at the coflow inlet.

7.3.3 Lift-off height predictions

Experimentally, the lift-off height is determined using the probability of the presence of flame pockets [55]. In the experiments, the flame pockets are identified from a series of instantaneous luminescence images. In the simulations, a criterion needs to be set to define the flame pocket boundaries. Following what has been selected in previous numerical results for the same DJHC flames [9, 63], in the present study, a flame pocket is defined as a region in space where an OH mass fraction reaches a value of 10^{-3}. Further, in the experiments, two different methods are presented to determine the probability of the presence of the flame pockets [55]. In the first approach, P_{b1} corresponds to the probability of finding a flame pocket anywhere on a radial line stretching outward from the burner axis, as a function of axial height. The second definition gives P_{b2} as the probability of finding a flame pocket at a certain axial height. In other words, the first method examines flame pockets on the centre (x,z) plane assuming that the flame is axisymmetric and the second approach searches for flame pockets radially at a given height, sweeping over the azimuthal direction. Consistent with the experimental calculations, in the present LES results, for each instantaneous OH mass fraction field, a one-dimensional function $b(x,t)$, representing the flame pocket is applied taking the value of zero when there is no flame pocket and the value of unity when a flame pocket is present. For P_{b1}, using only half of the centre (x,z) plane, at a given axial location and given time, the presence of a flame pocket is determined, i.e if $b(x,t) = 1$. This procedure is repeated for every axial location in the LES grid for a number of time instants equally spread over the entire simulation time. For the DJHC-I 4100 and 8800 flames 125 and 132 time instants are used, respectively. Thus, at a given axial location, P_{b1} is found by adding the number of flame pocket occurrences, and dividing this number by the number of time instants. It should be noted that a larger number of time instants was tested and the differences are found to be negligible with what is determined with 125 or 132 time instants, depending on the flame. As for P_{b2}, the exact same procedure is considered, but instead of considering only half of the centre (x,z) plane, this is applied to all radial locations and all azimuthal locations at a given axial height.

The lift-off is defined as the axial location where P_{b1} or P_{b2} is equal to 0.5. The first lift-off height, H_{b1}, is extracted from the profile of P_{b1} and the second lift-off height, H_{b2}, comes from P_{b2}. The experimental study indicates that both definitions yield similar trends [55]. It seems that one definition is preferred to another in the experimental studies [54, 55] depending on the magnitude of the lift-off height and the field of view of the camera.

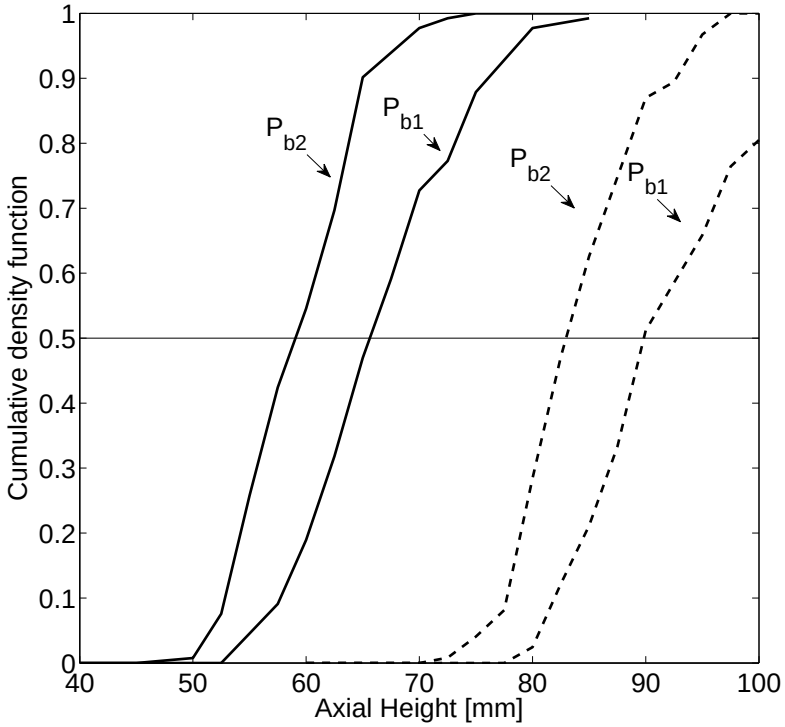

Figure 7.16: CSE predicted P_{B1} and P_{B2} cumulative density functions for the DJHC-I 4100 (solid line) and DJHC-I 8800 (dashed line) flames

The two probabilities, P_{b1} and P_{b2}, are given in Fig. 7.16 as functions of the axial distance for the DJHC-I 4100 and DJHC-I 8800 flames. The resulting lift-off heights for both flames are presented in Table 7.1. It is interesting to note that the lift-off height is found to be sensitive to fuel composition [55]. In particular, the lift-off height is significantly altered when the fuel is changed from Dutch natural gas to Fuel I which is close to Dutch natural gas in composition. The major difference in the composition is the presence of ethane in Dutch natural gas (3.7% ethane and 0.6% higher alkanes in addition to 14.4% N_2 and 81.3% CH_4 by volume). The influence of the composition on the lift-off height is visible

in Table 7.1 by examining the trends between Dutch natural gas and Fuel I. In contrast to what is seen in Dutch natural gas, the lift-off height for Fuel I is shown to increase as the Reynolds number changes from 4100 to 8800. As Fuel I is used in the current simulations the remaining analysis will be compared to the experimental Fuel I data.

Table 7.1: Numerical and experimental lift-off heights using P_{b1} and P_{b2} for the two DHJC flames under consideration. Lift-off heights are given in mm. DNG is Dutch natural gas.

Simulation Case	LES-CSE H_{b1}	LES-CSE H_{b2}	DNG H_{b1}	Fuel I H_{b1}	Fuel I H_{b2}
DJHC-I 4100	66	59	80	103	85
DJHC-I 8800	89	83	77	160	93

First, the comparison will focus on the values of H_{b1}. As can be seen in Table 7.1. the LES-CSE results indicate that the lift-off height is underpredicted by 36% and 44% for the DJHC-I 4100 and DJHC-I 8800 flames, respectively. However, the trend of increasing lift-off height with increasing Reynolds number is properly captured. In comparison, the predicted H_{b2} lift-off heights are in good agreement with the experimental data with a underprediction of approximately 30% for the DJHC-I 4100 flame and 10% for the DJHC-I 8800 flames. A possible explanation for the lower lift-off heights is that the current CSE model does not account for small scale straining and its effect on autoignition or local extinction. This could be accommodated by adding a third conditioning variable, for example based on strain, temperature or enthalpy, in the CSE formulation.

Another possible improvement in the current LES-CSE lift-off height predictions could be made by changing the chemistry tabulation. Currently, two species mass fractions, H_2O and CO_2, are selected to characterize the chemical activity. Kulkarni and Polifke [9] saw significant improvements in their lift-off height predictions when changing their progress variable from CO_2 to $CH_2O + CO + CO_2$. This could be explained by the fact that H_2O and CO_2 have long formation times, and therefore, may be unable to capture accurately the effect of minor or intermediate species on the formation of OH. A similar approach could be implemented in CSE by using a composite characteristic mass fraction for the tables or with the addition of a progress variable as a third conditioning variable. For the composite characteristic mass fraction, c, defined as $c = CH_2O + CO + CO_2$, the tables would become functions of η, v and c and a transport equation is solved for c.

7.3.4 Flame characteristics

The behaviour of jet-in-hot-coflow flames differs significantly from conventional lifted flames, where a single sharp flame surface moves up or down in a coherent structure and flame stabilization may be due to flame propagation [55]. In the DJHC flames, the flame stabilization is not due to flame propagation and the flame structure is not coherent or stable [55]. Instead, flame stabilization is due to the formation of ignition kernels which grow and convect downstream connecting to form a flame front. Six instantaneous LES snapshots are taken from the DJHC-I 8800 flame showing the flame front, defined as $\widetilde{Y}_{OH} \geq 10^{-3}$, and velocity vectors along the centreplane are shown in Fig. 7.17. At 0 second, the flame front is connected and unburnt pockets of reactants are seen within the flame surface. These unburnt pockets are also seen in the LES of Kulkarni and Polifke [9] for both the DJHC-I 4100 and DJHC-I 8800 flames. After 0.44 ms, an ignition kernel forms in the coflow, in a region of low relative velocity. At the same time, the size of the unburnt pockets within the flame front decreases. Over the next 1.36 ms, the ignition kernel grows and is convected downstream by the jet. The ignition kernel then connects with the main flame front and a second ignition kernel, independent from the first, is seen after 2.17 ms. Thus, the present LES-CSE calculations correctly predict the flame stabilization mechanism seen in the DJHC-I flames qualitatively. The LES-CSE results display a flame which does not have a single sharp flame surface that moves up or down, seen in traditional lifted flames. Instead, the LES-CSE snapshots show a flame surface that is more random with a lift-off height that varies significantly. In the current simulations, ignition kernels are seen below 50 mm and 72.5 mm for the DJHC-I 4100 and DJHC-I 8800 flames, approximately 18% and 15% below the calculated lift-off height. The probability of finding a flame kernel at or below these axial locations is approximately 0.7% and 0.8% for the DJHC-I 4100 and DJHC-I 8800 flames, respectively. Experimentally the location of first ignition kernel is defined as the axial height with a flame pocket probability of 0.25% [55]. For Fuel I, the first ignition kernel is found to be approximately 18% and 27% below the measured lift-off height for the DJHC-I 4100 and DJHC-I 8800 flames [55], respectively. Thus, the LES-CSE results correctly predict a large variation in the flame pocket location as a function of time consistent with the experimental observations.

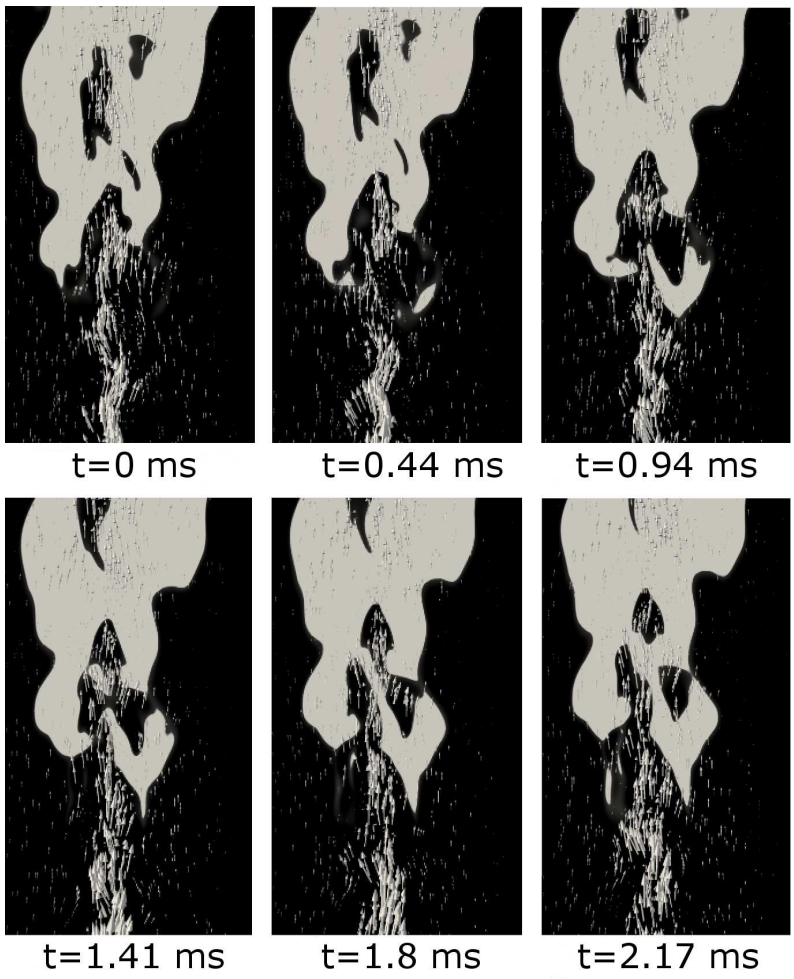

Figure 7.17: Flame front, defined as $\widetilde{Y}_{OH} \geq 10^{-3}$, and velocity vectors at six instantaneous time steps for the DJHC-I 8800 flame

An instantaneous snapshot of the CH_4 reaction rate and corresponding instantaneous temperature profiles are presented in Fig. 7.18(a) and Fig. 7.18(b), respectively, to demonstrate the chemical activity observed in the DJHC-I 8800 flame. Below 75 mm very little CH_4 is consumed, some reformation of CH_4 is observed, and the temperature increases due to hot coflow entrainment. Above 75 mm, consumption of CH_4 occurs where the hot coflow and fuel have mixed sufficiently, with the peak chemical activity occurring on the outer edge of the flame. At these locations, a corresponding temperature increase and change in turbulent structures are also noted. Similar observations are obtained for the DJHC-I 4100 flame.

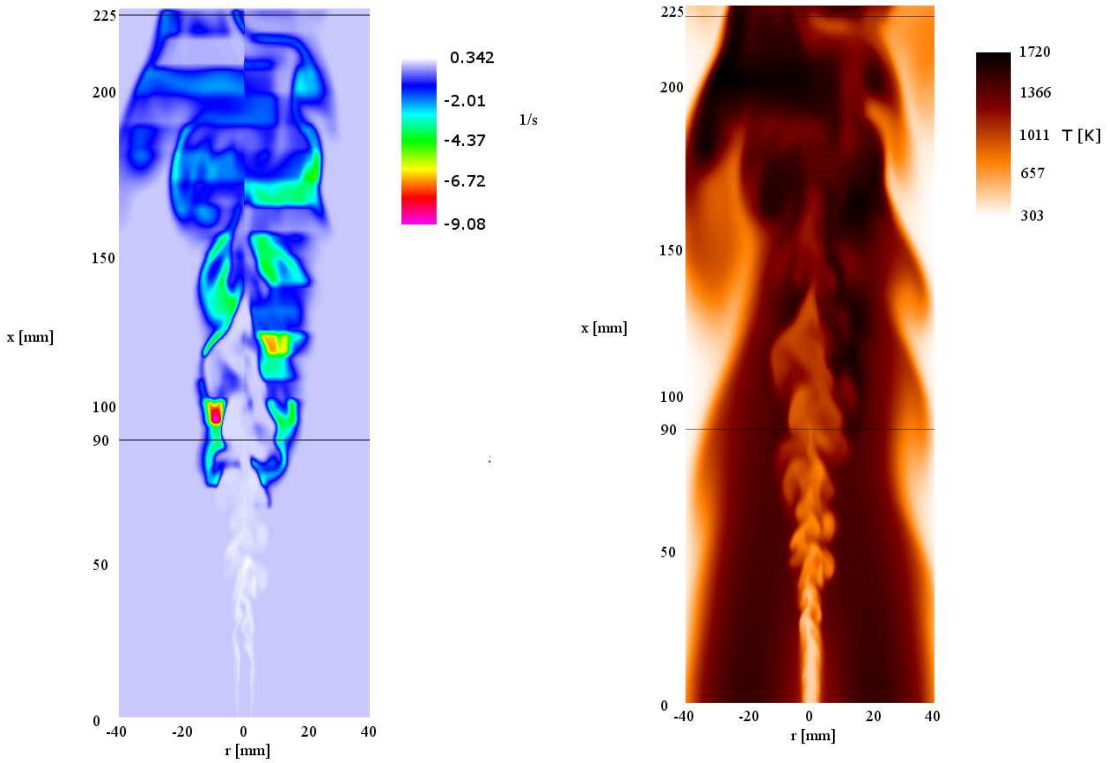

(a) Instantaneous methane reaction rate

(b) Instantaneous temperature

Figure 7.18: Instantaneous methane reaction rate and temperature for the DJHC-I 8800 flame on the centreplane. The black lines at 90 mm and 225 mm correspond to the locations where the conditional averages are shown in Fig. 7.19

7.3.5 Conditional mass fractions

The conditional mass fractions of CO_2 are investigated to determine whether the DJHC-I flames require two mixture fractions to accurately capture the mixing between the fuel, coflow and shroud air. The conditional mass fraction of CO_2 for the DJHC-I 8800 flame is presented in Fig. 7.19 for each half of the computational domain, at two axial locations, 90 mm and 225 mm. At 90 mm, very little shroud air has been entrained with the fuel/coflow mixture and the turbulent structures are relatively small. Thus, at this location, the conditional averages are very similar for both halves of the CFD domain with the location of maximum CO_2 occurring at low values of η and υ. With increased axial height additional shroud air is entrained and the location of maximum CO_2 is expected at higher υ values. Figure 7.19 c) and d) confirm that this expected behavior is captured in the LES-CSE calculations. In addition, larger variations in the conditional profiles between the two halves of the domain demonstrate that the amount of entrained shroud air can vary significantly between the two halves of the domain. The change in the conditional profiles between 90 mm and 225 mm demonstrates that a second mixture fraction is required to accurately capture the entrainment of the shroud air.

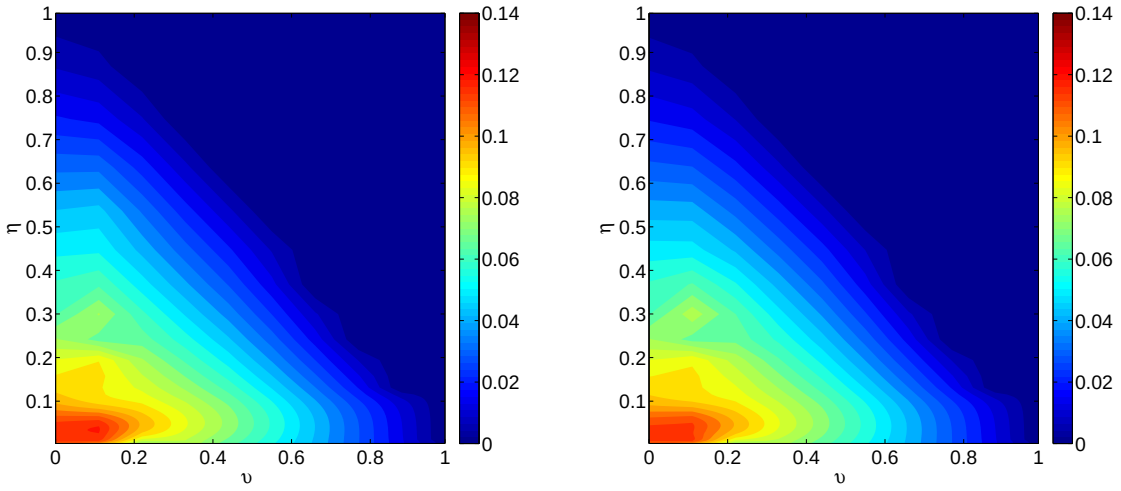

(a) 90 mm Left

(b) 90 mm Right

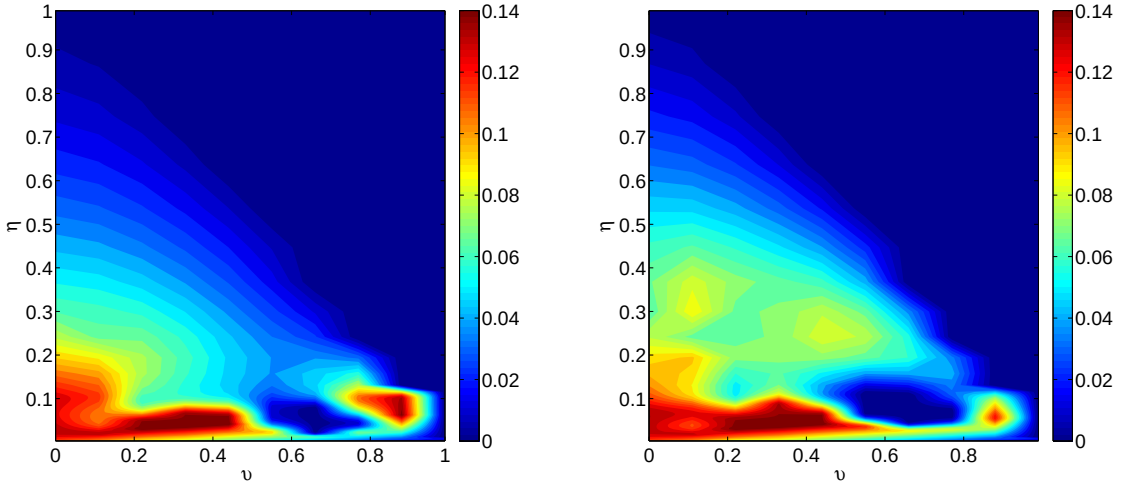

(c) 225 mm Left

(d) 225 mm Right

Figure 7.19: Instantaneous $\langle Y_{CO_2} | \eta, \upsilon \rangle$ profiles at various axial heights for each side of the CFD domain

7.4 Summary

A two mixture fraction CSE formulation was implemented in LES to simulate two DHJC flames representative of MILD combustion at a laboratory scale. For the first time, a double conditioned CSE model was successfully applied in the LES framework.

Overall, good agreement with experimental data was found for the turbulent flow field statistics. Some discrepancies were noted, in particular near the centreline for axial locations greater than 60 mm for both flames due to inaccuracies in the coflow entrainment. This effect was found to be higher in the DJHC-I 8800 flame. For both flames, the agreement between the LES predictions and experimental values are not as good for the radial velocity component compared to what is observed for the axial component, in particular close to the nozzle. The identified sources of discrepancy were the constant Smagorinsky model used in the present LES, and the inlet turbulence conditions. The present velocity predictions are found to follow similar trends as those presented in previous LES for the same flames [9, 63].

The predicted temperatures were also in good agreement with the experimental data. At axial locations away from the nozzle exit, the centreline temperature is overpredicted due to early prediction of ignition kernels by CSE and increased coflow entrainment. The peak temperatures predicted for the DJHC-I 8800 flame by CSE were in good agreement with the experimental data below 120 mm. At 120 mm, the peak temperature from the CSE simulation was higher than the experimental data. Compared to the RANS-CSE results, the peak temperatures and shape of the temperature profiles were better captured in the present LES-CSE. As for the temperature rms, an underprediction was shown close to the nozzle due to the fact that no temperature fluctuation was set at the inlet boundary. Farther down, the temperature rms predictions were in reasonable agreement with the experimental measurements.

The predicted lift-off heights were lower than the experimental values. However, the trend of increasing lift-off height with increasing Reynolds number was properly captured when the LES-CSE results were compared with the experimental data using the same fuel composition as that in the LES-CSE. The lift-off height predictions may be improved by adding a third conditioning variable that would reflect the effect of straining or changing the chemistry tabulation using different chemical progress variables. Qualitatively, the present simulations correctly predicted flame stabilization due to the formation of ignition kernels which grow and convect downstream to form a flame front.

Chapter 8

Conclusions and future work

8.1 Summary of main findings

In Chapter 3, CSE coupled with TGLDM for chemistry tabulation was implemented in order to simulate a confined non-premixed turbulent methane flame. A sensitivity analysis related to the number of CSE ensembles and ensemble size was performed. The number of CSE ensembles was shown to have a significant impact on the results if not selected appropriately and a sensitivity analysis was recommended for each new CSE application. The number of points in each ensemble was shown to have an impact on the predictions. The presented CSE calculations provided stable and converged predictions. Two different turbulence models were used, the $k-\epsilon$ model with a corrected value for $C_{\epsilon 1}$ and the RNG $k-\epsilon$ model. Overall, the predictions for the mixture fraction were in good agreement with the experimental data. The predicted temperatures using CSE and the $k-\epsilon$ turbulence model with a modified value of $C_{\epsilon 1} = 1.47$ were shown to be in very good agreement with the experimental data. CSE tended to slightly overpredict the peak temperature, thought to be due to the lack of a soot model. Further, the current CSE results were of comparable quality with previous simulations using the flamelet model [17] and CMC [16, 35].

In Chapter 4 the inverse problem encountered in CSE was investigated in a Bayesian framework. It was found that the unconditional species mass fractions obtained from the CSE simulations contained perturbations. These perturbations may be caused by the use of a discrete mixture fraction grid, which resulted in inaccurate predictions of the PDF for very lean mixture fractions. The Bayesian framework was used to investigate the impact of a smoothing prior on the recovered solution and credible intervals. It was found that including a smoothing prior decreased the credible interval width and the recovered solution

better approximated the exact solution. Two regularization methods, zeroth order temporal Tikhonov and first order spatial Tikhonov, were implemented in the Bayesian framework. The width of the credible intervals calculated for zeroth order temporal Tikhonov and first order spatial Tikhonov were found to be similar. Further, for zeroth order temporal Tikhonov the credible intervals were not necessarily smooth and were dependent on the solution from the previous time step. In contrast, the credible intervals for first order spatial Tikhonov were smooth and not dependent upon a previous solution. First order spatial Tikhonov was found to better predict the characteristics of the credible intervals for higher mixture fraction values.

In Chapter 5, the effect of radiation on the conditional reaction rates was accounted for by calculating the conditional enthalpy. The extended CSE approach was applied with the standard $k-\epsilon$ turbulence approach to model a semi-industrial MILD furnace with detailed measurements for temperature, velocity and species concentration. The peak velocities and general shape of the velocity profiles at each axial location were in good agreement with the experimental data. The recirculation was slightly stronger than that seen in the experimental results and the velocity of the fuel jet region was slightly underpredicted away from the centreline. The temperature profiles were also in good agreement for most axial positions. Good agreement between the predicted species concentrations and the experimental data was observed. Near the burner exit, the CO_2 concentration was lower than the experimental data near the fuel jet and a corresponding higher CH_4 concentration was observed, consistent with the results of [60, 68]. The NOx concentrations were in good agreement with the experimental measurements near the burner exit. Farther downstream the centreline concentration of NOx was found to be underpredicted.

In Chapter 6, CSE was implemented to model the DJHC burner by introducing a second mixture fraction to account for the variation in the coflow. Two different flames were considered corresponding to DJHC-I 4100 and DJHC-I 8800. For the DJHC-I 4100 flame the standard $k-\epsilon$ turbulence model was found to accurately predict the radial velocity profiles. The realizable $k-\epsilon$ turbulence model produced better velocity profiles for the DJHC-I 8800 flame. In both flames, the predicted turbulent kinetic energy was in good agreement with the experimental data. For the DJHC-I 4100 flame, the radial CSE temperature predictions were in close agreement with the experimental data. For the DJHC-I 8800 flame, at 30, 60 and 90 mm downstream of the nozzle, in the first half of the flame near the centreline, the radial CSE temperature profiles were slightly larger than the experimental values and in the second half of the flame in the radial direction, the CSE predictions were in close agreement with the experimental results. The CSE temperature predictions were not as good for the last axial location. The discrepancies in the temperature predictions were attributed to some inaccuracies in the predicted entrainment of the ambient air and coflow due to RANS limitations. CSE correctly predicted the trend

of lift-off height decreasing with increasing Reynolds number. Although the lift-off height criterion was different, the predicted lift-off height appeared underpredicted compared to the experiments. The presented results demonstrated that RANS-CSE using two mixture fractions as conditioning variables, could capture the main properties of MILD combustion for the DJHC flame.

Chapter 7 outlined the two mixture fraction CSE formulation implemented in LES to simulate two DHJC flames. For the first time, a double conditioned CSE model was successfully applied in the LES framework. Overall, good agreement with experimental data was found for the turbulent flow field statistics. The predicted temperatures were also in good agreement with the experimental data. At axial locations away from the nozzle exit, the centreline temperature was overpredicted due to early prediction of ignition kernels by CSE and increased coflow entrainment. Compared to the RANS-CSE results from Chapter 6, the peak temperatures and shape of the temperature profiles were better captured in the present LES-CSE. The predicted lift-off heights were lower than the experimental values. However, the trend of increasing lift-off height with increasing Reynolds number was properly captured when the LES-CSE results were compared with the experimental data using the same fuel composition as that in the LES-CSE. Qualitatively, the present simulations correctly predicted flame stabilization due to the formation of ignition kernels which grow and convect downstream to form a flame front.

8.2 Summary of accomplishments

A list of the main outcomes is presented here:

- Numerical simulations of a confined non-premixed methane flame were completed using the CSE non-premixed approach. This study investigated the sensitivity to various CSE model parameters and showed CSE was able to accurately predict non-premixed methane combustion.
- A detailed study of the inversion problem encountered in CSE was investigated using the Bayesian framework. This study investigated the origin of the perturbation seen in the unconditional mass fraction in CSE and demonstrated the impact of a smoothing prior on the recovered solution and credible intervals. Different regularization methods were studied and it was demonstrated that both zeroth and first order Tikhonov were promising regularization methods for CSE.

- The non-premixed CSE formulation was extended to include the impact of radiation of the conditional reaction rates and applied to a semi-industrial furnace. This study showed that a RANS-CSE simulation was able to accurately predict the temperature and species concentration, including NOx, for large scale realistic furnace configurations.

- A multi-stream CSE formulation was developed and applied to the DJHC burners in the RANS framework. This new CSE formulation was able to predict the temperature and velocity profiles in very good agreement with the experimental data.

- The multi-stream CSE formulation was extended to the LES framework and demonstrated that CSE was able to predict the time-dependent nature of the DHJC burners.

8.3 Future work

Two of the turbulent flames investigated in the current work use methane as a surrogate for more complex fuels. Further investigation is needed to extend the TGLDM method to allow for the tabulation of complex fuels such as syngas. Alternatively, a comprehensive review of different tabulation approaches is required to determine if better tabulations methods are available for CSE.

In the present work, no optimization of the inversion process has been investigated. Currently, LU decomposition is applied which produces an exact solution with a deterministic runtime. However, LU decomposition requires a square matrix which involves calculating the $\mathbf{A}^{\mathrm{T}}\mathbf{A}$ matrix, which can be time consuming. A detailed investigation of the computation requirements of LU decomposition and alternative solution methods is needed to optimize the CSE solver for large scale LES simulations.

CSE has been shown to accurately predict laboratory scale burners and semi-industrial furnaces with simple geometries. Further work is needed to determine how CSE performs for industrial applications with complex geometries. Specifically, methods to automatically and dynamically select CSE ensembles during runtime would enable CSE to simulation burners without *a-priori* information about the homogeneity of the conditional averages.

With the conclusion of the current work CSE has been successfully applied to non-premixed, premixed, partially-premixed and multi-stream combustion. A study investigating CSE for multi-room fire modelling would be beneficial as it would demonstrate if CSE can be applied to fire safety applications. Specifically, an investigation of the relative run-time requirements and prediction quality when compared to FDS [129] and FireFOAM [130] would be required.

References

[1] S. Chu and A. Majumdar, "Opportunities and challenges for a sustainable energy future," Nature, vol. 488, pp. 294–303, 2012.

[2] Annual Energy Outlook 2015 with projections to 2040. U.S. Energy Information Administration, 2015.

[3] Transportation in Canada 2014. Transport Canada, 2014.

[4] Office of the Assistant Secretary for Research and Technology Bureau of Transportation Statistics," United States Department of Transportation, 2015.

[5] IATA Annual Review 2014. 2014.

[6] A. Cavaliere and M. de Joannon, "MILD combustion," Prog. Energy Combust. Sci, vol. 30, pp. 329–366, 2004.

[7] H. Tsuji, A. Gupta, T. Hasegawa, M. Katsuki, and M. Morita, High Temperature Air Combustion: From Energy Conservation to Pollution Reduction. CRC Press, 2003.

[8] R. Cant and E. Mastorakos, An Introduction to Turbulent Reacting Flows. Imperial College Press, 2008.

[9] R. Kulkarni and W. Polifke, "LES of Delft-Jet-In-Hot-Coflow (DJHC) with tabulated chemistry and stochastic fields combustion model," Fuel Process Technol, vol. 107, pp. 138–146, 2013.

[10] H. Versteeg and W. Malalasekera, An Introduction to Computational Fluid Dynamics The Finite Vlomume Method. Pearson Education, 2007.

[11] S. Pope, Turbulent Flows. Cambridge Press, 2000.

[12] B. E. Launder and B. I. Sharma, "Application of the energy-dissipation model of turbulence to the calculation of flow near a spinning disc," Int. Commun. Heat Mass Transfer, vol. 1, pp. 131–138, 1974.

[13] W. Rodi, Turbulence models and their application in hydraulics. Amsterdam: International Association for Hydraulic Research, 1993.

[14] S. B. Pope, "An explanation of the turbulent round-jet/plane-jet anomaly," AIAA Journal, vol. 16, pp. 279–281, 1978.

[15] B. B. Dally, D. F. Fletcher, and A. R. Masri, "Flow and mixing fields of turbulent bluff-body jets and flames," Combust. Theor. Model., vol. 2, pp. 193–219, 1988.

[16] R. W. B. A. Kronenburg and J. H. Kent, "Modeling soot formation in turbulent methaneair jet diffusion flames," Combust. Flame, vol. 121, pp. 24–40, 2000.

[17] S. J. Brookes and J. B. Moss, "Predictions of soot and thermal radiation properties in confined turbulent jet diffusion flames," Combust. Flame, vol. 116, pp. 486–503, 1999.

[18] P. D. Y. Bartosiewicz, Z. Aidoun and Y. Mercadier, "Numerical and experimental investigations on supersonic ejectors," Int. J. Heat Fluid Flow, vol. 26, pp. 56–70, 2005.

[19] A. Leonard, "Energy cascade in Large Eddy Simulation of turbulent fluid flow," Adv. Geophys., vol. 18A, pp. 237–248, 1974.

[20] M. Germano, U. Piomelli, P. Moin, and W. Cabot, "A dynamic sub-grid-scale eddy viscosity model," Phys. Fluids A, vol. 3, pp. 1760–1765, 1991.

[21] V. Eswaran and S. Pope, "An examination of forcing in direct numerical simulations," Comput. Fluids, vol. 16, pp. 257–278, 1988.

[22] D. Veynante and L. Vervisch, "Turbulent combustion modeling," Prog. in Energ. Combust. Sci, vol. 28, pp. 193–266, 2002.

[23] N. Peters, Turbulent Combustion. Cambridge University Press, 2000.

[24] A. Klimenko and R. Bilger, "Conditional moment closure for turbulent combustion," Prog. Energy Combust. Sci., vol. 25, no. 6, pp. 595–687, 1999.

[25] R. Bilger, "Turbulent flows with nonpremixed reactants," in Turbulent Reacting Flows (P. Libby and F. Williams, eds.), vol. 44 of Top. Appl. Phys., pp. 65–113, Springer Berlin / Heidelberg, 1980.

[26] J. Warnatz, U. Mass, and R. Dibble, Combustion. Springer-Verlag, 1999.

[27] R. W. Bilger, "Turbulent jet diffusion flames," Prog. Energy Combust. Sci, pp. 87–109, 1976.

[28] B. Magnussen and B. Hjertager, "On mathematical modeling of turbulent combustion with special emphasis on soot formation and combustion," Proc. Combust. Inst., vol. 13, p. 649:657, 1971.

[29] A. De, E. Oldenhof, P. Sathiah, and D. Roekarts, "Numerical Simulation of Delft-Jet-in-Hot-Coflow (DJHC) Flames Using the Eddy Dissipation Concept Model for TurbulenceChemistry Interaction," Flow Turbul. Combust., vol. 87, p. 537:567, 2011.

[30] N. Peters, "Local quenching due to flame stretch and non-premixed turbulent combustion," Western States Section of the Combustion Institute, vol. 19, pp. 39–49, 1980.

[31] V. Kuznetsov, "Effect of turbulence on the formation of large superequilbrium concentration of atoms and free radicals in diffusion flames," Mehan. Zhidkosti Gasa, vol. 6, pp. 3–9, 1982.

[32] F. Williams in Turbulent Mixing in Nonreactive and Reactive Flows (S. Murry., ed.), pp. 189–208, Plenum Press, New York, 1975.

[33] R. Bilger, "Conditional moment closure for turbulent reacting flows," Phys. Fluid A: Fluid Dynam., vol. 5, pp. 436–444, 1993.

[34] A. Y. Klimenko, "Multicomponent diffusion of various admixtures in turbulent flow," Fluid Dynamics, vol. 25, pp. 327–334, 1990.

[35] R. Woolley, M. Fairweather, and Yunardi, "Conditional moment closure modelling of soot formation in turbulent non-premixed methane and propane flames," Fuel, pp. 393–407, 2009.

[36] S. Kim, K. Huh, and D. Dally, "Conditional moment closure modeling of turbulent nonpremixed combustion in diluted hot coflow," Proc. Combust. Inst., vol. 30, pp. 751–757, 2005.

[37] S. Pope, "Lagrangian PDF methods for turbulent flows," Annu. Rev. Fluid Mech., vol. 26, pp. 23–63, 1994.

[38] S. Pope, "PDF methods for turbulent reacting flows," Prog. Energy Combust. Sci., vol. 11, pp. 119–192, 1985.

[39] W. K. Bushe and H. Steiner, "Conditional moment closure for large eddy simulation of non-premixed turbulent reacting flows," Phys. Fluids, vol. 11, pp. 1896–1906, 1999.

[40] W. Bushe and H. Steiner, "Laminar flamelet decomposition for conditional source-term estimation," Phys. Fluids, vol. 15, p. 1564, 2003.

[41] B. Jin, R. Grout, and W. K. Bushe, "Conditional Source-Term Estimation as a Method for Chemical Closure in Premixed Turbulent Reacting Flow," Flow, Turbulence and Combustion, vol. 81, pp. 563–582, 2008.

[42] R. W. Grout, W. K. Bushe, and C. Blair, "Predicting the ignition delay of turbulent methane jets using conditional source-term estimation," Combust. Theor. Model., vol. 11, pp. 1009–1028, 2007.

[43] J. Huang and W. Bushe, "Simulation of transient turbulent methane jet ignition and combustion under engine-relevant conditions using conditional source-term estimation with detailed chemistry," Combust. Theor. Model., vol. 11, 2007.

[44] N. Wu, W. Bushe, and M. Davy, "On the experimental validation of combustion in turbulent non-premixed jets," Combust. Theor. Model., vol. 14, pp. 855–874, 2010.

[45] M. M. Salehi, W. K. Bushe, and K. J. Daun, "Application of conditional source-term estimation model for turbulence-chemistry interactions in a premixed flame," Combust. Theor. Model., vol. 16, pp. 301–320, 2012.

[46] D. Dovizio, M. M. Salehi, and C. Devaud, "RANS simulation of a turbulent premixed bluff body flame using Conditional Source−term Estimation," Combust. Theor. Model., vol. 17, pp. 935–959, 2013.

[47] N. Shahbazian, M. Salehi, C. Groth, O. Gülder, and W. Bushe, "Performance of conditional source-term estimation model for les of turbulent premixed flames in thin reaction zones regime," Proc. Combust. Inst., vol. 35, no. 3, pp. 1367–1375, 2015.

[48] H. Steiner and W. Bushe, "Large eddy simulation of a turbulent reacting jet with conditional source term estimation," Phys. Fluids, vol. 13, no. 3, pp. 754–769, 2001.

[49] S. Ferraris and J. Wen, "LES of the Sandia flame D using laminar flamelet decomposition for conditional source-term estimation," Flow, Turbulence Combust., vol. 81, pp. 609–639, 2008.

[50] M. Wang, J.Huang, and W. Bushe, "Simulation of a turbulent non-premixed flame using condtional source-term estimation with trajectory generated low-demensional manifold," Proc. Combust. Inst., vol. 31, pp. 1701–1709, 2007.

[51] M. Wang and W. Bushe, "Conditional source-term estimation with laminar flamelet decomposition in large eddy simulation of a turbulent nonpremixed flame," Phys. Fluids, vol. 19, p. 115103, 2007.

[52] S. Lee and C. Devaud, "Application of conditional source-term estimation (cse) to two turbulent non-premixed methanol flames," Combust. Theor. Model, 2016, In Press.

[53] D. Dovizio, J. Labahn, and C. Devaud, "Doubly conditional source-term estimation (DCSE) applied to a series of lifted turbulent jet flames in cold air," Combust. Flame, vol. 162, no. 5, pp. 1976–1986, 2015.

[54] E. Oldenhof, M. Tummers, E. van Veen, and D. Roekaerts, "Role of entrainment in the stabilisation of jet-in-hot-coflow flames," Combust. Flame, vol. 158, pp. 1553–1563, 2011.

[55] E. Oldenhof, M. Tummers, E. van Veen, and D. Roekaerts, "Ignition kernel formation and lift-off behaviour of jet-in-hot-coflow flames," Combust. Flame, vol. 157, pp. 1167–1178, 2011.

[56] B. Dally, A. Karpetis, and R. Barlow, "Structure of turbulent non-premixed jet flames in a diluted hot coflow," Proc. Combust. Inst., vol. 29, pp. 1147–1154, 2002.

[57] A. Verlaan, S. Orsino, N. Lallement, and R. Weber, Fluid flow and mixing in a furnace equipped with the low Nox regenerative burner of Nippon Furnace Kogyo. IFRF Doc. F46=y=1, 1998.

[58] D. R. Hardesty and F. Weinberg, "Burners producing large excess enthalpies," Combust. Sci. Technol., vol. 8, pp. 201–214, 1974.

[59] J. W. J. Wünning, "Flameless oxidation to reduce thermal no-formation," Prog. Energy Combust. Sci., vol. 23, pp. 81–94, 1997.

[60] M. Mancini, R. Weber, and U. Bollettini, "Predicting NOx emissions of a burner operated in flameless oxidation mode," Proc. Combust. Inst, vol. 29, pp. 1155–1163, 2002.

[61] M. Oberlack, R. Arlitt, and N. Peters, "On stocastic damköhler number variations in a homogeneous flow reactor," Principles and potential of HiCOT combustion. Proceedings of the Forum on High-Temperature Air Combustion Technology, vol. 4, pp. 495–509, 2000.

[62] N. Peters, "Principles and potential of hicot combustion," Combust. Theor. Model., vol. 4, p. 109, 2001.

[63] R. Bhaya, A. De, and R. Yadav, "Large eddy simulation of MILD combustion using pdf-based turbulencechemistry interaction models," Combust. Sci. Technol, vol. 186, pp. 1138–1165, 2014.

[64] F. Christo and B. Dally, "Modeling turbulent reacting jets issuing into a hot and diluted coflow," Combust. Flame, vol. 142, pp. 117–129, 2005.

[65] M. Ihme and Y. See, "LES flamelet modeling of a three-stream MILD combustor: Analysis of flame sensitivity to scalar inflow conditions," Proc. Combust. Inst., vol. 33, pp. 1309–1317, 2011.

[66] P. Coelho and N. Peters, "Numerical simulation of a MILD combustion burner," Combust. Flame, vol. 124, pp. 503–518, 2001.

[67] T. Plessing, N. Peters, and J. Wünning, "Laseroptical investigation of highly preheated combustion with strong exhaust gas recirculation," Proc. Combust. Inst, vol. 27, pp. 3197–3204, 1998.

[68] J. Kim, U. Schnell, and G. Scheffknecht, "Comparison of different global reaction mechanisms for mild combustion of natural gas," Combust. Sci. Technol., vol. 180, pp. 565–592, 2008.

[69] S. J. Brookes and J. Moss, "Measurements of soot production and thermal radiation from confined turbulent jet diffusion flames of methane," Combust. Flame, vol. 116, pp. 49–61, 1999.

[70] H. Kassem, K. Saqr, H. Aly, M. Sies, and M. Wahid, "Implementation of the eddy dissipation model of turbulent non-premixed combustion in openfoam," Int. Commun. Heat Mass Transfer, vol. 38, pp. 363–367, 2011.

[71] M. Roomina and R. Bilger, "Conditional Moment closure (CMC) Predictions of a turbulent methane-air jet flame," Combust. Flame, vol. 125, pp. 1176–1195, 2001.

[72] M. Fairweather and R. Woolley, "First-order conditional moment closure modeling of turbulent, nonpremixed methane flames," Combust. Flame, vol. 138, no. 1-2, pp. 3–19, 2004.

[73] S. Girimaji, "Assumed β-pdf model for turbulent mixing: validation and extension to multiple scalar mixing," Combust. Sci. Technol., vol. 78, p. 177, 1991.

[74] S. Stårner, R. Bilger, K. Lyons, J. Frank, and M. Long, "Conserved scalar measurements in turbulent diffusion flames by a Raman and Rayleigh ribbon imaging method," Combust. Flame, vol. 99, no. 2, pp. 347–354, 1994.

[75] A. Milford and C. Devaud, "Investigation of an inhomogeneous turbulent mixing model for conditional moment closure applied to autoignition," Combust. Flame, vol. 157, pp. 1467–1483, 2010.

[76] C. Markides, G. D. Paola, and E. Mastorakos, "Measurements and simulations of mixing and autoignition of an n-heptane plume in a turbulent flow of heated air," Exp. Therm. Fluid Sci., vol. 31, no. 5, pp. 393–401, 2007.

[77] P. Hansen, "Numerical tools for analysis and solution of fredholm integral equations of the first kind," Inverse Problems, vol. 8, pp. 849–872, 1992.

[78] A. Tikhonov and V. Arsenin, "Solution of incorrectly formulated problems and the regularization method," Soviet Mathematics Doklady, vol. 4, pp. 1035–1038, 1963.

[79] P. Hansen, "The truncated svd as a method for regularization," vol. 27, pp. 534–553, 1987.

[80] W. Press, S. Teukolsky, W. Vetterling, and B. Flannery, Numerical Recipes: The Art of Scientific Computing. Cambridge University Press, 2007.

[81] C. Bowman, R. Hanson, D. Davidson, W. Gardiner, Jr., V. Lissianski, G. Smith, D. Golden, M. Frenklach, and M. Goldenberg, "GRI-Mech 2.11," 1995.

[82] S. Pope and U. Maas, "Simplifying chemical kinetics: Trajectory low-dimensional manifolds in composition space," Cornell University Report No FDA 93-11, 1993.

[83] A. Hindmarsh, "Odepack, a systematized collection of ode solvers," Sci. Comput, vol. 1, pp. 55–64, 1983.

[84] R. Renka, "Tripack: A constrained two-dimensional delaunay triangulation," ACM Transactions on Mathematical software, vol. 22, pp. 1–8, 1996.

[85] G. Farin, Curves and Surfaces for CAGD:A Practical Guide. Morgan Kaufmann, 2001.

[86] OpenFOAM (The open source CFD toolbox). software available at http://www.openfoam.org.

[87] R. S. Barlow, A. N. Karpetis, J. H. Frank, and J.-Y. Chen, "Scalar profiles and no formation in laminar opposed-flow partially premixed methane/air flames," Combust. Flame, vol. 127, pp. 2102–2118, 2001.

[88] V. Yakhot and A.Orszag, "Renormalization group analysis of turbulence," J. Sci. Comput., vol. 1, pp. 3–51, 1986.

[89] B. Vanderstraeten, D. Tuerlinckx, J. Berghmans, S. Vliegen, V. Oost, and B. Smit, "Experimental study of the pressure and temperature dependence on the upper flammability limit of methane/ air mixtures," J. Hazard. Mater., vol. 56, pp. 237–246, 1997.

[90] C. Devaud and K. Bray, "Assessment of the applicability of conditional moment closure to a lifted turbulent flame: first order model," Combust. Flame, vol. 132, pp. 102–114, 2003.

[91] J. Hadamard, Lectures on Cauchy's Problem in Linear Differential Equations,. Yale University Press, New Haven, CT, 1923.

[92] K. Braman, T. Oliver, and V. Raman, "Bayesian analysis of syngas chemistry models," Combust. Theor. Model., pp. 1–30, 2013.

[93] R. Dibble, A. Masri, and R. Bilger, "The spontaneous raman scattering technique applied to nonpremixed flames of methane," Combust. Flame, vol. 67, pp. 189–206, 1987.

[94] P. Hansen, Rank-Deficient and Discrete Ill-Possed Problems. SIAM, 1998.

[95] A. Gelman, J. Carlin, H. Stern, and D. Rubin, Bayesian Data Analysis. Chapman & Hall/ CRC, 2004.

[96] A. Gelb, "Applied optimal estimation," MIT press, Cambridge MA, p. 79, 2001.

[97] R. M. Neal, "Slice sampling," Ann. Statist., vol. 31, no. 3, pp. 705–767, 2003.

[98] K. Daun, S. Waslander, and B. Tulloch, "Infrared species tomography of a transient flow field using kalman filtering," Appl. Optics, vol. 50, pp. 891–900, 2011.

[99] R. Charnigo, M. Francoeur, P. Kenkel, M. Mengüç, B. Hall, and C. Srinivasana, "Credible intervals for nanoparticle characteristics," J. Quant. Spectrosc. Ra., vol. 113, pp. 182–193, 2012.

[100] M. Chen and Q.Shao, "Monte carlo estimation of bayesian credible and hpd intervals," J. Comput. Graph. Stat., vol. 8, pp. 69–92, 1999.

[101] T. Coleman and Y. Li, "An interior, trust region approach for nonlinear minimization subject to bounds," SIAM Journal on Optimization, vol. 6, pp. 418–445, 1996.

[102] T. Coleman and Y. Li, "On the convergence of reflective newton methods for large-scale nonlinear minimization subject to bounds," Mathematical Programming, vol. 67, pp. 189–224, 1994.

[103] J. D. Jr., "Nonlinear least-squares," pp. 269–312.

[104] K. Levenberg, "A method for the solution of certain problems in least-squares," Quarterly Applied Math, pp. 164–168, 1944.

[105] S. Pope and U. Maas, "Simplifying chemical kinetics: Trajectory low-dimensional manifolds in composition space," Cornell University Report No FDA 93-11, 1993.

[106] M. Ihme and H. Pitsch, "Modeling of radiation and nitric oxide formation in turbulent nonpremixed flames using a flamelet/progress variable formulation," Phys. Fluids, vol. 20, no. 5, 2008.

[107] R. Weber, S. Orsino, N. Lallermant, and A. Verlaan, "Combustion of natural gas with high-temperature air and large quantities of flue gas," Proc. Combust. Inst, vol. 28, pp. 1315–1321, 2000.

[108] S. Orsino, R. Weber, and U. Bollettini, "Numerical simulation of combustion of natural gas with high-temperature air," Combust. Sci. Technol., vol. 170, pp. 1–34, 2001.

[109] M. Mancini, P. Schwöppe, R. Webber, and S. Orsino, "On mathematical modelling of flameless combustion," Combust. Flame, vol. 150, pp. 54–59, 2007.

[110] R. Bilger, S. Stårner, and R. Kee, "On reduced mechanisms for methane-air combustion in nonpremixed flames," Combust. Flame, vol. 80, pp. 135–149, 1990.

[111] M. Ihme, J. Zhang, G. He, and D. Dally, "Large-eddy simulation of a jet-in-hot-coflow burner operating in the oxygen-diluted combustion regime," Flow Turbul. Combust, vol. 89, pp. 449–464, 2012.

[112] A. Kronenburg, "Double conditioning of reactive scalar transport equations in turbulent nonpremixed flames," Phys. Fluids, vol. 16, pp. 2640–2648, 2004.

[113] G. Nivarti, M. Salehi, and W. Bushe, "A mesh partitioning algorithm for preserving spatial locality in arbitrary geometries," J. Comput. Phys., vol. 281, pp. 352–364, 2015.

[114] S. Navarro-Martinez and S. Rigopoulos, "Large eddy simulation of a turbulent lifted flame using conditional moment closure and rate-controlled constrained equilibrium," Flow Turbul. Combust., vol. 87, pp. 407–423, 2011.

[115] B. Launder and D. Spalding, "The numerical computation of turbulent flows," Comput. Methods Appl. Mech. Eng., vol. 3, no. 2, pp. 269–289, 1974.

[116] T. Shih, W. Liou, A. Shabbir, Z. Yang, and J. Zhu, "A new k- eddy viscosity model for high reynolds number turbulent flows," Comput. Fluids, vol. 24, no. 3, pp. 227–238, 1995.

[117] B. Fiorina, R. Vicquelin, P. Auzillon, N. Darabiha, O. Gicquel, and D. Veynante, "A filtered tabulated chemistry model for LES of premixed combustion," Combust. Flame, pp. 465–475, 2010.

[118] M. Salehi and W. Bushe, "Presumed PDF modeling for RANS simulation of turbulent premixed flames," Combust. Theory Model., pp. 381–403, 2010.

[119] C. Wall, B. J. Boersma, and P. Moin, "An evaluation of the assumed beta probability density function subgrid-scale model for large eddy simulation of nonpremixed, turbulent combustion with heat release," Phys. Fluids, vol. 12, pp. 2522–2529, 2000.

[120] H. Pitsch, "Large-Eddy Simulation of Turbulent Combustion," Ann. Rev. Fluid Mech., vol. 38, pp. 453–483, 2006.

[121] A. Triantafyllidis and E. Mastorakos, "Implementation issues of the Conditional Moment Closure model in large eddy simulations," Flow Turbul. Combust., vol. 84, pp. 481–512, 2009.

[122] M. Ihme and H. Pitsch, "Prediction of extinction and reignition in nonpreimixed turbulent flames using a flamelet/progress variable model 2. application in les of sandia flames D and E," Combust. Flame, vol. 155, pp. 90–107, 2008.

[123] H. Jasak, H. Weller, and A. Gosman, "High resolution nvd differencing scheme for arbitrarily unstructured meshes," Int. J. Numer. Meth. Fluids, vol. 31, pp. 431–449, 1999.

[124] D. A. Lysenko, I. Ertesvtåg, and K. Rian, "Large-eddy simulation of the flow over a circular cylinder at reynolds number 3900 using the openfoam toolbox," Flow Turbul. Combust., vol. 89, pp. 491–518, 2012.

[125] N. Kornev and E. Hassel, "Method of random spots for generation of synthetic inhomogeneous turbulent fields with prescribed autocorrelation functions," Commun. Numer. Meth. En., vol. 23, pp. 35–43, 2007.

[126] D. Veynante and R. Knikker, "Comparison between LES results and experimental data in reacting flows," Combust. Flame, vol. 7, no. 35, pp. 1–20, 2006.

[127] E. Knudsen, Shashank, and H. Pitsch, "Modeling partially premixed combustion behavior in multiphase LES," Combust. Flame, vol. 162, pp. 159–180, 2105.

[128] S. Pope, "Ten questions concerning the large-eddy simulation of turbulent flows," New J. Physics, vol. 6, pp. 35–59, 2004.

[129] Fire Dynamic Simulator (FDS). http://fire.nist.gov/fds.

[130] FireFOAM. http://github.com/fireFoam-dev.